UNIVERSITY OF CALIFORNIA, SAN DIEGO

Chemical Sensor Development in Oceanography

A dissertation submitted in partial satisfaction of the requirements for the degree
Doctor of Philosophy

in

Oceanography

by

Yuichiro Takeshita

Committee in charge:

Todd R. Martz, Chair
Andrew G. Dickson
Kenneth S. Johnson
Andrew Kummel
Dale Stokes
Lynne Talley

2014

The Dissertation of Yuichiro Takeshita is approved, and it is acceptable in quality and form for publication on microfilm and electronically:

Chair

University of California, San Diego

2014

EPIGRAPH

Preconceived notions are the locks on the door to wisdom.

- Merry Browne

TABLE OF CONTENTS

LIST OF FIGURES

LIST OF TABLES

ACKNOWLEDGMENTS

I would not have been able to complete this journey by myself, nor would I be the same person or scientist that I am today without the help and support of so many people throughout my time at Scripps. First and foremost, I would like to thank my advisor, Todd Martz. Todd, you helped me develop my scientific writing skills, offered me countless opportunities both in the lab and the field, and always encouraged me to pursue my "side projects". I could not have asked for a better mentor to guide me through this influential period of my professional career. I will always cherish our experience learning how to sail. I cannot be more thankful that I ended up in your lab. Members of the Martz lab have also been an integral part of my life at Scripps. Thank you Brittany Peterson, Phil Bresnahan, John Ballard, Ellen Briggs, Makaila LaShomb and Magali Poracchia.

I feel privileged for working down the hall from the Dickson lab for the majority of my time at Scripps. Andrew Dickson provided laboratory space and equipment that allowed me to carry out experiments presented in chapter 3. I would also like to thank Guy Emanuel and George Anderson for providing me with expert knowledge on carbonate and analytical chemistry. Emily Bockmon, thank you for always being there for me to talk science.

It has been a pleasure collaborating with Ken Johnson, and I am so grateful to have been involved in the development of the Deep Sea Durafet. He has been extremely supportive throughout my graduate career, and has been a continuing source

of inspiration to become a better scientist. I want to thank the members of the Johnson lab – Hans Jannash, Josh Plant, and Luke Coletti – for providing me with hardware for the high pressure chamber, Matlab code to process profiling float data, and a prototype Deep Sea Durafet to test at sea.

I feel very lucky to have been a student PI of the San Diego Coastal Expedition, under wonderful chief scientists Christina Frieder and Benjamin Grupe. I would especially like to thank Christina for generously delegating extra time to team CTD at all hours of the day, and for being the inspiration for the modelling work that resulted in chapter 5. The sample collection and analysis used for that study would not have been possible without all of the volunteers who generously offered their time for this research cruise.

To all of my friends that I have made during my time at Scripps: Thank you so much for making the past six years so incredibly enjoyable. You all are the most important part of this journey, and I am so deeply thankful that we were able to share our lives together. I will always treasure our memories – Emily Bockmon, Randie Bundy, Mattias Cape, Emily Donham, Geoff Cromwell, Amanda Frossard, Benjamin Grupe, Emily Kelly, Gabe Kooperman, Summer Martin, Mike Navarro, Sarah Smith, Taylor Stratton, and many more! Where should we do Big Bear next year?

Finally, I would like to thank my family for always believing in me. Mito, Nick, you have been incredibly supportive over the years. Thank you for hosting me for 2 weeks during the polar vortex while I started writing my dissertation.

This dissertation would not have been possible without the support of the National Science Foundation, Scripps Director's Fellowship, the University of California Multiple Campus Research Programs and Initiatives, UC ship funds, and the National Oceanographic Partnership Program,

Chapter 2, in full, is a reprint of previously published material in Journal of Geophysical Research: Oceans, 2013. Takeshita, Y., Martz, T.R., Johnson, K.S., Plant, J.N., Gilbert, D., Riser, S.C., Neill, C., and Tilbrook, B. The dissertation author was the primary investigator and author of this paper.

Chapter 3, in full, is currently being prepared for submission for publication of the material. Takeshita, Y., Martz, T.R., Johnson, K.S., and Dickson, A.G. The dissertation author was the primary investigator and author of this paper.

Chapter 4, in full is currently being prepared for submission for publication of the material. Takeshita, Y., Martz, T.R., Johnson, K.S. and Jannasch, H.W. The dissertation author was the primary investigator and author of this paper.

Chapter 5, in full, is currently being prepared for submission for publication of the material. Takeshita, Y., Frieder, C.A., Martz, T.R., Ballard, J.R., Feely, R.A., Nam, S., and Navarro, M. The dissertation author was the primary investigator and author of this paper.

VITA

2008 Bachelor of Arts, Carleton College

2012 Teaching Assistant, "Aqueous Chemistry", University of California, San Diego

2014 Doctor of Philosophy, University of California, San Diego

PUBLICATIONS

Takeshita, Y., Martz, T.R., Johnson, K.S., Plant, J.N., Gilbert, D., Riser, S.C., Neill, C., and Tilbrook, B. 2013 A Climatology-Based Quality Control Procedure for Profiling Float Oxygen Data. *Journal of Geophysical Research-Oceans*, 118, 5640-5650. doi: 10.1002/jgrc.20399

Bresnahan, P.J., Martz, T.R., **Takeshita, Y.**, Johnson, K.S., and LaShomb, M. 2014 Best practices for autonomous measurement of seawater pH with the Honeywell Duraeft. *Methods in Oceanography*. *Accepted*.

Cich, M.J., Hill, I.M., Lackner, A.D., Martinez, R.J., Ruthenburg, T.C., **Takeshita, Y.**, Young, A.J., Drew, .M., Buss, C.E., and Mann, K.R. 2010 Enantiomerically Selective Vapochromic Sensing. *Sensors and Actuators B: Chemical*, 149, 199-204

Hoffman, G.E., Smith, J.E., Johnson, K.S., Send, U., Levin, L.A., Micheli, F., Paytan, A., Price, N.N., Peterson, B., **Takeshita, Y.**, Matson, P.G., Crook E.D., Kroeker, K.J., Gambi, M.C., Rivest E.B., Frieder, C.A., Yu, P.C., and Martz, T.R. 2011 High-frequency dynamics of ocean pH: a multi-ecosystem comparison. *PloS ONE*, 6(12) e28983. doi:10.1371/journal.pone.0028983

Martz, T.R., **Takeshita, Y.**, Rolph, R., and Bresnahan, P.J. 2012 Tracer Monitored Titrations: Measurement of Dissolved Oxygen. *Analytical Chemistry*, 84(1), 290-296. doi**:** 10.1021/ac202537f

Martz, T.R. Send, U., Ohman, M.D., **Takeshita, Y.**, Bresnahan, P., Kim, H., and Nam, S. 2014. Dynamic Variability of Biogeochemical Ratios in the Southern

California Current System. *Geophysical Research Letters*, 41(7), 2496-2501. doi: 10.1002/2014GL059332

Paytan, A., Crook, E.D., Cohen, A. L, Martz, T.R., **Takeshita, Y**., Rebolledo-Vieyra, M., and Hernandez, L. 2014 Reply to Iglesias-Prieto et al.: Combined field and laboratory approaches for the study of coral calcification. *Proceedings of the National Academy of Sciences of the United States of America*, 111(3), E302-E303. doi: 10.1073/pnas.1319572111

Petrenko, V.V., Severinghaus, J.P., Smith, A.M., Riedel, K., Baggenstos, D., Harth, C., Orsi, A., Hua, Q., Franz, P., **Takeshita, Y.**, Brailsford, W., Weiss, R.F., Buizert, C., Dickson, A., Schaefer, H. 2013. High-precision ^{14}C measurements demonstrate production of in situ cosmogenic (CH_4)-^{14}C and rapid loss of in situ cosmogenic (CO)-^{14}C in shallow Greenland firn. *Earth and Planetary Science Letters*, 365, 190-197. doi: 10.1016/j.epsl.2013.01.032

ABSTRACT OF THE DISSERTATION

Chemical Sensor Development in Oceanography

by

Yuichiro Takeshita

Doctor of Philosophy in Oceanography

University of California, San Diego 2014

Professor Todd R. Martz, Chair

In situ autonomous chemical sensors, combined with the right deployment platforms provide novel, powerful tools for oceanographers to observe biogeochemical processes on unprecedented spatial and temporal scales. However, many aspects of chemical sensor technology have not yet reached full maturity, preventing routine use by the community at large. This dissertation aims to fill this critical need in ocean observing technology, with a focus on Ion Sensitive Field Effect Transistor (ISFET) pH sensors for profiling float applications. Following a brief introduction to the current status of marine chemical sensor technology, the four chapters address the various steps involved in sensor development: sensor

characterization, calibration, data quality control (QC), and a modeling effort using sensor data.

Chapter 2 introduces a simple QC protocol for profiling float oxygen data by comparison to a monthly climatology. This protocol can constrain O_2 at the surface to better than 3%, and detect sensor drift with high confidence. Similar approaches can be taken to QC other chemical sensors data from profiling floats.

Chapter 3 characterizes the response of the ISFET pH sensor and the Chloride-Ion Selective Electrode by comparison to the hydrogen electrode and the silver-silver chloride electrode, respectively. Both electrodes showed near-Nernstian response, thus the error in pH due to non-theoretical behavior of the electrodes is negligible over the oceanic range of pH and salinity.

Chapter 4 quantifies the effect of pressure on the pH of certified tris buffer prepared in synthetic seawater. Assignment of pH values to certified buffer solutions is essential for sensor calibration. As the number of pH sensors deployed under high pressures is expected to increase, this chapter will fill a critical need in sensor validation and traceability.

Chapter 5 presents habitat-specific ocean acidification projections between 2012 and 2100 for 4 habitats in the upper 100 m of the Southern California Bight. The projections were generated by combining high frequency pH sensor data, a regional empirical relationship of the CO_2 system, and hydrographic data to characterize the properties of upwelled waters. Habitat specific acidification signals were predicted, and implications for future ocean acidification research are discussed.

CHAPTER 1: INTRODUCTION

In situ chemical sensors are changing the landscape of monitoring chemical distribution and variability in the marine ecosystem [*Johnson et al.*, 2007; *Prien*, 2007; *Moore et al.*, 2009]. Combined with the right deployment platforms, they are capable of providing chemical data with temporal and spatial resolution never before attainable. Profiling floats are one of the best monitoring platforms available for studying the seasonal evolution of biogeochemical cycles on regional to global scales. Given their potential, significant progress has been made to equip profiling floats with a limited number of chemical and bio-optical sensors [*Johnson et al.*, 2009], and the resulting data have been used to study pelagic production [*Riser and Johnson*, 2008], nutrient supply in subtropical gyres [*Johnson et al.*, 2010], carbon export [*Bishop et al.*, 2002, 2004], air-sea gas flux [*Kihm and Körtzinger*, 2010], and oxygen minimum zone dynamics [*Prakash et al.*, 2012]. However, many aspects of this technology have not yet reached full maturity. For example, one major limitation is the lack of an established calibration protocol for chemical sensors on profiling floats. This is partly due to the fact that in some cases, there is no consensus among the community as to which sensor should be integrated onto floats, or the chemical sensing technology is still evolving, making it difficult, or impossible to establish calibration protocols. Nevertheless, the lack of such protocols prohibits the wide-use of chemical sensor data from profiling floats, and limits the use of data to the individual research groups deploying the sensors. Improvements in chemical sensor technology, calibration, and

data quality control protocols would greatly benefit the oceanographic community by providing new, powerful tools to monitor the ocean.

Over the course of my dissertation, I have had the great privilege of being involved in the development of the Deep Sea Durafet, a pH sensor designed to be equipped on profiling floats. This collaborative effort led by Ken Johnson between the Monterey Bay Aquarium Research Institute, Honeywell, University of Washington, and the Scripps Institution of Oceanography led to the successful deployment of the first pH profiling float at the Hawaii Oceanic Time-series (HOT) station ALOHA. My involvement in this project has guided my dissertation, and three of the four chapters are designed to complement the development of the Deep Sea Durafet.

Role of Chemical Sensors for Ocean Monitoring

In order to study oceanic biogeochemical processes, observations should be made at the same, or higher temporal and spatial resolution than the phenomenon of interest [*Prien,* 2007]. Almost all chemical measurements in the ocean are made by capturing discrete samples in the field, and analyzing them in laboratories. This is largely because chemical oceanographers are faced with the painstaking task of measuring chemicals that occur in very low concentrations (nM - µM) in a solution containing other ions with similar chemical properties but in much greater abundance [*Johnson et al.,* 1992]. As a result, analysis often requires sophisticated instruments with high sensitivity and specificity that need to be operated by skilled technicians, making analysis time consuming, labor intensive, and expensive. Furthermore, large areas of the ocean require long transit time from shore (weeks), and often require

working under harsh environments. These challenges result in no observations, to perhaps 1-2 samples per decade (e.g. repeat hydrography cruises) over the majority of the ocean. Many important biogeochemical processes that occur on much shorter time scales (e.g., annual, seasonal, tidal, and diurnal) go completely unobserved. Even well-monitored areas such as the coastal ocean or oceanographic time-series stations (e.g. HOT and Bermuda Atlantic Time-Series Study) are monitored only monthly at best. Although the value of these datasets is considerable, it is becoming widely recognized that traditional discrete sampling methods are insufficient for understanding many of the underlying processes responsible for the chemical variability in marine ecosystems [*Daly,* 2000]. This problem, often referred to as the "undersampling problem", has always been one of the largest challenges for the oceanographic community, and will require new technologies to overcome.

In situ chemical sensors can vastly improve the temporal resolution of chemical measurements in the ocean by providing high-frequency measurements (minutes to hours) for months, to potentially years. Furthermore, the spatial resolution can be improved when combined with effective monitoring platforms, such as gliders [*Davis et al.*, 2008; *Nicholson et al.*, 2008], profiling floats [*Johnson et al.*, 2007, 2009], and biological platforms [*Boehme et al.*, 2008]. However, chemical sensor technology is not as mature as other sensors that are commonly deployed on oceanographic platforms such as those for temperature, salinity, and pressure [*Byrne and Diamond,* 2006; *Moore et al.,* 2009]. Rapid strides in chemical sensing technology have been made in the past decade [*Daly et al.*, 2004], and use of chemical

sensors for quantitative biogeochemical analysis is becoming more common [*Emerson et al.*, 2008, 2011; *Harris et al.*, 2013; *Martz et al.*, 2014]. Further development of robust chemical sensor technologies will dramatically increase the temporal and spatial resolution of chemical observations in the ocean.

Profiling Floats

Profiling floats are Lagrangian platforms designed to observe oceanic processes on a basin to global scale [*Davis*, 1991a, 1991b]. The first floats were deployed during the World Ocean Circulation Experiment to study deep ocean circulation patterns [*Davis et al.*, 1992]. The success from the small array deployed in the 1990's triggered an international effort to create a global array of profiling floats to monitor the physical processes in the upper 2000 m of the world's oceans in real time. This was the birth of the program now famously known as ARGO. The program reached full maturity in 2007 when the float array reached the target size of ~3000 floats, or 1 float every 3 × 3 latitude/longitude grid. The ARGO program has maintained, or slightly increased their float array size since, and has proven to be one of the most successful oceanographic observing systems.

Each float contains a hydraulic pump that compresses and inflates an external bladder to control the density of the float in situ for autonomous profiling through the upper 2000 meters of the water column. Once every 5-10 days, the profiling float ascends from its park depth (1000-2000 meters) while measuring temperature, salinity, and pressure. At the surface, the float transmits its data to a satellite, and then descends to its park depth. The float repeats this cycle for usually 4-5 years, providing

several hundred profiles throughout its lifetime. Currently, there are approximately 3500 floats operating in the ocean, providing publicly available data in near real-time from around the globe (www.argo.ucsd.edu).

Floats offer several distinct advantages as observing platforms. First, the spatial and temporal coverage of the data is unprecedented. They are not limited to ship tracks and repeat hydrography transects, or by hostile conditions in austral winters in the southern ocean, for example. This largely eliminates potential spatial and temporal biasing issues during analysis. Furthermore, advancements in ice-avoiding algorithms now allow floats to operate reliably under areas with seasonal ice-cover [*Wong and Riser*, 2013], allowing observations in locations that were previously inaccessible. Second, sensors on profiling floats seem to be minimally impacted by biofouling, especially when compared to near-surface monitoring platforms. This is because floats spend the majority of their time in the deep, dark ocean, and only surface periodically to the euphotic zone, where biofouling is most intense This allows for long term observations without the expenses and complications involved in combating biofouling. Finally, the economic benefits of using profiling floats are significant. For example, a typical repeat hydrography cruise obtains approximately four profiles a day, and costs anywhere between $20,000 and $40,000 to operate daily. This simple calculation estimates the cost of each profile at $5,000-$10,000. On the other hand, a profiling float costs approximately $20,000 and provides over a hundred profiles during its lifetime, costing under $200 per profile.

Chemical Sensors on Profiling Floats

Development of chemical sensors for profiling floats faces unique obstacles such as strict requirements for size, weight, power, reagent consumption, fast response time, and long-term stability. Despite these challenges, a number of prototype sensors have been successfully equipped onto profiling floats, including those for particulate organic carbon [*Bishop et al.*, 2002, 2004; *Bishop and Wood*, 2009], total gas pressure [*McNeil et al.*, 2006], pCO_2 [*Fiedler et al.*, 2013], and colored dissolved organic matter [*Xing et al.*, 2014]. Furthermore, improvements in profiling float technology has made much of this integration possible: efficient piston motors for reduced power consumption; introduction of the Iridium satellite communication system that enables significantly accelerated data transfer rates and increased data load; and increased payload capacities. However, very few or perhaps, no sensors currently exist for measuring inorganic carbon parameters in seawater that meet the requirements listed above. This represents a critical gap in sensor technology given the immense importance of the oceanic carbon cycle.

An equally important, yet often overlooked aspect of sensor development is the establishment of rigorous calibration protocols. Proper calibration and characterization of sensors is essential in meeting the stringent requirements of data quality desired by the oceanographic community. Deploying sensors that has undergone a tenuous calibration process makes interpretation of data difficult, and in the worst case, may lead to irrecoverable data. For example, several hundred profiling floats equipped with oxygen sensors were deployed worldwide using factory calibration coefficients, and as a result, much of the data could not be used for quantitative biogeochemical analyses.

I applied a post-deployment correction to the global oxygen profiling float dataset in chapter 2. Although significant improvements were made to the dataset, there were limitations to this approach such as basin-dependent differences in the quality of the corrections. The obvious alternative is to calibrate chemical sensors prior to deployment to the highest quality, thus ensuring a dataset that does not require large post-deployment corrections, if at all. One of the major goals for the development of the Deep Sea Durafet was to establish a comprehensive calibration protocol to avoid pitfalls that oxygen sensors on profiling floats encountered. Two chapters in my dissertation describe in detail the characterization and calibration of the Deep Sea Durafet.

Ocean Acidification

The ocean has absorbed roughly 40% of the anthropogenic CO_2 since the industrial revolution [*Sabine and Tanhua*, 2010], and as a result the surface ocean pH has declined by roughly 0.1 since pre-industrial times [*Caldeira and Wickett*, 2003]. This phenomenon, known as anthropogenic ocean acidification, is expected to have detrimental effects on marine organisms [*Doney et al.*, 2009], especially to those with calcium carbonate shells and skeletons [*Langdon et al.*, 2000; *Barton et al.*, 2012]. Although studies on the effects of elevated CO_2 on organisms based in the laboratory and the field are abundant, [e.g. *Yates and Halley*, 2006; *Hall-Spencer et al.*, 2008; *Kroeker et al.*, 2011; *Frieder et al.*, 2014; *White et al.*, 2014] direct observations of the acidification trend is relatively scarce [e.g. *Dore et al.*, 2009; *Leinweber and Gruber*, 2013; *Bates et al.*, 2014]. One of the major challenges of detecting the acidification

signal is the expense and expertise that is required to sustain monthly to seasonal measurements for multiple years to decades. An observation system of this magnitude is required because pH of seawater experiences large natural fluctuations on diel [*Hofmann et al.*, 2011; *Price et al.*, 2012], seasonal [*McNeil and Matear*, 2008], and decadal [*Nam et al.*, 2011] time scales. As the rate of decrease of pH is expected to have significant regional variability [*Cai et al.*, 2011; *Gruber et al.*, 2012], direct observations of ocean acidification and the development of robust region to habitat specific acidification models is a critical necessity to accurately assess the impacts of ocean acidification on marine ecosystems.

Dissertation Outline

Each chapter in this dissertation addresses a different aspect of chemical sensor development: (in order of chapters) post deployment data quality control, sensor characterization, sensor calibration, and a modeling effort using sensor data.

In Chapter 2, I describe a simple QC procedure for profiling float oxygen data using a monthly climatology. This study takes the first step of establishing a QC protocol for profiling float oxygen data; a critical component of a global biogeochemical sensor array. Similar approaches can be taken for other chemical parameters in the future.

Chapter 3 presents thorough characterization of the Nernstian response of ISFET and Cl-ISE to the activity of proton and chloride ion, respectively. Results from 3 ISFETs and 7 Cl-ISE reveal near-Nernstian behavior for both electrodes over a large range of hydrogen and chloride ion activity, respectively. The uncertainty due to non-

Nernstian behavior of the electrodes over the oceanic range of pH and salinity is negligible.

In Chapter 4, the partial molal volume of Tris buffer in artificial seawater ($\Delta V_{\mathrm{Tris}}^{\mathrm{SW}}$) is reported. Tris buffer has become accepted as the primary pH standard by the chemical oceanography community, and has been used to calibrate both potentiometric and spepctrophotometric pH measurements in seawater. However the buffer solution has only been characterized at 1atm, and the effects of pressure are relatively unknown. $\Delta V_{\mathrm{Tris}}^{\mathrm{SW}}$ must be quantified for the development of improved calibration protocols for pH sensors intended for high pressure applications, along with the capability of validating pH sensor data in situ.

In Chapter 5, habitat-specific ocean acidification projections between 2012 and 2100 are generated for 4 habitats in the upper 100 m of the Southern California Bight. These projections were generated by combining high frequency pH sensor data, a regional empirical relationship of the CO_2 system, and hydrographic survey data that characterized the source water properties of upwelled waters. Implications for future ocean acidification research are discussed.

References

Barton, A., B. Hales, G. G. Waldbusser, C. Langdon, and R. a. Feely (2012), The Pacific oyster, Crassostrea gigas, shows negative correlation to naturally elevated carbon dioxide levels: Implications for near-term ocean acidification effects, *Limnol. Oceanogr.*, *57*(3), 698–710, doi:10.4319/lo.2012.57.3.0698.

Bates, N. R., Y. M. Astor, M. J. Church, K. Currie, J. E. Dore, M. Gonzalez-Davila, L. Lorenzoni, F. Muller-karger, J. Olafsson, and J. M. Santana-Casiano (2014), A Time-Series View of Changing Surface Ocean Chemistry Due to Ocean Uptake of Anthropogenic CO2 and Ocean Acidification, *Oceanography*, *1*, 126–141.

Bishop, J. K. B., and T. J. Wood (2009), Year-round observations of carbon biomass and flux variability in the Southern Ocean, *Global Biogeochem. Cycles*, *23*, 1–12, doi:10.1029/2008GB003206.

Bishop, J. K. B., R. E. Davis, and J. T. Sherman (2002), Robotic observations of dust storm enhancement of carbon biomass in the North Pacific, *Science (80-.).*, *298*(5594), 817–821, doi:10.1126/science.1074961.

Bishop, J. K. B., T. J. Wood, R. E. Davis, and J. T. Sherman (2004), Robotic observations of enhanced carbon biomass and export at 55 degrees S during SOFeX, *Science (80-.).*, *304*(5669), 417–420, doi:10.1126/science.1087717.

Boehme, L., S. E. Thorpe, M. Biuw, M. Fedak, and M. P. Meredith (2008), Monitoring Drake Passage with elephant seals : Frontal structures and snapshots of transport, *Limnol. Oceanogr.*, *53*(5), 2350–2360.

Byrne, R., and D. Diamond (2006), Chemo/bio-Sensor Networks, *Nat. Mater.*, *5*(6), 421–424.

Cai, W.-J. et al. (2011), Acidification of subsurface coastal waters enhanced by eutrophication, *Nat. Geosci.*, *4*(11), 766–770, doi:10.1038/ngeo1297.

Caldeira, K., and M. E. Wickett (2003), Anthropogenic carbon and ocean pH, *Nature*, *425*(6956), 365.

Daly, K. L. (2000), Meeting Explores Sensor Technology for Remote, Interactive Aquatic Experiments, *EOS, Trans Am. Geophys. Union*, *81*(580), 1–3.

Daly, K. L., R. H. Byrne, A. G. Dickson, S. M. Gallager, M. J. Perry, and M. K. Tivey (2004), Chemical and Biological Sensors for Time-Series Research: Current

Status and New Directions, *Mar. Technol. Soc. J.*, *38*(2), 121–143, doi:10.4031/002533204787522767.

Davis, R. E. (1991a), Lagrangian Ocean Studies, *Annu. Rev. Fluid Mech.*, *23*, 43–64.

Davis, R. E. (1991b), Observing the general circulation with floats, *Deep Sea Res. Part A. Oceanogr. Res. Pap.*, *38*, S531–S571, doi:10.1016/S0198-0149(12)80023-9.

Davis, R. E., D. C. Webb, L. A. Regier, and D. J. (1992), The Autonomous Lagrangian Circulation Explorer (ALACE), *J. Atmos. Ocean. Technol.*, *9*, 264–285.

Davis, R. E., M. D. Ohman, D. L. Rudnick, J. T. Sherman, and B. Hodges (2008), Glider surveillance of physics and biology in the southern California Current System, *Methods*, *53*, 2151–2168.

Doney, S. C., V. J. Fabry, R. a. Feely, and J. a. Kleypas (2009), Ocean Acidification: The Other CO 2 Problem, *Ann. Rev. Mar. Sci.*, *1*(1), 169–192, doi:10.1146/annurev.marine.010908.163834.

Dore, J. E., R. Lukas, D. W. Sadler, M. J. Church, and D. M. Karl (2009), Physical and biogeochemical modulation of ocean acidification in the central North Pacific., *Proc. Natl. Acad. Sci. U. S. A.*, *106*(30), 12235–40, doi:10.1073/pnas.0906044106.

Emerson, S., C. Sabine, M. F. Cronin, R. Feely, S. E. Cullison Gray, and M. DeGrandpre (2011), Quantifying the flux of CaCO 3 and organic carbon from the surface ocean using in situ measurements of O 2 , N 2 , pCO 2 , and pH, *Global Biogeochem. Cycles*, *25*(3), 1–12, doi:10.1029/2010GB003924.

Emerson, S. R., C. Stump, and D. Nicholson (2008), Net biological oxygen production in the ocean: Remote in situ measurements of O 2 and N 2 in surface waters, *Global Biogeochem. Cycles*, *22*(3), 1–13, doi:10.1029/2007GB003095.

Fiedler, B., P. Fietzek, N. Vieira, P. Silva, H. C. Bittig, and A. Körtzinger (2013), In Situ CO 2 and O 2 Measurements on a Profiling Float, *J. Atmos. Ocean. Technol.*, *30*(1), 112–126, doi:10.1175/JTECH-D-12-00043.1.

Frieder, C. a, J. P. Gonzalez, E. E. Bockmon, M. O. Navarro, and L. a Levin (2014), Can variable pH and low oxygen moderate ocean acidification outcomes for mussel larvae?, *Glob. Chang. Biol.*, *20*(3), 754–64, doi:10.1111/gcb.12485.

Gruber, N., C. Hauri, Z. Lachkar, D. Loher, T. L. Frölicher, and G.-K. Plattner (2012), Rapid progression of ocean acidification in the California Current System., *Science (80-.).*, *337*(6091), 220–3, doi:10.1126/science.1216773.

Hall-Spencer, J. M., R. Rodolfo-Metalpa, S. Martin, E. Ransome, M. Fine, S. M. Turner, S. J. Rowley, D. Tedesco, and M.-C. Buia (2008), Volcanic carbon dioxide vents show ecosystem effects of ocean acidification., *Nature*, *454*(7200), 96–9.

Harris, K. E., M. D. DeGrandpre, and B. Hales (2013), Aragonite saturation state dynamics in a coastal upwelling zone, *Geophys. Res. Lett.*, *40*(11), 2720–2725, doi:10.1002/grl.50460.

Hofmann, G. E. et al. (2011), High-Frequency Dynamics of Ocean pH: A Multi-Ecosystem Comparison, edited by W.-C. Chin, *PLoS One*, *6*(12), e28983, doi:10.1371/journal.pone.0028983.

Johnson, K. S., K. H. Coale, and H. W. Jannasch (1992), Analytical Chemistry in Oceanography, *Anal. Chem.*, *64*(22), 1065–1075.

Johnson, K. S., J. A. Needoba, S. C. Riser, and W. J. Showers (2007), Chemical sensor networks for the aquatic environment., *Chem. Rev.*, *107*(2), 623–40, doi:10.1021/cr050354e.

Johnson, K. S., W. M. Berelson, E. S. Boss, Z. Chase, H. Claustre, S. R. Emerson, N. Gruber, A. Körtzinger, M. J. Perry, and S. C. Riser (2009), Observing Biogeochemical Cycles at Global Scales with Profiling Floats and Gliders Prospects for a Global Array, *Oceanography*, *22*(3), 216–225, doi:10.5670/oceanog.2009.81.

Johnson, K. S., S. C. Riser, and D. M. Karl (2010), Nitrate supply from deep to near-surface waters of the North Pacific subtropical gyre, *Nature*, *465*(7301), 1062–1065, doi:10.1038/nature09170.

Kihm, C., and a. Körtzinger (2010), Air-sea gas transfer velocity for oxygen derived from float data, *J. Geophys. Res.*, *115*(C12), 1–8, doi:10.1029/2009JC006077.

Kroeker, K. J., F. Micheli, M. C. Gambi, and T. R. Martz (2011), Divergent ecosystem responses within a benthic marine community to ocean acidification., *Proc. Natl. Acad. Sci. U. S. A.*, *108*(35), 14515–20, doi:10.1073/pnas.1107789108.

Langdon, C., T. Takahashi, C. Sweeney, D. Chipman, J. Goddard, F. Marubini, H. Aceves, H. Barnett, and M. J. Atkinson (2000), Effect of calcium carbonate

saturation state on the calcification rate of an experimental coral reef, *Global Biogeochem. Cycles*, *14*(2), 639–654.

Leinweber, A., and N. Gruber (2013), Variability and trends of ocean acidification in the Southern California Current System: A time series from Santa Monica Bay, *J. Geophys. Res. Ocean.*, *118*(7), 3622–3633, doi:10.1002/jgrc.20259.

Martz, T., U. Send, M. D. Ohman, Y. Takeshita, P. Bresnahan, H.-J. Kim, and S. Nam (2014), Dynamic Variability of Biogeochemical Ratios in the Southern California Current System, *Geophys. Res. Lett.*, *41*(7), 2496–2501, doi:10.1002/2014GL059332.

McNeil, B. I., and R. J. Matear (2008), Southern Ocean acidification: a tipping point at 450-ppm atmospheric CO2., *Proc. Natl. Acad. Sci. U. S. A.*, *105*(48), 18860–4, doi:10.1073/pnas.0806318105.

McNeil, C., E. D'Asaro, B. Johnson, and M. Horn (2006), A Gas Tension Device with Response Times of Minutes, *J. Atmos. Ocean. Technol.*, *23*(11), 1539–1558.

Moore, T. S., K. M. Mullaugh, R. R. Holyoke, A. S. Madison, M. Yücel, and G. W. I. Luther (2009), Marine Chemical Technology and Sensors for Marine Waters: Potentials and Limits, *Ann. Rev. Mar. Sci.*, *1*(1), 91–115, doi:10.1146/annurev.marine.010908.163817.

Nam, S., H.-J. Kim, and U. Send (2011), Amplification of hypoxic and acidic events by La Niña conditions on the continental shelf off California, *Geophys. Res. Lett.*, *38*(22), 1–5, doi:10.1029/2011GL049549.

Nicholson, D., S. R. Emerson, and C. C. Eriksen (2008), Net community production in the deep euphotic zone of the subtropical North Pacific gyre from glider surveys, *Limnol. Oceanogr.*, *53*(5), 2226–2236.

Prakash, S., T. M. B. Nair, T. V. S. U. Bhaskar, P. Prakash, and D. Gilbert (2012), Oxycline variability in the central Arabian Sea: An Argo-oxygen study, *J. Sea Res.*, *71*, 1–8, doi:10.1016/j.seares.2012.03.003.

Price, N. N., T. R. Martz, R. E. Brainard, and J. E. Smith (2012), Diel Variability in Seawater pH Relates to Calcification and Benthic Community Structure on Coral Reefs., *PLoS One*, *7*(8), e43843, doi:10.1371/journal.pone.0043843.

Prien, R. D. (2007), The future of chemical in situ sensors, *Mar. Chem.*, *107*(3), 422–432, doi:10.1016/j.marchem.2007.01.014.

Riser, S. C., and K. S. Johnson (2008), Net production of oxygen in the subtropical ocean, *Nature*, *451*(7176), 323–5, doi:10.1038/nature06441.

Sabine, C. L., and T. Tanhua (2010), Estimation of Anthropogenic CO 2 Inventories in the Ocean, *Ann. Rev. Mar. Sci.*, *2*(1), 175–198, doi:10.1146/annurev-marine-120308-080947.

White, M., L. Mullineaux, D. McCorkle, and A. Cohen (2014), Elevated pCO2 exposure during fertilization of the bay scallop Argopecten irradians reduces larval survival but not subsequent shell size, *Mar. Ecol. Prog. Ser.*, *498*, 173–186, doi:10.3354/meps10621.

Wong, A. P. S., and S. C. Riser (2013), Modified shelf water on the continental slope north of Mac Robertson Land, East Antarctica, *Geophys. Res. Lett.*, *40*(23), 6186–6190, doi:10.1002/2013GL058125.

Xing, X., H. Claustre, H. Wang, A. Poteau, and F. D'Ortenzio (2014), Seasonal dynamics in colored dissolved organic matter in the Mediterranean Sea: Patterns and drivers, *Deep Sea Res. Part I Oceanogr. Res. Pap.*, *83*, 93–101, doi:10.1016/j.dsr.2013.09.008.

Yates, K. K., and R. B. Halley (2006), CO3-- concentration and pCO2 thresholds for calcification and dissolution on the Molokai reef flat , Hawaii, *Biogeosciences*, *3*, 357–369.

CHAPTER 2: A CLIMATOLOGY-BASED QUALITY CONTROL PROCEDURE FOR PROFILING FLOAT OXYGEN DATA

JOURNAL OF GEOPHYSICAL RESEARCH: OCEANS, VOL. 118, 5640–5650, doi:10.1002/jgrc.20399, 2013

A climatology-based quality control procedure for profiling float oxygen data

Yuichiro Takeshita,[1] Todd R. Martz,[1] Kenneth S. Johnson,[2] Josh N. Plant,[2] Denis Gilbert,[3] Stephen C. Riser,[4] Craig Neill,[5] and Bronte Tilbrook[5]

Received 31 March 2013; revised 31 July 2013; accepted 12 September 2013; published 22 October 2013.

[1] Over 450 Argo profiling floats equipped with oxygen sensors have been deployed, but no quality control (QC) protocols have been adopted by the oceanographic community for use by Argo data centers. As a consequence, the growing float oxygen data set as a whole is not readily utilized for many types of biogeochemical studies. Here we present a simple procedure that can be used to correct first-order errors (offset and drift) in profiling float oxygen data by comparing float data to a monthly climatology (World Ocean Atlas 2009). Float specific correction terms for the entire array were calculated. This QC procedure was evaluated by (1) comparing the climatology-derived correction coefficients to those derived from discrete samples for 14 floats and (2) comparing correction coefficients for seven floats that had been calibrated twice prior to deployment (once in the factory and once in-house), with the second calibration ostensibly more accurate than the first. The corrections presented here constrain most float oxygen measurements to better than 3% at the surface.

Citation: Takeshita, Y., T. R. Martz, K. S. Johnson, J. N. Plant, D. Gilbert, S. C. Riser, C. Neill, and B. Tilbrook (2013), A climatology-based quality control procedure for profiling float oxygen data, *J. Geophys. Res. Oceans*, *118*, 5640–5650, doi:10.1002/jgrc.20399.

1. Introduction

[2] Profiling floats provide a near-ideal platform for monitoring the seasonal evolution of both physical and chemical processes at the regional, basin, and global scale. The number of oxygen measurements from profiling floats is rapidly growing, with over 450 "Argo Equivalents" deployed with oxygen sensors (of which >150 are currently operating). Data from these autonomous platforms has yielded new insights into oceanic biogeochemical processes [*Martz et al.*, 2008; *Riser and Johnson*, 2008; *Whitmire et al.*, 2009; *Johnson et al.*, 2010; *Kihm and Körtzinger*, 2010; *Juranek et al.*, 2011; *Prakash et al.*, 2012]. However, the profiling float oxygen data set is underutilized because, unlike temperature (T), salinity (S), and pressure (P) data, dissolved oxygen (O_2) data are not QC'd by the Argo data centers. For example, T, S, and P data are subject to detailed scrutiny by regional experts after an initial automated QC protocol. Salinity data go through further QC by comparison to a climatology derived from ship-based bottle and CTD data [*Wong et al.*, 2003; *Bohme and Send*, 2005; *Owens and Wong*, 2009]. With the number of oxygen measurements from the float array growing rapidly, it is important to develop and evaluate new QC procedures for O_2 in order to promote wide use of the profiling float oxygen data set.

[3] Currently, only a handful of oxygen profiling floats have been validated using discrete samples taken at or near the time of deployment, and the vast majority of the profiling float oxygen data are unverified. Although studies have shown that oxygen sensors on profiling floats can produce highly stable data over months to years [*Körtzinger et al.*, 2005; *Tengberg et al.*, 2006; *Riser and Johnson*, 2008], examples where large discrepancies (up to 40 μM) between profiling floats and discrete water samples taken nearby the float have been reported [*Kobayashi et al.*, 2006]. Clearly, a need to QC the oxygen data from profiling floats exists.

[4] Here we present a simple QC procedure for profiling float oxygen data based on comparing float data to a monthly climatology and therefore driving corrected float data toward the climatology. The Argo float oxygen data set from the U.S. Global Ocean Data Assimilation Experiment (USGODAE) server was compared to the World Ocean Atlas 2009 (WOA09) in order to derive sensor errors (offset and drift) relative to the climatology. This procedure was repeated and float data were compared to discrete samples

Additional supporting information may be found in the online version of this article.

[1]Scripps Institution of Oceanography, University of California San Diego, La Jolla, California, USA.
[2]Monterey Bay Aquarium Research Institute, Moss Landing, California, USA.
[3]Maurice-Lamontagne Institute Mont-Joli, Quebec, Canada.
[4]School of Oceanography, University of Washington, Seattle, Washington, USA.
[5]CSIRO Marine and Atmospheric Research, Hobart, Tas, Australia.

Corresponding author: T. R. Martz, Scripps Institution of Oceanography, University of California San Diego, La Jolla, CA 92039, USA. (trmartz@ucsd.edu)

2169-9275/13/10.1002/jgrc.20399

for a limited number of instances, where those data were available concurrently. We report float specific correction coefficients for the entire array and contrast the two methods.

2. Methods

2.1. World Ocean Atlas 2009

[5] WOA09 is a monthly climatology on a 1° latitude-longitude grid from the surface to 5500 m at 33 standard depths for T, S, $[O_2]$ (μM), and oxygen percent saturation (%Sat = $[O_2]/[O_{2Sat}] \times 100$, where $[O_{2Sat}]$ is the oxygen concentration at solubility equilibrium [*Garcia and Gordon*, 1992]). The units for $[O_2]$ were kept as μM since corresponding T and S data were not available to convert to μmol/kg. The $[O_2]$ and %Sat climatologies were created from over 800,000 and 700,000 QC'd discrete oxygen measurements, respectively, in the World Ocean Database 2009 (WOD09); all oxygen measurements were made by Winkler titration. The data went through further quality control by means of range checks as a function of depth and ocean region, statistical checks, and subjective flagging of data by the authors of the climatology. Relative to the mean climatological value, the standard error of data used to derive the climatology in the majority of the open ocean is 1–2 %Sat, except at depths where a strong oxycline exists [*Garcia et al.*, 2010].

2.2. Profiling Float Data

[6] Profiling floats that measure oxygen are equipped with either a Sea-Bird SBE43 or an Aanderaa Optode. The SBE43 is a Clark-type electrode, where oxygen diffuses across a membrane and is converted to OH^- ion at the gold cathode and oxygen concentration is proportional to the induced current [*Edwards et al.*, 2010]. The Optode is based on dynamic luminescence quenching, where the luminescence lifetime of a platinum porphyrine complex (the luminophore) is quenched in the presence of O_2. The luminophore is insulated by a gas permeable, optical isolation layer, and responds to the partial pressure of O_2 in air or solution [*Tengberg et al.*, 2006]. The claimed accuracy of the factory calibration for the SBE43 is 2% and the Optode is 5% or 8 μM, whichever is greater; both sensors are calibrated between 0% and 120% saturation. For further details on both sensors, the reader is referred to *D'Asaro and McNeil* [2013].

[7] Profiling float data were downloaded from the USGODAE website in May 2012. A total of 473 floats were identified as "oxygen" floats, based solely on the presence of an oxygen variable in the float's NetCDF data file (see *Thierry et al.* [2011] for a complete list and definition of oxygen-related variables in profiling float NetCDF files). One hundred eighty-five of the 473 floats were rejected based on the procedure summarized in Figure 1 and 288 floats were compared to the WOA09. First, the two variables that contain dissolved oxygen concentration data, DOXY and MOLAR_DOXY, were inspected and 90 floats were rejected because the oxygen variables only contained NaNs, indicating no data was stored in the variable.

[8] Duplicate profiles, profiles with missing location data, and profiles with missing T, S, P, or $[O_2]$ data were removed. Data were rejected for $[O_2] > 550$ μM, approximately 10% larger than the highest $[O_2]$ in the WOA09.

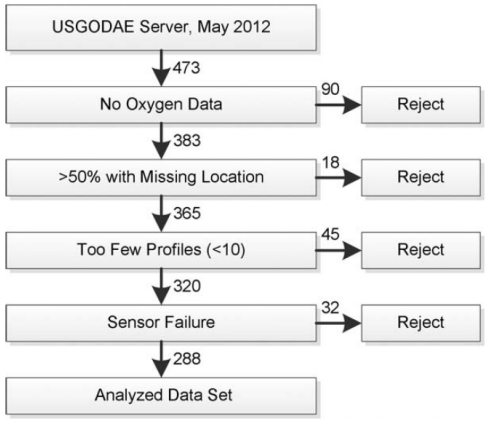

Figure 1. Flowchart of the selection process for floats deemed comparable to the WOA09. Numbers corresponding to the arrows represent the number of floats that were either rejected or accepted at each criterion.

The initial five profiles for floats equipped with the SBE43 were deleted prior to analysis, because these sensors can experience a rapid initial drift [*Martz et al.*, 2008]. Floats with fewer than 10 profiles remaining after this process were rejected, leaving a minimum of 10 profiles to compare to the climatology. Furthermore, if over half of the profiles had missing location data, the float was rejected; this criterion was used as a proxy for floats in the vicinity of Antarctica where seasonal sea ice reduces the reliability of the climatology. This eliminated 63 floats.

[9] The oxygen data for the remaining 320 floats were visually inspected for spikes and qualitatively assessed for unreasonable profiles and apparent sensor failures. In most cases, sensor failures occurred stepwise or over a course of several profiles. The most common symptoms were negative $[O_2]$, entire profiles where $[O_2] = 0$ μM, or significant increase in $[O_2]$ with depth. In cases where the sensor failed middeployment, data until then were used if more than 10 "good" profiles remained. This rejected 32 floats (10 SBE43, 7 Optodes, and 15 unidentified), resulting in 288 floats for further analysis.

[10] Oxygen data under the variable DOXY were assumed to have been properly adjusted for salinity and pressure effects, as described by *Thierry et al.* [2011]. Salinity and pressure corrections were applied to the oxygen data under the MOLAR_DOXY variable only when the oxygen sensor was an Optode; it was assumed the data were listed in units of μM, salinity setting (S0) was 0 (default manufacturer setting), and the pressure coefficient was 3.2% 1000 dB^{-1} [*Uchida et al.*, 2008]. %Sat was calculated following *Garcia and Gordon* [1992]. Quality controlled data distributed by the ARGO data centers (Delayed mode) for T, S, and P were used whenever available.

2.3. Comparison to the WOA09

[11] Climatological $[O_2]$ and %Sat values were first interpolated horizontally (by latitude and longitude) and temporally (by day of year) to the location and time of each float profile using a cubic spline method. If the profile was

taken within 1° latitude/longitude of a landmass, the nearest climatology location in space was used. Each resulting climatological profile was then interpolated vertically to the pressure or potential density measured by the float using cubic spline or linear methods, respectively. Linear interpolation was used for potential density surfaces because the spline method introduced significant noise (>10 μM) in weakly stratified regions of the water column, e.g., the surface mixed layer. Because vertical resolution of float measurements was equal to or higher than that of the climatology, no vertical averaging of the climatology was performed. For sensor drift calculations, oxygen concentrations from the climatology and float measurements were interpolated on 100 m intervals from 1500 to 2000 m.

2.4. Sensor Drift

[12] Sensor drift was determined as the average slope (least-squares regression) of the ΔO_2 versus time at depths between 1500 and 2000 m at 100 m intervals ($n = 6$), where $\Delta O_2 = [O_2]_{float} - [O_2]_{WOA}$. Sensor drift was calculated for floats with >1 year of data and ≥10 profiles deeper than 1500 m ($n = 170$). A trend in the deep ocean ΔO_2 was considered a proxy for sensor drift because the oxygen concentrations are very stable at this depth due to the lack of seasonal and annual signals [*Najjar and Keeling*, 1997]. In most cases, the residuals from the least-squares regression were slightly smaller when calculated on isopycnal surfaces than at constant depths because natural variability in the oxygen concentration due to vertical migration of isopycnal surfaces is accounted for. We therefore report sensor drift based on isopycnal surfaces (Table S1 in the supporting information). Four outliers (WMOID 5900345, 5902305, 5902308, and 5903260) were removed because the ΔO_2 time series changed stepwise when entering another water mass (most likely a mesoscale feature not captured in the climatology), unevenly distributed deep O_2 data biased the slope, or it was clear that the change in deep ΔO_2 was not due to sensor drift (see section 4 for details). This resulted in 166 floats analyzed for drift.

[13] Of the 166 floats, 74 exhibited sensor drift at the 95% CI based on a *t*-test (*t*-test, $p < 0.05$, df = 5) indicating a detectable drift relative to the climatology (labeled in Table S1). Sensor drift corrections were only applied to these floats prior to further analysis. This filtering criterion was applied to avoid overcorrecting the float data due to errors arising from uncertainties in the climatology (see section 4).

2.5. Oxygen Correction Coefficients

[14] Float specific oxygen dependent correction terms were determined by performing a model II linear regression [*York*, 1966] on $[O_2]_{float}$ versus $[O_2]_{WOA}$ and $\%Sat_{float}$ versus $\%Sat_{WOA}$ (Figure 2).

$$[O_2]_{WOA} = C_{0,[O2]} + C_{1,[O2]} \times [O_2]_{float} \quad (1)$$

$$\%Sat_{WOA} = C_{0,\%Sat} + C_{1,\%Sat} \times \%Sat_{float} \quad (2)$$

[15] The model II linear regression was used because there are errors associated with both float and WOA data. The $|\Delta O_2|$ increases in magnitude in strong vertical oxygen gradients due to a combination of dynamic sensor errors

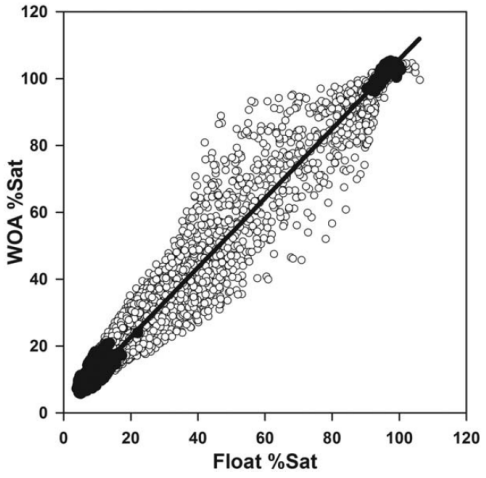

Figure 2. Plot used to calculate C_1 and C_0 for a float (WMO ID: 4900523). The data used and omitted ($|\partial O_2/\partial z| > 0.2$ μM m^{-1}) are represented by black circles and open circles, respectively. The solid line is the model II linear regression.

(e.g., response time and thermal lag), smoothing of real gradients in the WOA by averaging over multiple profiles, and natural vertical migration of the isopycnal surfaces by processes such as internal waves. Oxygen measurements taken in vertical gradients where $|\partial[O_2]/\partial z| > 0.2$ μM m^{-1} were omitted from the regression in order to minimize these errors. The corrected float oxygen, $[O_2]_{float}$ and $\%Sat_{float}$, was calculated by

$$[O_2]_{float}' = C_{0,[O2]} + C_{1,[O2]} \times [O_2]_{float} \quad (3)$$

$$\%Sat_{float}' = C_{0,\%Sat} + C_{1,\%Sat} \times \%Sat_{float} \quad (4)$$

where C_0 (offset) and C_1 (gain) are the coefficients from the model II regression. The standard error (SE) of the coefficients, and the root-mean-squared error (RMSE) of the fit are reported.

[16] Note that the proposed correction terms do not account for dynamic errors due to slow sensor response. At the present time, dynamic errors cannot be addressed for the global float oxygen data set because the errors are specific to sensor make and model, and this information is not necessarily documented in the metadata. Fortunately, the error is small in regions of low vertical oxygen gradient (see section 4), and thus restriction of data to these regions minimizes this bias.

2.6. Discrete Samples Near Float Profiles

[17] We (Riser, Johnson, and Gilbert) have deployed several floats near oceanographic time series stations (HOT, BATS, and Line *P*) and a repeat hydrography transect (CLIVAR section I06S), providing a unique opportunity to compare float sensor data to discrete samples taken near the time and location of a float profile (Table 1, $n = 14$, referred to as FloatVIZ floats hereafter). FloatVIZ

Table 1. FloatVIZ Correction Terms

Float	Days Apart	Distance (km)	$C_{0,\mathrm{Bottle}}$ [%Sat]	$C_{0,\mathrm{WOA}}$ [%Sat]	$C_{1,\mathrm{Bottle}}$	$C_{1,\mathrm{WOA}}$	RMSE Bottle [μM]	RMSE WOA [μM]	$O_2' - O_{2,\mathrm{Bottle}}$ (Surface) [μM (%Sat)][a]	$O_2' - O_{2,\mathrm{WOA}}$ (Surface) [μM (%Sat)][a]	$O_2' - O_{2,\mathrm{Bottle}}$ (Min. O_2) [μM (%Sat)]	$O_2' - O_{2,\mathrm{Bottle}}$ (Min. O_2) [μM (%Sat)]
5143[b,c,d]	3	20	−1.591	1.300	1.122	1.099	1.46	3.79	28.8 (9.7)	31.1 (10.4)	−3.0 (−0.9)	6.2 (1.9)
5145[b,d,e]	2	14	0.526	1.040	1.066	1.092	2.74	7.04	14.5 (6.8)	20.7 (9.6)	2.8 (0.9)	4.8 (1.5)
5146[b,d,f]	3	17	6.730	10.484	1.009	0.950	2.40	6.91	25.3 (7.6)	19.5 (5.8)	24.1 (7.1)	27.6 (8.2)
6391[b,d,g]	4	17	10.211	11.846	0.971	0.951	2.33	5.85	16.3 (7.5)	15.8 (7.3)	24.8 (8.9)	26.9 (9.6)
6401[b,d,e]	3	102	1.368	2.175	1.041	1.012	6.15	7.80	11.3 (5.4)	7.0 (3.3)	5.0 (1.6)	7.0 (2.2)
6403[b,d,e]	2	10	0.111	0.734	1.074	1.073	2.94	6.77	15.1 (7.1)	16.4 (7.7)	1.9 (0.6)	3.9 (1.2)
6891[b,d,e]	3	8	1.583	0.881	1.040	1.038	4.05	8.09	11.8 (5.6)	9.8 (4.6)	5.9 (1.9)	3.6 (1.2)
6976[b,d,e]	2	10	8.343	14.407	1.044	0.950	2.90	6.91	28.2 (12.3)	22.8 (9.9)	28.6 (10.3)	33.7 (12.2)
4900093[e,h,i]	12	14	0.651	1.877	1.066	1.031	2.67	6.42	14.9 (7.0)	10.4 (4.9)	3.1 (1.0)	6.5 (2.0)
4900235[e,h,i]	5	207	0.753	1.601	1.065	1.037	5.30	4.80	20.8 (6.9)	15.4 (5.1)	3.4 (1.0)	5.9 (1.7)
4901153[e,h,i]	2	63	−1.587	1.554	0.913	0.845	4.25	3.88	−34.4 (−11.8)	−48.4 (−16.6)	−6.6 (−2.0)	2.5 (0.8)
5900952[e,h,i]	12	19	−0.311	0.818	1.039	1.055	9.06	10.89	7.0 (3.3)	12.7 (6.1)	−0.1 (0.0)	3.9 (1.2)
5901069[d,e,h]	3	29	−0.348	0.840	1.105	1.050	4.27	9.24	20.8 (9.8)	12.0 (5.6)	1.3 (0.4)	3.9 (1.2)
5901336[d,e,h]	3	166	−0.818	−1.182	1.091	1.077	3.00	7.03	16.7 (6.2)	13.2 (6.2)	−1.0 (−0.3)	−2.4 (−0.7)
Average	5	50	1.83	3.46	1.05	1.02	3.82	6.81	14.1 (6.1)	11.3 (5.0)	6.44 (2.17)	9.58 (3.16)
SD.	4	64	3.76	4.89	0.05	0.07	1.96	1.92	15.4 (5.6)	18.3 (6.6)	11.01 (3.76)	11.1 (3.9)

[a] O_2' refers to corrected O_2 ($[O_2]$ and %Sat) using equations (3) and (4).
[b] Float data downloaded from http://www.mbari.org/chemsensor/floatviz.htm.
[c] Discrete sample collected on line P (Including Ocean Station Papa).
[d] Float equipped with Optode.
[e] Discrete sample collected at HOT.
[f] Discrete sample collected on the CLIVAR repeat section I06S.
[g] Discrete sample collected at BATS.
[h] Float data downloaded from USGODAE website.
[i] Float equipped with SBE43.

data were downloaded from http://www.mbari.org/chemsensor/floatviz.htm and the USGODAE website. Corresponding discrete samples were downloaded from the time series' websites or provided directly from PIs for data not yet publically available.

[18] O_2 from the hydrographic casts was interpolated vertically for comparison to the float data on isobaric (dbar), isothermal (θ), and isopycnal (σ) surfaces corresponding to float measurement points. C_0 and C_1 for $[O_2]$ and %Sat were calculated on the three different vertical grids, for a total of six different combinations. Finally, the corrected oxygen data based on the discrete samples and WOA09 were compared.

2.7. Recalibration of Optode Sensors

[19] Seven float Optodes (Aanderaa model 3830) were calibrated at CSIRO, achieving an accuracy of <1 μM throughout the oceanic range of temperature and O_2. The sensor response (phase shift) was recorded at eight different values of $[O_2]$ between 0 %Sat and 130 %Sat, and repeated at five different temperatures between 1°C and 30°C ($n = 40$). Response of each sensor was calibrated to oxygen concentration determined by triplicate Winkler titration. Data were fit to the Stern-Volmer equation using a nonlinear multivariate regression [*Uchida et al.*, 2008]. The average root-mean-squared error (RMSE) of the fit for the seven Optodes was 0.60 ± 0.05 μM (1σ).

3. Results

3.1. Sensor Drift

[20] Sensor drift was categorized by sensor type, i.e., SBE43 or Optode (Figure 3). The average sensor drift for all floats was 0.2 ± 2.8 μM yr^{-1} (1σ, $n = 166$). The average Optode and SBE43 drift was 0.9 ± 2.7 μM yr^{-1} (1σ, $n = 102$) and -1.0 ± 2.7 μM yr^{-1} (1σ, $n = 62$), respectively. Sensor type was unidentified for two of the 166 sensors, resulting in a total of 164 floats for this comparison. A higher percentage of floats equipped with SBE43 (53%) had a detectable drift relative to the climatology (i.e., sensor drift significantly different than 0 at the 95% CI) compared to Optodes (37%).

3.2. Float Oxygen Correction

[21] When comparing float data to discrete data, corrections based on %Sat on isobaric surfaces yielded the lowest standard error for C_1 (SE_{C1}) (Table 2); although the improvement was not statistically significant when switching from $[O_2]$ to %Sat ($p > 0.15$), or changing the vertical grid ($p > 0.1$). However, corrections based on %Sat are

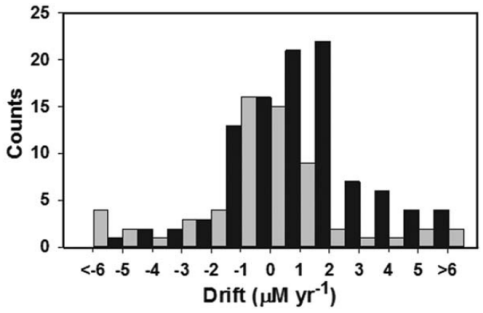

Figure 3. Histogram showing the frequency of sensor drift by sensor type: Optode (black, $n = 105$) and SBE43 (gray, $n = 63$).

Table 2. Mean Standard Error for $C_1 \pm$ SD for FloatVIZ Floats[a]

	$[O_2]$	% Sat
P	0.017 ± 0.015	0.011 ± 0.005
σ	0.018 ± 0.015	0.015 ± 0.011
θ	0.020 ± 0.014	0.017 ± 0.012

[a]Results from linear regression of FloatVIZ versus discrete samples, interpolated onto isobaric (P), isothermal (θ), or isopycnal (σ) surfaces using $[O_2]$ and %Sat ($n = 14$). The SD is calculated from the 14 SE_{C1} from FloatVIZ floats.

probably preferable because $[O_2]$ responds rapidly to changes in solubility that are driven by temperature, and using %Sat would largely correct for these changes. Since the climatology is gridded on isobaric surfaces, unless otherwise noted, correction coefficients hereafter were calculated using %Sat on isobaric surfaces and referred to simply as C_0 and C_1.

[22] The correction results based on both discrete samples and the WOA09 for the FloatVIZ floats are summarized in Table 1. On average, RMSE was lower for bottle corrections compared to WOA corrections (3.8 versus 6.8 μM); although, due to the high number of samples, SE for floats versus WOA (see Table S1) is lower than SE reported in Table 2 for float versus discrete samples. On average, the two methods agreed well; the difference of the applied correction (WOA – discrete) at the surface was -2.8 ± 5.5 μM, or -1.06 ± 2.2 %Sat (1σ).

[23] Correction coefficients of the 288 floats from the USGODAE server are shown in Figure 4 and reported in Table S1. The correction coefficients for six floats were rejected (noted in Table S1) after visual inspection indicated abrupt changes in temperature, salinity, and O_2 in the floats with no corresponding changes in $O_{2,WOA}$. This was most likely due to water masses not accurately captured by the climatology (e.g., interannual variability of frontal zones); these floats are not included in further discussions. The average Δ%Sat at the surface, where $\Delta\%Sat = \%Sat_{float} - \%Sat_{WOA}$, was -6.11 ± 8.8 (1σ) %Sat precorrection and -0.37 ± 2.3 %Sat post correction. The mean ($\pm 1\sigma$) C_0, C_1, and RMSE [μM (%Sat)] calculated from equation (4) for all floats was 5.47 ± 9.4, 1.01 ± 0.14, and 8.9 (2.99%) $\pm$ 3.0 (1.1%), respectively.

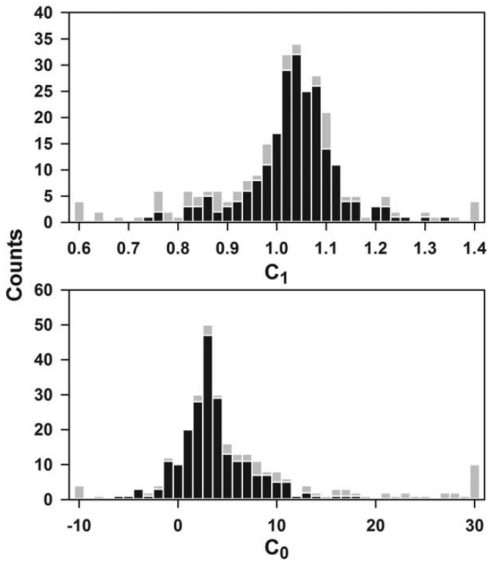

Figure 4. Stacked bar plot of the slope (C_1) and intercept (C_0) ($n = 282$). Floats where $SE_{C1} < 0.006$ ($n = 217$) and $SE_{C1} > 0.006$ are shown in black and gray, respectively.

4. Discussion

4.1. Sensor Drift

[24] Of the 166 floats analyzed for sensor drift, less than half had a detectable drift relative to the climatology ($n = 74$). This result shows that the majority of oxygen profiling floats are stable for years. The climatology is constructed using historical data spanning many decades, but the sampling is sparse in both time and space. This complicates using the climatology to correct a data set that is relatively short term in length. A climatology-based correction is therefore prone to errors in areas where deep oxygen is subject to short-term variability due to deep ventilation such as frontal zones and the subpolar North Atlantic, potentially creating a bias in the calculated drift. For example, *Stendardo and Gruber* [2012] show interannual variability of O_2 as large as 15 μM in the North Atlantic Intermediate Water (~800–900 m), and the majority of the floats with detectable "drift" were in fact located in the North Atlantic.

[25] For most of the floats with detectable drift, including all those equipped with an Optode sensor, a positive drift was just as likely as a negative drift, relative to the climatology. Experience with drift of the SBE43 [*Gruber et al.*, 2010] and observed shifts in Optode calibrations [*Bushinsky and Emerson*, 2013; *D'Asaro and McNeil*, 2013] all indicate that these sensors primarily drift toward lower reported oxygen concentration. This suggests that short-term variability in oxygen distributions relative to the climatology introduces significant uncertainty in the calculated sensor drift, in both a positive and negative direction.

[26] Only for the SBE43 is there seen to be a second mode in the frequency histogram of sensor drift (Figure 3), suggesting that some of these sensors do experience significant drift, a result consistent with previous observations [*Gruber et al.*, 2010; *Martz et al.*, 2008]. Studies have shown that Optodes on profiling floats produce highly stable data for years [*Körtzinger et al.*, 2005; *Tengberg et al.*, 2006], which agrees with the indication that changes of the Optode sensor, relative to climatology are due to changes in ocean oxygen distributions or errors in the climatology. However, since the number of floats in the second mode (and possibly a third in the high extreme) is small, it is difficult to say with confidence if this phenomenon is real. Further independent data are necessary to verify these results.

[27] Comparing float oxygen data to a regional climatology based on recent historical data, an approach adopted by the ARGO community to QC salinity data [*Owens and Wong*, 2009], would better address the question of sensor drift. Unfortunately, currently, there is no global oxygen

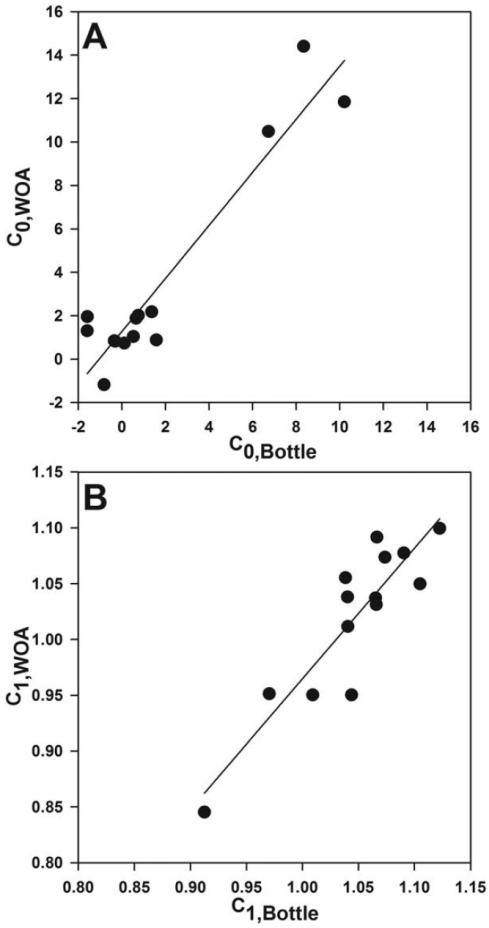

Figure 5. Scatter plot of (a) $C_{0,\%Sat}$ and (b) $C_{1,\%Sat}$ for the 14 FloatVIZ floats from bottle samples and the WOA. Linear regressions, shown as solid lines, yielded $R_{C1} = 0.89$, $R_{C0} = 0.94$.

data set that is dense enough to apply this method for float oxygen. However, it is encouraging that the majority of floats showed no drift in this study, suggesting that an array of properly calibrated floats is capable of producing a reliable oxygen data set for biogeochemical studies.

4.2. Method Assessment

[28] The comparison of WOA versus discrete sample correction coefficients for the 14 FloatVIZ floats shows a strong correlation between the two methods (Figure 5, $R_{C1} = 0.89$, $R_{C0} = 0.94$), suggesting that the two methods are correcting for similar sources of error. The average difference between the two corrections (1.1 ± 2.2 %Sat at the surface, Table 1) suggests that either approach is capable of improving the first-order errors often observed in factory sensor calibrations. For the bottle-based correction, the implicit assumption is made that a single cast is sufficient to provide a reliable correction throughout the life of the float. Local gradients and timing mismatch between a single hydrographic profile and a float profile, or rapid initial sensor drift in the case of SBE43 can lead to errors in this approach. As seen in Table 1, most discrete samples are taken days, and tens of kilometers apart from the profiling float; in other cases the spatial and temporal discrepancies may be even larger. Any natural processes that alter oxygen concentrations during that interval in space and time (e.g., temperature changes in the mixed layer) would lead to errors in the correction terms derived from a single hydrographic profile. On the other hand, the climatology-based approach is data limited over large regions of the ocean, leading to increased uncertainty in the correction coefficients (Figure 6). Nonetheless, the agreement between the two methods implies that either approach is capable of correcting the float oxygen data to several %Sat at the surface.

[29] The benefit of a WOA-based correction is that it provides a postdeployment QC protocol for all floats. The vast majority of oxygen floats are not deployed with a corresponding hydrographic cast. As oxygen sensors become a mainstay on profiling floats, increasing numbers will be deployed from ships without the capability to perform hydrographic casts. For example, many of the profiling floats in the Argo program are deployed from Ships of

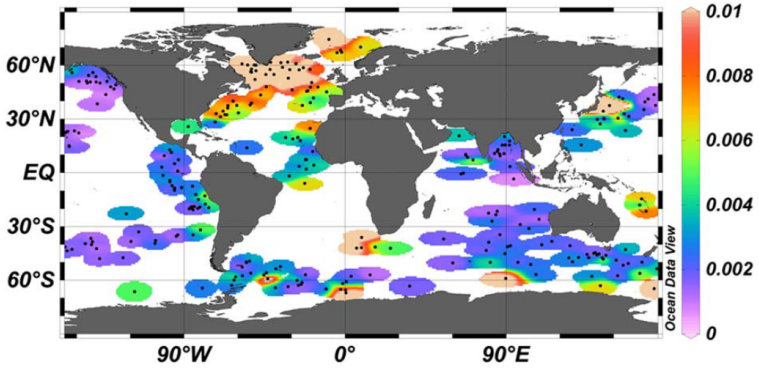

Figure 6. Distribution of SE_{C1} from equation (2). Location of floats was determined by mean latitude and longitude. Majority of high SE_{C1} values are observed in the North Atlantic.

Opportunity to achieve the target global coverage of the array. If profiling floats with oxygen sensors are to reach coverage similar to the existing Argo array, QC methods applicable to all floats will be a critical requirement.

[30] The global distribution of the standard error of C_1 (SE_{C1}) suggests that this method is more robust in certain regions than in others (Figure 6). A low SE_{C1} results from a properly functioning oxygen sensor, combined with an accurate representation of O_2 in the climatology through the entire O_2 range experienced by the float. A high SE_{C1} suggests an error in either sensor or climatology (or both). It is clear that the majority of floats with a high SE_{C1} are located in the North Atlantic, which strongly suggests that the method is less robust in this basin. A SE_{C1} threshold of 0.006 (the highest observed for the FloatViz floats versus WOA) was chosen to select floats with agreement to the climatology similar to the 14 FloatViz floats. Two hundred twenty profiling floats remained after this final filtering criterion was applied, eliminating most floats at latitudes north of 30°N in the Atlantic (Table S1). The C_0 and C_1 ($\pm 1\sigma$) of the remaining 220 floats are 3.22 ± 3.7 and 1.02 ± 0.09, respectively, and the average surface Δ%Sat improved from -5.19 ± 7.9 %Sat to -0.20 ± 2.3 %Sat. Thus on average, float oxygen data were corrected by about 5 %Sat at solubility equilibrium (i.e., $3.22 + 1.02 \times 100 - 100 = 5.2$). The relatively large uncertainty range of ± 7.9 %Sat indicates that many floats are likely to disagree with the WOA by more than 10 %Sat at equilibrium, due to both calibration error and errors in the WOA.

[31] The correction coefficients for floats rejected in this final criterion are not necessarily unreliable. For example, regression analysis through a narrow range of O_2 can lead to high SE_{C1}, but provide sufficient C_1 and C_0 for that O_2 range. However, applying coefficients for such floats outside of the observed O_2 range is suspect, and should be avoided.

[32] The correction coefficients for the 220 floats were separated by sensor type (Table 3). C_0 for both sensors and C_1 for SBE43 were significantly different from 0 and 1, respectively at the 99.99% confidence level ($p < 0.0001$), whereas C_1 for the Optode was not statistically different from unity ($p = 0.30$). A t-test analysis showed that both C_0 and C_1 between the two sensors were significantly different ($p < 0.01$), suggesting a possible difference between the quality of factory calibration. On average, it seems that Optodes tend to be biased low by a constant %Sat, whereas the SBE43 has an error in gain. However, the large standard deviation of the coefficients for both sensors indicates that the quality of calibration varies significantly from sensor to sensor.

4.3. Corrections in Low Oxygen Regimes

[33] Recent studies suggest that the World Ocean Atlas overestimates O_2 in most suboxic/anoxic regions [*Fuenzalida et al.*, 2009; *Bianchi et al.*, 2012], therefore O_2' in low oxygen regimes may be overestimated. This error is clearly demonstrated by a float equipped with both an Optode and an ISUS nitrate sensor that was deployed in the eastern tropical Pacific by Riser and Johnson (Figure 7) [*Johnson et al.*, 2013]. The $[O_2]_{float}$ is <1 μM for several hundred meters in the core of the oxygen minimum zone (OMZ), whereas $[O_2]_{WOA}$ ranges from 5 to 32 μM. The

Table 3. Correction Coefficients Divided by Sensor Type for Floats Where $SE_{C1} < 0.006$

	Optode ($n = 130$)	SBE43 ($n = 87$)
C_0 [%Sat] $\pm$ SD	4.33 ± 3.5	1.96 ± 3.2
$C_1 \pm$ SD	1.007 ± 0.098	1.044 ± 0.067

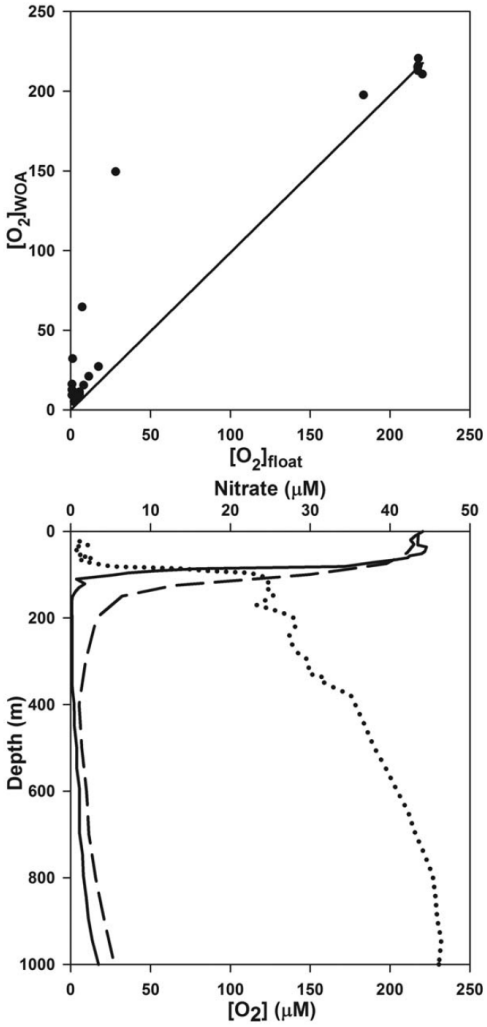

Figure 7. (top) Comparison of $[O_2]_{float}$ to $[O_2]_{WOA}$ demonstrates the mismatch at low O_2 (FloatVIZ ID: 7558). Climatology oxygen values are positive in the oxygen minimum, while the float is nearly zero (<1 μM). The line shown is a linear regression using only the surface value (forcing the y intercept through zero). (bottom) profiles from $[O_2]_{float}$ (solid line), $[O_2]_{WOA}$ (dashed line), and $[NO_3^-]_{float}$ (dotted line). Reversal of nitrate is indicative of nitrate reduction, and float oxygen values are <1 μM in this region.

inversion of the nitrate profile in the same depth range provides strong evidence of water column denitrification, which only occurs under anoxic conditions, confirming that $[O_2]_{float}$ is more accurate than $[O_2]_{WOA}$ for this particular float near zero $[O_2]$.

[34] A similar trend was observed for the global float array. $[O_2]_{float}$ in known permanent anoxic OMZs (northern Indian Ocean and eastern tropical Pacific) ranged between 0 μM and 5 μM, whereas the corresponding $[O_2]_{WOA}$ were 6–12 μM. This is in good agreement with *Bianchi et al.* [2012], who show an average bias in the WOA of +6 μM in hypoxic regions. These results suggest that oxygen sensor calibration is robust at low O_2 [*D'Asaro and McNeil*, 2013], and a positive offset correction is not appropriate for floats in OMZs. A correction based on equation (2) will bias the offset high due to this error in the climatology. For such floats, only adjusting the gain while forcing the offset to 0 should minimize this error.

[35] One straightforward approach to calculate the gain is to compare the surface $\%Sat_{float}$ to the surface $\%Sat_{WOA}$ using >1 year of data, i.e., $C_1 = \text{mean}(\%Sat_{WOA}/\%Sat_{float})$ at the surface (Table S1). It is counterintuitive to restrict the float O_2 data to the most dynamic region of the water column to obtain correction coefficients. However, due to rapid gas exchange and a constant atmospheric oxygen concentration, %Sat remains very close to solubility equilibrium at the surface over an annual cycle [*Najjar and Keeling*, 1997]. Therefore, a robust estimate of the gain can be obtained from ≥1 year of surface data. This method is appealing due to its simplicity; however, it has one large drawback: float oxygen data corrected using this method cannot provide an independent estimate of net community production (NCP). Most of the ocean is a few %Sat above solubility equilibrium when averaged annually, due to biological activity and bubble injection [*Hamme and Emerson*, 2006]. If float oxygen data are corrected to the average annual surface %Sat of the WOA09, then subsequent calculations of NCP will always reflect biological activity that is necessary to maintain the level of supersaturation in the climatology. Therefore, studies of biological production in the euphotic zone would be biased by this simple correction. In order to obtain independent estimates of NCP using profiling float oxygen data, a calibration protocol that enables the sensors to constrain oxygen concentrations more accurately than the climatology must be established.

4.4. Sources of Oxygen Sensor Error

[36] Sources of error in float oxygen can be categorized as either calibration errors or dynamic errors (Table 4). The method described here corrects for the calibration errors and sensor drift (a dynamic error); yet, it is important to keep in mind that other dynamic errors remain uncorrected. At minimum, correction of dynamic errors beyond sensor drift requires knowledge of sensor manufacturer, model, and calibration coefficients. These values are not sufficiently tabulated in the global float oxygen metadata, making it impractical for any single research group to analyze the data set as a whole for dynamic errors. However, a brief discussion on dynamic errors of the Aanderaa Optode is warranted, as this has been the dominant sensor deployed in the global float array for many years. For a detailed review on the SBE43, the reader is referred to *Edwards et al.* [2010].

Table 4. Sources of Errors for Profiling Float Oxygen

Error Type	Correction
Calibration Errors	
$[O_2]$ and T coefficient(s)	Apply linear correction using C_0, C_1 [this work]
Pressure coefficient(s)	3.2%/1000 dBar [*Uchida et al.*, 2008]
Dynamic Errors	
Delayed T response	Use sensors equipped with fast response thermistor
Response time	Use oxygen gradient with τ fit [this work]
Drift	Linear regression on ΔO_2 [this work]

[37] Delayed temperature errors arise when there is a thermal disequilibrium between the sample water in contact with the oxygen sensing element and the thermistor. The resulting oxygen measurements are affected by temperature through (1) the temperature dependency of the sensor itself and (2) the $[O_{2Sat}]$ temperature dependence used to convert the raw sensor output (phase shift) to oxygen concentration [*Garcia and Gordon*, 1992]. The thermistor is embedded deep inside of the sensor for the Model 3830, the most common Optode model deployed on profiling floats, leading to a greater potential for thermal disequilibrium. Discrepancies between the temperature reading from the CTD and these Optodes can frequently be as large as 1.5°C. The oxygen error due to this temperature discrepancy is sensor specific and can only be quantified if the temperature response of the sensor is well characterized. Two randomly selected Optodes generated errors on the order of 15 μM for a 1.5°C shift in input temperature. An accurate estimate of the probable range of this error within the float array would require access to a distribution of calibration coefficients from many sensors, data which were not publicly available at the time of this work. Preliminary results from Optodes with a faster thermistor response (Model 4330F) suggest improved performance [*Riser*, 2012]. However, this sensor model was only recently introduced into the float array and its performance was not assessed in this study.

[38] The Optode response time to oxygen (τ ~23 s at 25°C) [*Uchida et al.*, 2008] can lead to significant errors when a float ascends through a strong oxygen gradient. The actual oxygen concentration can be estimated ($[O_2]_{model}$) from the reported concentration ($[O_2]_{float}$) based on the oxygen gradient and τ as

$$[O_2]_{model} = [O_2]_{float} - \tau \frac{\partial [O_2]}{\partial t}\left(1 - e^{\left(-\frac{t}{\tau}\right)}\right) \quad (5)$$

where $\partial[O_2]/\partial t$ is the oxygen gradient with respect to time, assuming a float ascent rate of 10 cm s^{-1}. This simple model was created based on equations used to model thermal lag of profiling CTDs [*Johnson et al.*, 2007]. Previous work suggests that τ is temperature dependent (longer at lower temperatures), and may be sensor specific [*Uchida et al.*, 2008]. The modeled oxygen error resulting from different τ using an actual profile is shown in Figure 8. When a constant τ of 30 s throughout the profile is assumed, oxygen errors as large as 15 μM were calculated during the strongest oxygen gradient (~5 μM m^{-1}). It is noteworthy

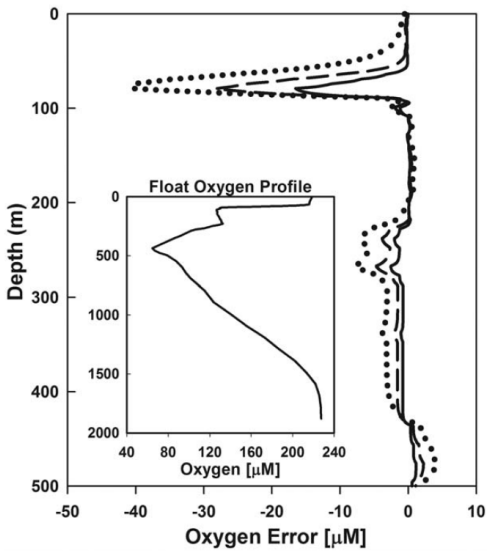

Figure 8. The depth profile of the modeled oxygen error ($[O_2]_{float}$–$[O_2]_{model}$) for float 1900650 on 4 September 2007 between 0 and 500 m, assuming a τ of 30, 60, and 120 s (solid, dashed, and dotted lines, respectively). Inset shows the full oxygen profile.

that such a large oxygen gradient is rare, and a more commonly observed gradient of 1 μM m^{-1} results in a $\sim$6 μM error. However, due to uncertainties associated with τ, this correction was not applied to the float oxygen data. Since data were selected from regions where $|\partial[O_2]/\partial z| < 0.2$ μM m^{-1}, the errors due to slow sensor response should be minimal. In order to accurately correct this error, further investigation on sensor response over a range of temperature and pressure is required.

4.5. Laboratory Predeployment Calibration of Optodes

[39] A float data set, corrected to the WOA09, will reflect any errors inherent to the climatology; this may not be satisfactory for some biogeochemical studies. For example, independent estimates of NCP require the accuracy of the oxygen measurements to be <1 %Sat near the surface [*Emerson et al.*, 2008]. Currently, the uncertainties inherent to the climatology are slightly larger than this requirement (1–2 %Sat for large parts of the surface ocean) due to sparse sampling in both time and space. A more direct and straightforward approach would be to properly calibrate the sensors prior to deployment. The Optode can achieve an accuracy of $\sim$1 μM between 0°C and 30°C when individual sensors are calibrated against discrete samples analyzed by Winkler titration [*Bittig et al.*, 2012; *Bushinsky and Emerson*, 2013; *D'Asaro and McNeil*, 2013]. This is a significant improvement over the current factory calibration for Optodes, which claims an accuracy of "5% or 8 μM, whichever is larger." Discrepancies larger than the claimed accuracy have been reported [*Kobayashi et al.*, 2006] and were also observed in this study as described above. To our knowledge, most, if not all oxygen data archived at USGO-DAE uses factory derived calibration coefficients. Thus, an establishment of a proper sensor calibration protocol is a critical step to meet the stringent requirements desired by the community.

[40] In 2011, Tilbrook and Neill deployed seven floats in the Southern Ocean equipped with Optodes that were recalibrated in-house. Correction coefficients from the WOA were calculated using both the factory calibrations and the laboratory recalibrations (Table 5). The C_1 obtained using laboratory recalibrated sensors was significantly closer to unity (1.02 ± 0.02 and 1.08 ± 0.02 for recalibration and factory calibration, respectively), reflecting the improved calibration protocol. On average, the laboratory calibrations agreed with the WOA by $\sim$5 %Sat at the surface, compared to $\sim$17 %Sat for the factory calibrations.

[41] Even after laboratory recalibration, all seven Optodes recorded oxygen values that were low relative to the WOA ($C_0 = 3$, Table 5), suggesting either a bias in the climatology in this region, or an unidentified mechanism occurring between calibration and deployment that systematically decreases the sensor measurement. A decrease in sensor response (i.e., a drift toward lower oxygen concentration) for Optodes was also observed in recent studies and attributed to decreased oxygen sensitivity of the sensor [*Bushinsky and Emerson*, 2013; *D'Asaro and McNeil*, 2013]. However, based on previous observations [*Körtzinger et al.*, 2005; *Tengberg et al.*, 2006] and results from this study, data from Optodes deployed on profiling floats are stable for years. One hypothesized mechanism that explains these two seemingly contradictory observations is migration/diffusion of the luminophore in the oxygen sensing foil over time, leading to lower oxygen values. This effect would be temperature dependent and minimal at low temperatures, providing an explanation for the observation that Optodes on profiling floats are stable for years (floats spend the majority of the time in the cold deep ocean). Further mechanistic studies of this phenomenon are necessary to establish a stringent calibration and storage protocol for oxygen sensors. However, it is encouraging that recalibrated sensors exhibited significantly better agreement with the WOA. We therefore recommend that researchers contributing to the global oxygen float array recalibrate oxygen sensors prior to deployment.

5. Conclusions

[42] Float specific oxygen sensor correction terms for 288 profiling floats are reported based on a comparison to

Table 5. Correction Coefficients for Laboratory Recalibrated Optodes

Float	$C_{0,\ Factory}$	$C_{0,\ Lab}$	$C_{1,\ Factory}$	$C_{1,\ Lab}$
1901152	7.744	2.761	1.059	0.991
1901153	6.385	2.278	1.085	1.030
1901154	5.874	2.824	1.099	1.022
1901155	6.056	1.191	1.111	1.051
1901157	6.780	4.382	1.075	1.007
1901158	6.798	2.480	1.057	1.004
1901159	7.437	3.678	1.078	1.014
Avg $\pm$ SD	6.72 ± 0.69	3.00 ± 1.14	1.08 ± 0.02	1.02 ± 0.02

the World Ocean Atlas. The correction approach was validated for a small subset of the global array where additional information (bottle samples or sensor recalibration) was available. The corrections were shown to improve the sensor data reported in the USGODAE database. The results suggest that the corrected float oxygen values constrain oxygen concentrations to several %Sat at the surface. Oxygen data from floats deployed at high latitude in the North Atlantic and parts of the Southern Ocean deviated from a simple linear relationship with the climatology, suggesting this method is not robust in these areas due to complex hydrography and/or sparse coverage in the WOA. Correcting float data in areas with low O_2 by only adjusting the gain may be more appropriate.

[43] Further limitations of the correction based on gain only should be noted. For floats deployed in areas where there is a weak oxygen gradient throughout the water column (e.g., North Atlantic or Southern Ocean), applying a gain-only correction can introduce errors of up to 5% in the midwater column relative to the climatology. This could be due to uncharacterized dynamic sensor errors, redistribution of oxygen in the midwater column, nonlinear response of the sensor to $[O_2]$, or improperly characterized temperature coefficients. Overall, a gain-only (C_1) correction, applied to floats in OMZs, coupled with an offset + gain correction (C_0 and C_1) for all other floats would likely produce the most accurate float oxygen data set, given the present limitations of the WOA. Accordingly, the coefficients for both corrections are reported in Table S1.

[44] In order for float data to be used to improve upon the climatology, the accuracy of the calibration protocol must be better than the errors in the climatology, i.e., 1–2 %Sat for most of the world's oceans. Ideally, float oxygen data from sensors that have undergone a proper calibration protocol would be verified using a climatology based on recent historical data; an approach adopted for float salinity data QC. However, due to the uncertainties associated with the WOA09 as discussed above, this approach seems currently untenable unless there is a significant increase in the number of independent oxygen measurements. One promising alternative is to validate oxygen measurements in situ using atmospheric oxygen measurements [*Bushinsky and Emerson*, 2013], a methodology that has yet to be tested on profiling floats. The calibration process, however, is not necessarily trivial, is labor and time intensive, and may cost as much as the sensor itself; a fact often underappreciated by the scientific community. Consequently, the most practical solution would appear to be agreement of the community to send Optode sensors to a certified facility(s) capable of high accuracy calibration, until it can be demonstrated that factory calibrations are of equal quality.

[45] **Acknowledgments.** This work was supported by NOPP award N00014-10-1–0206. We would like to thank Steve Emerson and Rod Johnson for providing discrete sample data that were not publically available.

References

Bianchi, D., J. P. Dunne, J. L. Sarmiento, and E. D. Galbraith (2012), Data-based estimates of suboxia, denitrification, and N_2O production in the ocean and their sensitivities to dissolved O_2, *Global Biogeochem. Cycles*, *26*, GB2009, doi:10.1029/2011GB004209.

Bittig, H. C., B. Fiedler, T. Steinhoff, and A. Körtzinger (2012), A novel electrochemical calibration setup for oxygen sensors and its use for the stability assessment of Aanderaa Optodes, *Limnol. Oceanogr.Methods*, *10*, 921–933, doi:10.4319/lom.2012.10.921.

Bohme, L., and U. Send (2005), Objective analyses of hydrographic data for referencing profiling float salinities in highly variable environments, *Deep Sea Res., Part II*, *52*(3–4), 651–664, doi:10.1016/j.dsr2.2004.12.014.

Bushinsky, S. M., and S. Emerson (2013), A method for in-situ calibration of Aanderaa oxygen sensors on surface moorings, *Mar. Chem.*, *155*, 22–28, doi:10.1016/j.marchem.2013.05.001.

D'Asaro, E. A., and C. McNeil (2013), Calibration and stability of oxygen sensors on autonomous floats, *J. Atmos. Oceanic Technol.*, *30*, 1896–1906, doi:10.1175/JTECH-D-12–00222.1.

Edwards, B., D. Murphy, C. Janzen, and N. Larson (2010), Calibration, response, and hysteresis in deep-sea dissolved oxygen measurements, *J. Atmos. Oceanic Technol.*, *27*(5), 920–931, doi:10.1175/2009JTECHO693.1.

Emerson, S. R., C. Stump, and D. Nicholson (2008), Net biological oxygen production in the ocean: Remote in situ measurements of O2 and N2 in surface waters, *Global Biogeochem. Cycles*, *22*, GB3023, doi:10.1029/2007GB003095.

Fuenzalida, R., W. Schneider, J. Garcés-Vargas, L. Bravo, and C. Lange (2009), Vertical and horizontal extension of the oxygen minimum zone in the eastern South Pacific Ocean, *Deep Sea Res., Part II*, *56*(16), 992–1003, doi:10.1016/j.dsr2.2008.11.001.

Garcia, H. E., and L. I. Gordon (1992), Oxygen solubility in seawater: Better fitting equations, *Limnol. Oceanogr.*, *37*(6), 1307–1312.

Garcia, H. E., R. A. Locarnini, T. P. Boyer, J. I. Antonov, O. K. Baranova, M. M. Zweng, and D. R. Johnson (2010), *World Ocean Atlas 2009, Volume 3: Dissolved Oxygen, Apparent Oxygen Utilization, and Oxygen Saturation, NOAA Atlas NESDIS 70*, edited by S. Levitus U.S. Gov. Print. Off., Washington, D. C.

Gruber, N., S. C. Doney, S. R. Emerson, D. Gilbert, T. Kobayashi, A. Körtzinger, G. C. Johnson, K. S. Johnson, S. C. Riser, and O. Ulloa (2010), Adding oxygen to argo: Developing a global in situ observatory for ocean deoxygenation and biogeochemistry, *Proceedings of Ocean Obs '09: Sustained Ocean Observations and Information for Society*, Vol. 2, *ESA Publication WPP-306*, edited by J. Hall et al., doi:10.5270/OceanObs09.cwp.39.

Hamme, R. C., and S. R. Emerson (2006), Constraining bubble dynamics and mixing with dissolved gases: Implications for productivity measurements by oxygen mass balance, *J. Mar. Res.*, *64*(1), 73–95, doi:10.1357/002224006776412322.

Johnson, G. C., J. M. Toole, and N. G. Larson (2007), Sensor corrections for Sea-Bird SBE-41CP and SBE-41 CTDs*, *J. Atmos. Oceanic Technol.*, *24*(6), 1117–1130, doi:10.1175/JTECH2016.1.

Johnson, K. S., S. C. Riser, and D. M. Karl (2010), Nitrate supply from deep to near-surface waters of the North Pacific subtropical gyre, *Nature*, *465*(7301), 1062–1065, doi:10.1038/nature09170.

Johnson, K. S., L. J. Coletti, H. W. Jannasch, C. M. Sakamoto, D. D. Swift, and S. C. Riser (2013), Long-term nitrate measurements in the ocean using the in situ ultraviolet spectrophotometer: Sensor integration into the apex profiling float, *J. Atmos. Oceanic Technol.*, *30*, 1854–1866, doi:10.1175/JTECH-D-12–00221.1.

Juranek, L. W., R. A. Feely, D. Gilbert, H. Freeland, and L. A. Miller (2011), Real-time estimation of pH and aragonite saturation state from Argo profiling floats: Prospects for an autonomous carbon observing strategy, *Geophys. Res. Lett.*, *38*, L17603, doi:10.1029/2011GL048580.

Kihm, C., and A. Körtzinger (2010), Air-sea gas transfer velocity for oxygen derived from float data, *J. Geophys. Res.*, *115*, C12003, doi:10.1029/2009JC006077.

Kobayashi, T., T. Suga, and N. Shikama (2006), Negative bias of dissolved oxygen measurements by profiling floats, *Umi no kenkyu*, *15*(6), 479–498.

Körtzinger, A., J. Schimanski, and U. Send (2005), High quality oxygen measurements from profiling floats: A promising new technique, *J. Atmos. Oceanic Technol.*, *22*(3), 302–308.

Martz, T. R., K. S. Johnson, and S. C. Riser (2008), Ocean metabolism observed with oxygen sensors on profiling floats in the South Pacific, *Limnol. Oceanogr. Methods*, *53*(5–2), 2094–2111.

Najjar, R. G., and R. F. Keeling (1997), Analysis of the mean annual cycle of the dissolved oxygen anomaly in the World Ocean, *J. Mar. Res.*, *55*, 117–151.

Owens, W. B., and A. P. S. Wong (2009), An improved calibration method for the drift of the conductivity sensor on autonomous CTD profiling floats by θ–S climatology, *Deep Sea Res., Part I*, *56*(3), 450–457, doi:10.1016/j.dsr.2008.09.008.

Prakash, S., T. M. B. Nair, T. V. S. U. Bhaskar, P. Prakash, and D. Gilbert (2012), Oxycline variability in the central Arabian Sea: An Argo-oxygen study, *J. Sea Res.*, *71*, 1–8, doi:10.1016/j.seares.2012.03.003.

Riser, S. C. (2012), The use of dissolved oxygen sensors on profiling floats: Technical challenges and data quality, *Eos Trans. AGU*, *83*(4), Ocean Sci. Meet. Suppl., Abstract 11537.

Riser, S. C., and K. S. Johnson (2008), Net production of oxygen in the subtropical ocean, *Nature*, *451*(7176), 323–325, doi:10.1038/nature06441.

Stendardo, I., and N. Gruber (2012), Oxygen trends over five decades in the North Atlantic, *J. Geophys. Res.*, *117*, C11004, doi:10.1029/2012JC007909.

Tengberg, A., et al. (2006), Evaluation of a lifetime-based optode to measure oxygen in aquatic systems, *Limnol. Oceanogr. Methods*, *4*, 7–17.

Thierry, V., D. Gilbert, and T. Kobayashi (2011), Processing Argo OXYGEN data at the DAC level, Argo Project Office, Toulouse, France. [Available at http://www.argodatamgt.org/content/download/2928/21973/file/.]

Uchida, H., T. Kawano, I. Kaneko, and M. Fukasawa (2008), In situ calibration of optode-based oxygen sensors, *J. Atmos. Oceanic Technol.*, *25*(12), 2271–2281, doi:10.1175/2008JTECHO549.1.

Whitmire, A. L., R. M. Letelier, V. Villagran, and O. Ulloa (2009), Autonomous observations of in vivo fluorescence and particle backscattering in an oceanic oxygen minimum zone, *Opt. Express*, *17*(24), 21,992–22,004, doi:10.1117/12.190060.

Wong, A. P. S., G. C. Johnson, and W. B. Owens (2003), Delayed-mode calibration of autonomous CTD profiling float salinity data by θ – S climatology, *J. Atmos. Oceanic Technol.*, *20*(2), 308–318, doi:10.1175/1520-0426(2003)020<0308:DMCOAC>2.0.CO;2.

York, D. (1966), Least-squares fitting of a straight line, *Can. J. Phys.*, *44*, 1079–1086.

Acknowledgements

Chapter 2, in full, is a reprint of previously published material in Journal of Geophysical Research: Oceans, 2013. Takeshita, Y., Martz, T.R., Johnson, K.S., Plant, J.N., Gilbert, D., Riser, S.C., Neill, C., and Tilbrook, B. The dissertation author was the primary investigator and author of this paper.

CHAPTER 3: CHARACTERIZATION OF AN ION SENSITIVE FIELD EFFECT TRANSISTOR AND CHLORIDE ION SELECTIVE ELECTRODES FOR PH MEASUREMENTS IN SEAWATER

Abstract

Characterization of several potentiometric cells without liquid junction has been carried out in universal buffer, aqueous HCl, and artificial seawater media. The electrodes studied include Ion Sensitive Field Effect Transistor (ISFET) pH electrodes, and Chloride-Ion Selective Electrodes (Cl-ISE) directly exposed to the solution. These electrodes were compared directly to the conventional Standard Hydrogen Electrode and Silver-Silver Chloride electrode in order to report the degree to which they obey ideal Nernstian laws. These data provide a foundation for operating the ISFET/Cl-ISE pair in seawater as a pH sensor. In order to obtain the highest quality pH measurements from this sensor, its response to changes in pH and salinity must be properly characterized. Our results indicate near-ideal Nernstian response for both electrodes over a wide range of H^+ and Cl^- activity. We conclude that the combined error due to sub-Nernstian response of the cell ISFET|seawater|Cl-ISE over the range of seawater pH and salinity is negligible (<0.0001 pH). The cross sensitivity of the Cl-ISE to Br^- does not seem to be a significant source of error (<0.003 pH) in seawater media between salinity of 20 – 35.

Introduction

A variety of biogeochemical processes in the ocean result in changes to the oceanic CO_2 system. Such processes include production/respiration, calcification/dissolution, and air-sea gas exchange of CO_2, and can be quantified in terms of the observed magnitudes of these changes [*Smith and Key*, 1975; *Lee*, 2001; *Feely et al.*, 2002; *Takahashi et al.*, 2009]. As the CO_2 system is the dominant acid-base system in seawater, these various processes necessarily change the pH; though knowledge of pH alone is not sufficient to describe unambiguously the changes that occur [*Dickson*, 2010]. Nevertheless, advances in pH measurement methodology [*Clayton and Byrne*, 1993; *Martz et al.*, 2010; *Carter et al.*, 2013] and calibration protocols [*Millero et al.*, 1993; *DelValls and Dickson*, 1998; *Liu et al.*, 2011; *Easley and Byrne*, 2012] have made pH an effective tool for monitoring the ocean. Observations from autonomous sensors are especially powerful, as they are capable of providing measurements at time and space scales that are not possible using classic sampling schemes [*Johnson et al.*, 2007; *Prien*, 2007; *Moore et al.*, 2009; *Roemmich et al.*, 2009]. Use of such autonomous sensor data for quantitative biogeochemical studies is becoming more common [*Emerson et al.*, 2008; *Emerson and Stump*, 2010; *Harris et al.*, 2013; *Martz et al.*, 2014].

pH sensors based on the Honeywell Durafet Ion Sensitive Field Effect Transistor (ISFET) technology have shown extraordinary stability in seawater, [*Martz et al.*, 2010] and have recently seen a dramatic increase in use worldwide [*Hofmann et al.*, 2011, 2014; *Kroeker et al.*, 2011; *Matson et al.*, 2011; *Frieder et al.*, 2012; *Price*

et al., 2012; *Bresnahan et al.*, 2014; *Kapsenberg and Hofmann*, 2014; *Martz et al.*, 2014]. The ISFET is an active electronic circuit in which the potential between the reference electrode and the source of the MOSFET transistor can be made to follow the Nernst equation if the amphoteric material on the gate insulator has sufficient buffer capacity [*Bergveld*, 2003a]; insufficient buffer capacity of the gate insulator material leads to sub-Nernstian response of the sensor. For example, ISFETs that utilize Ta_2O_5 for the insulator have near-Nernstian response to pH, whereas the sensitivity reduces to 30 mV pH^{-1} when using SiO_2 [*Bergveld*, 2003b]. The gate material of the Durafet is Honeywell proprietary information.

Although ISFET pH sensors have been evaluated extensively for their stability [*Martz et al.*, 2010], a thorough characterization of the Nernst response of ISFETs over the seawater range of pH and ionic composition has not been carried out with the low uncertainty desired by chemical oceanographers. For example, near-Nernstian response of ISFETs has been documented using NBS buffer solutions [*Connery et al.*, 1992; *Sandifer and Voycheck*, 1999; *Bergveld*, 2003b] and buffers in artificial seawater media [*Martz et al.*, 2010]. However, the uncertainty of the response estimated in this fashion is too large to enable a meaningful correction to be made for oceanic biogeochemical studies. In addition, potential cation interferences to the ISFET pH sensor and optimization of the reference electrodes used with the ISFET have not been thoroughly examined for seawater applications. Here we demonstrate an alternate technique to constrain the Nernst slope to within ±0.1%, and show that any cation interference is negligible in seawater media, thus making possible

oceanographic applications that desire the ability to measure changes in pH to better than 0.005 pH units..

The most common reference electrode in use today consists of a silver-silver chloride (Ag/AgCl) electrode in a concentrated KCl gel saturated with AgCl and with a diffusion liquid junction to the test solution. The liquid junction potential associated with this junction is essentially uncharacterizable and is often irreproducible, leading to systematic errors [*Bates*, 1973]. Alternatively, a chloride-ion selective electrode (Cl-ISE) directly exposed to seawater has been successfully applied as an effective substitute to the conventional reference electrode with junction for ISFET pH sensors [*Shitashima et al.*, 2002; *Martz et al.*, 2010]. The use of a Cl-ISE as a reference electrode eliminates the liquid junction from the electrochemical cell and allows the sensor response to be defined in terms of the ion activity product, $a_H a_{Cl}$, a well-defined thermodynamic quantity. This allows for a potentially more robust calibration and accurate measurement of pH. This approach takes advantage of the essentially constant ionic composition of seawater [*Johnson et al.*, 1992] to calculate the concentration of chloride ion with high accuracy from the measured conductivity of the seawater, and therefore infer its effect on the cell potential. In the open ocean, salinity varies between 32 and 36 while estuarine environments can reach a salinity of near zero. It is therefore essential also to characterize the degree to which the Cl-ISE obeys an ideal Nernstian response if it is to be used as a reference electrode in an environment with variable salinity. It is also necessary to consider the sensitivity of the Cl-ISE to bromide ion in seawater, which could lead to non-Nernstian behavior.

Even if a particular ISFET sensor can be shown to be stable in seawater for long periods, any deviation from the theoretical response of the sensor to the combined effects of analyte ions and temperature results in sensor errors unless adequate protocols are outlined to account for such non-ideal behavior. To use ISFET devices to obtain the highest quality pH measurements, it is important to characterize the behavior of the ISFET and its reference electrode. Here, we present a series of experiments that quantify the Nernstian behavior of the ISFET chip used in the Honeywell Durafet line of pH sensors and of commercially-available Cl-ISEs. The Nernstian response of the ISFET to hydrogen ion was assessed by comparing its response to that of a Standard Hydrogen Electrode (SHE) over a pH range of 2 – 12 in a universal buffer solution in either a sodium or potassium chloride background. The Nernstian behavior of the Cl-ISE was assessed by means of a series of NaCl additions to an aqueous HCl solution and comparing its response to that of a standard thermal electrolytic Ag/AgCl electrode placed in the same solution without liquid junction, and by using the Pitzer model [*Pitzer*, 1973; *Pitzer and Kim*, 1974] to allow for the changing activity coefficients when interpreting the results. Finally, the overall behavior of the cell ISFET|Cl-ISE was assessed in seawater media to evaluate the effects of bromide on the electrode response of the Cl-ISE.

Experimental Section

Solution Preparation. Universal Buffer (UB) was prepared using a modified recipe described by *Ellis*, 1961 The UB contains 0.1 M of each of the following buffers in a 0.7 M ionic background of either KCl or NaCl: Tris (2-amino-2-hydroxymethyl-

propane-1,3-diol); sodium dihydrogen phosphate; citric acid (2-hydroxypropane-1,2,3-tricarboxylic acid); and sodium borate. The Na_2CO_3 in the original recipe was replaced with borate buffer because continuous bubbling of H_2 at lower pHs quantitatively removes the carbonate buffer as CO_2. 10 L stock solutions of UB were prepared.

HCl was prepared gravimetrically from a certified 1 M solution (Fisher SA48-1), and >99.998% pure NaCl was used for the additions (Acros, 31434-1KG-R, Lot SZBD0240VN; dried for >24 hours at 180 °C prior to the experiment).

Tris buffer was prepared following a standard recipe (nominal salinity = 35) [*DelValls and Dickson*, 1998]. The salts were analytical grade, and were used without further purification. A certified 1 M HCl solution (Fisher SA48-1, Lot 100167), and analytical grade Tris (Fisher T395-1, Lot 100167) were used without further purification. KBr was added to the Tris buffer to give $[Br^-]$ = 840 µmol kg^{-1}. The Tris buffer used in this study was not calibrated using a Harned cell, as done previously, [*DelValls and Dickson*, 1998] however, spectrophotometric pH measurements of the Tris buffer using purified meta-cresol purple [*Liu et al.*, 2011] were used to verify agreement with expected pH values [*DelValls and Dickson*, 1998] to 0.008 .

Experimental Apparatus. All experiments were performed in a 1 L jacketed beaker at 20.000 ± 0.002 °C. A custom lid with an o-ring seal was used to minimize evaporation, and to secure the electrodes and titrant and H_2 delivery tubes (Figure 3.1). A custom set of electronics was used in all experiments to provide a regulated power supply to the ISFET sensor, and to buffer the output of the potentiometric voltage before recording using a 24-bit ADC.

ISFET response to hydrogen ions. The voltage of the cell

ISFET | UB, HCl, NaOH | SHE (I)

(where SHE is a standard hydrogen electrode) was measured while titrating the UB with NaOH (2.5 M) over the pH range 2 – 12. Titration of UB with strong base/acid results in an approximately linear relationship between added titrant volume and pH, allowing stable observations over a wide range of pH. In comparison to measurements in certified buffer solutions, this titration technique provides a vastly superior way to assess the Nernstian behavior of a pH electrode because it provides ~200 individual measurements compared to the usual 3 – 5, and does not require transfer between different solutions. However, due to the inconvenience of operating the SHE, this technique is rarely employed. The SHE is considered to have a perfect Nernstian response [*Bates*, 1973], thus any systematic changes in the potential of cell (I) indicate a non-ideal Nernstian behavior of the ISFET, provided that the SHE is carefully prepared, and operated following a strict protocol. Each titration utilized a pair of SHEs to confirm proper electrode behavior. The percent theoretical slope (PTS), a value that indicates how closely an electrode conforms to ideal Nernstian behavior, was calculated as

$$\mathrm{PTS_{ISFET}} = \frac{(\mathrm{S} - \mathrm{b})}{\mathrm{S}} \times 100 \qquad (3.1)$$

where b is the slope of E(ISFET|SHE) versus pH [V pH^{-1}], and S is the Nernst slope $(RT\ln 10)/F$, where R is the universal gas constant (8.3145 J K^{-1} mol^{-1}), T is the temperature in Kelvin, and F is the Faraday constant (96,485 C mol^{-1}); least squares

regression was used to calculate b. The pH of the solution was estimated using the internal reference electrode of the Durafet, which is a Ag/AgCl wire submerged in a 3.5 M KCl gel solution saturated with AgCl. Systematic errors in estimating the solution pH (e.g. a sub-Nernstian response) will contribute to an uncertainty in estimating b, and hence PTS_{ISFET}. However, since b is small (<0.01) and the cell used to estimate pH has a near-Nernstian response, this additional uncertainty can be neglected.

The pH of the UB was lowered to ~2 by adding 10 mL of 1 M HCl into 500 mL of UB, then H_2 was bubbled through the solution for several hours to ensure saturation prior to the titration. Ultra High Purity H_2 (99.999%) was used, and O_2 was further removed from the gas stream using an O_2 scrubber (Agilent OT-4-SS). O_2 was removed from the titrant by bubbling with N_2 for >24 hours, followed by storage of the titrant under a nitrogen atmosphere throughout the titration. Titrant delivery was automated using either a syringe pump (Kloehn V6 48K) or a microfluidic gear pump (MilliGAT MG-1). 100 µL of titrant was added at each step, and the solution mixed for 30 seconds using a magnetic stirrer before measuring the EMF; ten voltage measurements were made after each titrant addition. Two hundred additions were made over a period of 10 hours. Barometric pressure was monitored with a resolution of 1 mbar throughout the titration (Mensor DPG2400), and the EMF of the cell was corrected to 1atm of H_2 [*Bates*, 1973].

Cl-ISE response to chloride ions. The EMF was measured on two cells without a liquid junction immersed in the same solution:

ISFET | 0.01m HCl, NaCl | Cl-ISE (II)

Cl-ISE | 0.01m HCl, NaCl | Ag|AgCl (III)

while adding NaCl(s) so as to change the concentration of NaCl in the solution from 0 to ~1 M, the upper rating for the Cl-ISE. The silver-silver chloride electrode (Ag/AgCl) was prepared using the standard thermal/electrolytic protocol [*Bates*, 1973]. The Cl-ISEs were obtained commercially (see below). Voltages were recorded every minute for >15 minutes after each addition of NaCl(s), and the last 5 measurements were averaged. The molality of hydrogen ion, m_H, remains constant throughout this experiment, thus the observed changes in EMF can be viewed as largely reflecting the response of the Cl-ISE to the changing m_{Cl}, with small yet significant changes occurring due to changing activity coefficients as the solution composition changes. The EMF of cell (II) follows the Nernst relation:

$$E = E_{ref} - S\log(\gamma_H \gamma_{Cl} m_H m_{Cl}) \quad (3.2)$$

where E_{ref} is the reference potential for cell (II) (analogous to a standard potential, E°), and γ and m are the activity coefficient and molality of the respective ions. We refrain from using the conventional symbol (E°) in equation (3.2) to denote the "standard potential" for the cell because of the significant variability in E_{ref} among ISFET pH sensors and Cl-ISEs [*Martz et al.*, 2010]. Unfortunately, this variability necessitates that E_{ref} must be determined for each individual cell; but once established, E_{ref} seems stable for months to years.

The mean ion activity coefficient of HCl ($\gamma_{\pm HCl}$) is related to the single ion activity coefficients: $\gamma_{\pm HCl} = (\gamma_H \gamma_{Cl})^{1/2}$, and has been thoroughly characterized in HCl-NaCl mixtures [*Harned and Brumbaugh*, 1922; *Harned and Mannweiler*, 1935]. A framework of equations based on the Pitzer model [*Pitzer*, 1973] was used to estimate $\gamma_{\pm HCl}$ in the HCl-NaCl mixture at 20 °C. The parameters used are given in Table 1. The output of the model was used to estimate a_{HCl} after each addition.

The Nernst response was assessed using Cl-ISEs from two different manufacturers: 5 Thermo-Scientific Orion 9417BN ISEs, and 2 based on silver-silver chloride pellets purchased from Van London and sealed into a cavity machined on the end of a PEEK rod in house; the experiment was also repeated in triplicate on a single Orion electrode. Two approaches were employed. The first approach is similar to the experiment outlined in the previous section, where trends in the E(Cl-ISE|Ag/AgCl) are assessed over a wide range of chloride concentrations. The Ag/AgCl electrodes are considered to behave ideally [*Baucke*, 2002], thus any systematic changes observed in E(Cl-ISE|Ag/AgCl) as the solution composition changes indicate non-Nernstian behavior of the Cl-ISE. The $PTS_{Cl\text{-}ISE|Ag/AgCl}$ is calculated using an expression similar to equation (3.1), where now b is the slope of E(Cl-ISE|Ag/AgCl) versus $-\log(a_{HCl})$ [V $-\log(a_{HCl})^{-1}$]. Any likely uncertainty in the calculated value of a_{HCl} will only have a minor effect on $PTS_{Cl\text{-}ISE|Ag/AgCl}$.

The second approach uses a_{HCl} estimated using the Pitzer model to calculate the expected changes in the EMF of cell (II) resulting from the NaCl additions, and compares them to those observed. The $\gamma_{\pm HCl}$ calculated from the Pitzer model was

combined with the gravimetrically determined molality of the ions to predict changes in EMF (Equation (3.2)). Ideally, the slope of EMF versus $-\log(a_{HCl})$ should equal S, the Nernst value (at 20 °C). As PTS_{ISFET} is already known, it is possible to estimate $PTS_{Cl\text{-}ISE}$ ($= S_{observed}/(S\ PTS_{ISFET})$). Any uncertainty in estimating $-\log(a_{HCl})$ is directly translated to the calculated PTS for this method.

Overall response of the cell ISFET|Cl-ISE in seawater media. Equimolar tris buffer prepared in artificial seawater (referred to as Tris buffer hereafter) is the pH standard for oceanographic pH measurements [*Dickson*, 1993; *Millero et al.*, 1993; *DelValls and Dickson*, 1998]. The pH of Tris buffer has been characterized (expressed in terms of the total hydrogen ion concentration) over a range of temperature and salinity (0 – 45 °C and 20 – 40, respectively) [*DelValls and Dickson*, 1998]; the total hydrogen ion concentration is defined as $m_H^* = m_H(1 + S_T/K_{HSO4})$, where S_T is the total sulfate concentration ($m_{HSO4} + m_{SO4}$) and K_{HSO4} is the conditional dissociation constant of bisulfate in seawater. This makes Tris buffer a suitable solution to test the overall response of the cell ISFET|Cl-ISE and to assess the sensitivity of the Cl-ISE to bromide in seawater media. KBr was added to Tris buffer that was prepared in house (see above for details) to give $[Br^-]$ = 840 μmol kg^{-1}, the concentration of bromide in seawater of salinity 35. The assumption was made that the presence of bromide in Tris buffer has a negligible effect on the pH of the solution.

The EMF was measured on the cell:

ISFET | Tris Buffer + KBr |Cl-ISE (IV)

and the buffer solution was diluted from salinity 35 to 20 through a series of dilutions at ~1 salinity increments. The pH of Tris buffer on the total scale (pH_T), as measured with cell (IV), can be calculated by:

$$pH_T = -\log(m_H^*) = \frac{(E - E_{ref}^*)}{S} + \log(m_{Cl}) \quad (3.3)$$

$$E_{ref}^* = E_{ref} - Slog(\gamma_{\pm HCl}^{tr}) + Slog(1 + \frac{S_T}{K_{HSO4}}) \quad (3.4)$$

where E_{ref}^* represents the reference potential corresponding to the total hydrogen ion concentration scale, and $\gamma_{\pm HCl}^{tr}$ indicates the trace value of $\gamma_{\pm HCl}$ [*Dickson*, 1990]; information from *Dickson*, 1990 was used to quantify the latter two terms on the right hand side of equation (3.4), and E_{ref} was determined at the beginning of every experiment based on EMF measurements of cell (IV) in Tris buffer with salinity of 35. For each dilution step, pH_{resid} was calculated, where $pH_{resid} = pH_{ISFET|Cl\text{-}ISE} - pH_S$; pH_S is the value of the certified buffer pH standard, calculated using equation 17 and18 in *DelValls and Dickson*, 1998. Since the pH remains largely constant throughout the dilutions (change in pH <0.03), whereas m_{Cl} and m_{Br} change by almost a factor of 2, the pH_{resid} can be interpreted as a measure of how well the cell ISEFET|Cl-ISE performs in seawater media, especially in the presence of bromide. Because the ISFET|Cl-ISE measurement was first standardized to pH_S, pH_{resid} does not include any small uncertainty in the value of pH_S due to the original solution preparation of the buffer solution.

The dilutions were carried out for a subset of Cl-ISEs from the previous experiment (Table 3.4), using a single Durafet (Table 3.2). A shift in potential occurs when a Cl-ISE is first exposed to a solution containing Br^- due to the exchange of Cl^- and Br^- in the solid solution [*Vaslow and Boyd*, 1952]. The electrodes were therefore conditioned in Tris buffer containing Br^- for over 2 weeks prior to this experiment.

Results and Discussion

Nernstian Response of the ISFET to Hydrogen Ion Activity. The three Durafets showed repeatable, Nernstian response to changes in pH between pH 2 – 12 (Table 3.2). These results are consistent with previous studies that have assessed the Nernstian behavior of Durafet electrodes [*Connery et al.*, 1992; *Sandifer and Voycheck*, 1999]. One of the ISFETs (DF3) was created from a different production wafer than the other two, suggesting consistency across independently manufactured Honeywell ISFET chips; *Sandifer and Voycheck*, 1999 also reported near-Nernstian behavior of ISFETS from four different production wafers.

Although the entire range of E(ISFET|SHE) was less than 100 µV over 10 pH units, a systematic pattern of slightly sub-Nernstian response under acidic conditions (pH 2 – 7.5), and super-Nernstian response under basic conditions (pH 7.5 – 12) was observed in all cases (Figure 3.2). A possible explanation to this behavior is a small cross sensitivity of the ISFET to cations in solution (e.g. a sodium error; the buffers used to prepare the UB were sodium salts). The commonly observed sodium error in glass electrodes becomes apparent at higher pH, as $[H^+]$ reaches trace amounts. The same pattern was observed between solutions with a 0.7 M NaCl or KCl ionic

background (Table 3.2), suggesting that sodium is not the sole source of the super-Nernstian response at high pH. However, since the buffers were made from sodium salts, the experiment was not carried out in a completely Na-free solution, even in the KCl background. It is important to note that although these non-ideal behaviors are statistically significant, they can be safely ignored. For example, in the pH range 7 – 8.5, the largest non-Nernstian behavior observed in this study would result in a calculated pH bias of < 0.00005; significantly smaller than the precision of the electrode. However, since the PTS of ISFETs depend on the insulating material [*Bergveld*, 2003b], results presented here would not be representative of all ISFET devices.

In this study, the PTS can be quantified with low uncertainty for two reasons. First, direct comparison of the ISFET to the SHE potential eliminates any need to rely on standard buffer solutions. Since all pH measurements are ultimately traced back to measurements using a SHE in a Harned cell [*Bates*, 1973], direct measurements of E(ISFET|SHE) over a large range of pH provides unambiguous assessment of the Nernstian response of the ISFET to hydrogen ion. Second, stable EMF measurements can be made throughout the titration due to the buffering capacity of the UB over a wide range of pH. The stability of E(ISFET|SHE) at any point during this experiment was around 20 – 30 μV (1 std. dev.). The number of separate data points utilized in the regression leads to a robust determination of the PTS.

As a comparison, we estimate the likely error for the PTS that would result from using the "multipoint calibration" approach [*Baucke et al.*, 1993; *Buck et al.*,

2002], recommended by IUPAC for the highest quality pH measurements. The estimate (Table 3.3) is based on using 4 buffers (pH = 4.1, 6.9, 9.21, and 10.01) and standard propagation of uncertainty calculations [*EURACHEM/CITAC*, 2000]. Three sources of error were assumed: errors in the pH assigned to the buffer, in the temperature used to calculate the Nernst slope, and in the voltage measurements. The effect of temperature was small (<0.01% in PTS for an uncertainty of 0.1°C), thus is not considered further. The dominant source of error in the calculated PTS is the uncertatinty of the buffer pH, with a smaller yet noticeable influence from the uncertainty of the voltage measurements. Even in the best case scenario (pH uncertainty of 0.005 and voltage uncertainty of 20 μV), the calculated uncertainty in the PTS is larger than the values reported in this study by an order of magnitude. Such an error would be noticeable using a state of the art combination glass electrode with a resolution of 0.001 if pH measurements were made over a range > 1. However, the method used here is significantly more complex to perform, and for many applications the multipoint calibration may suffice. But such an approach will necessarily require a liquid junction as conventional buffers do not have chloride ion, and the main source of error may then be the residual liquid junction potential.

Response of Cl-ISE to Chloride ion activity: All 7 Cl-ISEs conformed closely to ideal Nernstian behavior over a large range of chloride concentration (Table 3.4). Typical results from NaCl additions are shown in Figure 3.3. The $PTS_{Cl\text{-}ISE|Ag/AgCl}$ is likely to provide the more accurate assessment of electrode response, because the Cl-ISE is measured directly against the Ag/AgCl electrode and the result is relatively

insensitive to small errors in the calculated a_{HCl}. The results from a triplicate run were in agreement within experimental error (Table 3.4, electrode O2). Overall, $PTS_{Cl\text{-}ISE\_Pitz}$ was lower than $PTS_{Cl\text{-}SE|Ag/AgCl}$ by 0.56 ± 0.14% (1 std. dev.), suggesting a small negative bias when determining PTS by directly estimating a_{HCl} using the Pitzer model. Nevertheless, this suggests that the PTS of Cl-ISE can be accurately constrained to several tenths of a percent even without using a Ag/AgCl electrode.

It is known that the silver-silver chloride electrode in acidic solution exhibits a slightly different absolute voltage in the presence of O_2 [*Taylor and Smith*, 1939; *Bates*, 1973]. However, there is little evidence that the response to chloride ion suffers in the presence of air and therefore our experiment was performed without deoxygenating the solution so as to avoid additional experimental complications. For example, each addition of $NaCl_{(s)}$ exposes the experiment to the atmosphere and thus would require continuous bubbling of the solution with an inert gas such as N_2. This could cause the solution to splash onto the side of the beaker and possibly evaporate, making it difficult to accurately quantify the $m_{Cl}$with each $NaCl_{(s)}$ addition. Since the quality of the calculated PTS is directly dependent on the accuracy of m_{Cl}, the experiment was carried out in a way that minimized evaporation, but allowed for contact with the atmosphere. The disturbance in the potential of silver-silver chloride electrode due to oxygen is attributed to the following reaction [*Taylor and Smith*, 1939]

$$2Ag + 2HCl + {}^{1}/_{2}\,O_2 \rightarrow 2AgCl + H_2O \qquad (3.5)$$

which results in a slightly reduced concentration of HCl within the porous electrode. The effect of this side reaction on the electrode potential was quantified by:

$$E = E^{o} - \frac{RT}{F}\ln(C - \delta) \quad (3.6)$$

where C is the concentration of HCl, and δ is the effective decrease in C within the silver-silver chloride electrode. The δ was found to be δ ≈ C/200, however, it was only estimated at 0.05 m HCl [*Taylor and Smith*, 1939]. If δ is proportional to C throughout the whole [Cl^-] range, it would not have any effect on the calculated PTS, since all points in Figure 3.3 will be subject to the same offset, leaving the calculated slope unaffected.

The error associated with the observed non-Nernstian response of the Cl-ISE is negligible when measuring seawater pH. For the salinity range of the open ocean (32 - 36), even a 98% PTS (worse than any electrode observed in this study) only leads to an uncertainty of < 0.0001 pH. This increases to ~0.0003 when the lower limit of the range is extended to a salinity of 20. Considering that the short term pH precision of the cell ISFET|Cl-ISE is about 0.0005, errors associated with non-Nernstian response of Cl-ISE can safely be ignored.

Overall Response in Seawater Media. The $|pH_{resid}|$ was <0.002 for three of the four electrodes, and <0.003 for all four electrodes between salinity 20 – 35, showing excellent agreement between the measured and calculated Tris buffer pH (Figure 3.4). The effect on pH of diluting the buffer concentration was neglected as this effect is small [*DelValls and Dickson*, 1998]. These results suggest that the presence of Br^-

does not appear to significantly affect the electrochemical cell performance, so long as the Cl-ISE has been conditioned in a solution containing seawater levels of bromide ion. Furthermore, electrodes from both manufacturers (Orion and Van London) seem to perform equally well, despite the difference in impedance observed between the two types of electrodes. We suspect this difference reflects differing compositions of the Cl-ISE, however, cannot confirm such suspicions because this information is proprietary. Only a small number of electrodes were tested here, and further validation of these results using a greater number of electrodes may be warranted.

Conclusion

The Nernstian response of the ISFET to hydrogen ion and Cl-ISE to chloride ion have been examined over a wide range of pH and chloride ion concentration. Direct comparison to the standard hydrogen electrode over a pH range of 2 – 12 in a constant ionic background revealed a near-ideal response of the ISFET to hydrogen ion. The Cl-ISE showed a slightly sub-Nernstian response, but all electrodes tested here had a PTS >99.4%. The error that can be expected from the observed non-Nernstian behavior over the seawater range of pH (7 – 8.5) and salinity (32 – 35) is negligible (<0.0001 pH). Any cross sensitivity to bromide in seawater media does not seem to introduce significant errors into the measured pH for salinities between 20 and 35. It is important to note that the results presented here refer to the errors associated with changing pH and salinity, and do not reflect the combined uncertainty of pH measurements which would also include any associated calibration uncertainty. The latter will depend – in part – on the uncertainty of a reference pH value, reported for a

Certified Reference Material or the pH ascribed to a traceable pH measurement carried out alongside an operating sensor [*Bresnahan et al.*, 2014]. Furthermore, uncertainties due to rapidly changing environmental conditions (e.g. thermal or salinity) can potentially introduce errors not accounted for here.

The use of ISFET|Cl-ISE pH sensors in oceanography is expected to increase in the coming years, as such a sensor adapted for oceanographic observations (based on the Durafet) has recently became commercially available (SeaFET^{TM} Ocean pH Sensor, Satlantic, Halifax, Canada). In addition to the near-ideal response to chloride ion at 1 atm, the Cl-ISE appears to exhibit minimal pressure hysteresis [*Shitashima et al.*, 2002], making it an attractive option for profiling applications [*Shitashima et al.*, 2008]. High pressure tolerant ISFET sensors with Cl-ISE reference electrodes are now being deployed on profiling floats of the type used in the Argo array [*Johnson et al.*, 2007; *Roemmich et al.*, 2009]. These platforms enable pH observations to be made throughout the open ocean and the work performed here demonstrates that the sensor response to hydrogen ion and chloride concentrations matches the theoretical predictions. This is an essential, enabling step for the development of a global pH observing system. As the number of ISFET|Cl-ISE sensors increases, it will be essential to establish standard calibration protocols, ideally implemented by the manufacturer, to ensure data comparability from these sensors. This work demonstrates that protocols to correct for non-Nernstian behavior are not necessary, allowing for a more simplified calibration procedure and thus a higher rate of sensor production at less, potentially making it more accessible for the community.

Acknowledgements

We would like to thank Hans Jannasch, Makaila LaShomb, and Britain Richardson for their help with buffer and electrode preparation. This work was supported by the National Oceanographic Partnership Program award N00014-10-1-0206.

Chapter 3, in full, is currently being prepared for submission for publication of the material. Takeshita, Y., Martz, T.R., Johnson, K.S., and Dickson, A.G. The dissertation author was the primary investigator and author of this paper.

Table 3.1: Pitzer model parameters used to estimate $\gamma_{\pm HCl}$ for HCl-NaCl mixture at 20 °C.

Parameter	Value (20 °C)	Reference
$\mathbf{A_{\varphi}}$	0.3882 $kg^{1/2}$ $mol^{-1/2}$	[*Bradley and Pitzer*, 1979]
$\boldsymbol{\beta_{HCl}^{(0)}}$	0.1788	[*Holmes et al.*, 1987]
$\boldsymbol{\beta_{HCl}^{(1)}}$	0.2956	[*Holmes et al.*, 1987]
$\boldsymbol{\beta_{NaCl}^{(0)}}$	0.0714	[*Pitzer et al.*, 1984]
$\boldsymbol{\beta_{NaCl}^{(1)}}$	0.2723	[*Pitzer et al.*, 1984]
$\boldsymbol{C_{HCl}^{\varphi}}$	5.138×10^{-4}	[*Holmes et al.*, 1987]
$\boldsymbol{C_{NaCl}^{\varphi}}$	0.002	[*Pitzer et al.*, 1984]
$\boldsymbol{\theta_{HNa}}$	0.036	[*Pitzer and Kim*, 1974]
$\boldsymbol{\theta_{HNa}'}$	0	[*Pitzer and Kim*, 1974]
$\boldsymbol{\psi_{HNaCl}}$	-0.004	[*Pitzer and Kim*, 1974]
$\boldsymbol{\alpha}$	2 $kg^{1/2}$ $mol^{-1/2}$	[*Pitzer*, 1973]

Table 3.2: Average PTS ± 95% C.I. (n = 6 for each electrode, t = 2.571) of three Durafet sensors

Durafet #ID	pH 2-7.5	pH 7.5-12	pH 2-12
DF1[a]	99.985 ± 0.004%	100.029 ± 0.004%	100.005 ± 0.002%
DF2[b]	99.976 ± 0.011%	100.032 ± 0.013%	100.007 ± 0.002%
DF3[b,c]	99.996 ± 0.005%	100.036 ± 0.009%	100.019 ± 0.008%

[a] Ionic background of KCl
[b] Ionic background of NaCl
[c] Electrode used in Tris buffer dilution experiments.

Table 3.3: Estimated uncertainty of calculated PTS from multipoint calibration using 4 buffers

EMF uncertainty (right) pH uncertainty (down)	20 µV	100 µV	200 µV	300 µV	500 µV
0.005	0.12%	0.15%	0.21%	0.30%	0.47%
0.010	0.22%	0.24%	0.29%	0.35%	0.50%
0.015	0.33%	0.34%	0.38%	0.43%	0.56%
0.020	0.44%	0.45%	0.47%	0.52%	0.63%

Table 3.4: PTS (± 95% C.I.) for Cl-ISE and Ag/AgCl reference electrodes

	PTS_{ISE_Pitz}[a]	$PTS_{Cl\text{-}ISE\|Ag/AgCl}$
O2[b]	99.16 ± 0.18	99.46 ± 0.05
O2[b]	98.83 ± 0.18	99.41 ± 0.08
O2[b]	98.85 ± 0.19	99.43 ± 0.07
O3[b]	99.43 ± 0.41	100.03 ± 0.09
O4	99.24 ± 0.42	99.72 ± 0.42
O5	99.20 ± 0.22	99.98 ± 0.09
O6	99.21 ± 0.19	99.80 ± 0.05
VL1[b]	99.39 ± 0.16	——
VL2[b]	99.54 ± 0.16	——

[a] $R^2 > 0.9999$ for linear regression

[b] Electrodes used in Tris buffer dilution experiments.

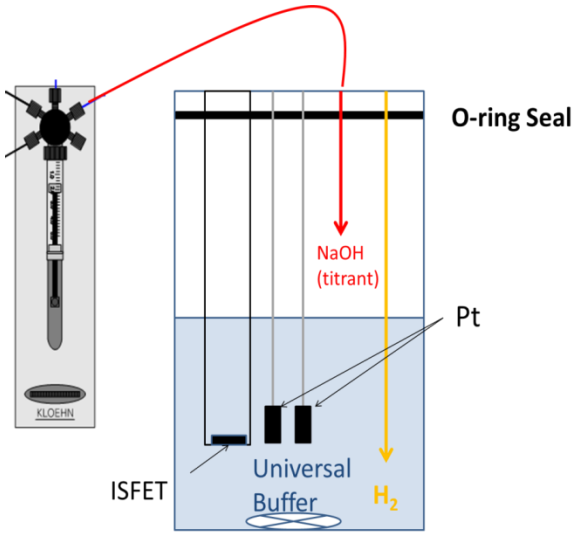

Figure 3.1: Schematic of the custom hydrogen electrode cell. The cell is constructed of a 1 L jacketed beaker for temperature control and a custom o-ring sealed cap for H_2 and titrant delivery. The same apparatus was used for the other experiments with the ports for H_2 and NaOH plugged.

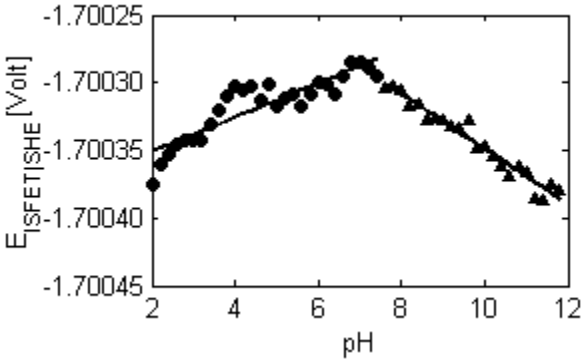

Figure 3.2: Average titration results for Durafet #2 (n = 6). A positive and negative slope indicates a sub and super Nernstian response, respectively. Circles and triangles indicate data for pH <7.5 and >7.5, respectively. Solid lines represent the regression used to calculate PTS_{ISFET}.

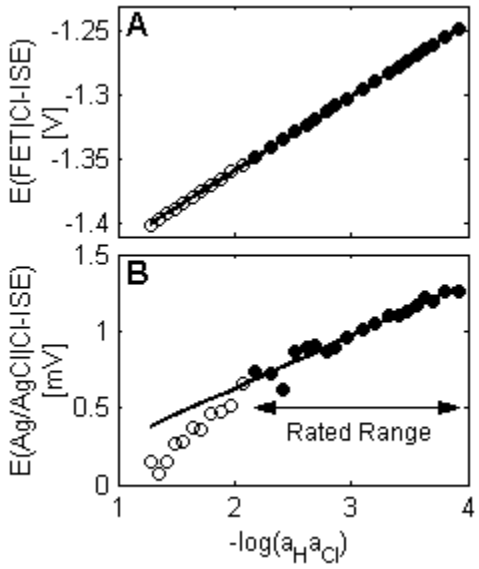

Figure 3.3: Results from a typical experiment showing (A) E(ISFET|Cl-ISE) (data for the Ag/AgCl electrode not shown), and (B) E(Ag/AgCl|Cl-ISE). Solid lines represent the linear regression used to calculate the PTS. Open symbols represent data where $[Cl^-] > 1M$, and were not used in calculating PTS.

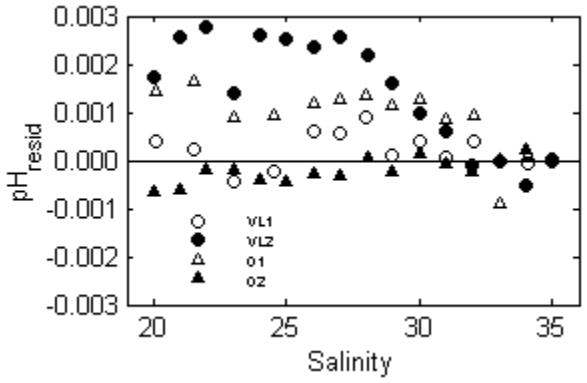

Figure 3.4: Effect of salinity on pH_{resid}. One anomalous data point was deleted.

References

Bates, R. G. (1973), *Determination of pH Theory and Practice*, 2nd ed., John Wiley & Sons, Inc., New York.

Baucke, F. G. K. (2002), New IUPAC (International Union of Pure and Applied Chemistry) recommendations on the measurement of pH - background and essentials., *Anal. Bioanal. Chem.*, *374*(5), 772–7, doi:10.1007/s00216-002-1523-4.

Baucke, F. G. K., R. Naumann, and C. A. Weber (1993), Multiple-Point Calibration with Linear Regression as a Proposed Standardization Procedure for High-Precision pH Measurements, *Anal. Chem.*, *65*(22), 3244–3251.

Bergveld, P. (2003a), ISFET , Theory and Practice, in *IEEE Sensor Conference*, pp. 1–26, Toronto.

Bergveld, P. (2003b), Thirty years of ISFETOLOGY What happened in the past 30 years and what may happen in the next 30 years, *Sensors Actuators B Chem.*, *88*(1), 1–20.

Bradley, D. J., and K. S. Pitzer (1979), Thermodynamics of electrolytes. 12. Dielectric properties of water and Debye-Hueckel parameters to 350.degree.C and 1 kbar, *J. Phys. Chem.*, *83*(12), 1599–1603, doi:10.1021/j100475a009.

Bresnahan, P. J., T. R. Martz, Y. Takeshita, K. S. Johnson, and M. LaShomb (2014), Best practices for autonomous measurement of seawater pH with the Honeywell Durafet, *Methods Oceanogr.*, *Accepted*.

Buck, R. P. et al. (2002), Measurement of pH . Definition, Standards, and Procedures (IUPAC Recommendations 2002), *Pure Appl. Chem.*, *74*(11), 2169–2200.

Carter, B. R., J. a. Radich, H. L. Doyle, and a. G. Dickson (2013), An automated system for spectrophotometric seawater pH measurements, *Limnol. Oceanogr. Methods*, *11*, 16–27, doi:10.4319/lom.2013.11.16.

Clayton, T. D., and R. H. Byrne (1993), Spectrophotometric seawater pH measurements : total hydrogen results, *Deep Sea Res. Part I Oceanogr. Res. Pap.*, *40*(10), 2115–2129.

Connery, J. G., R. D. Baxter, and C. W. Gulczynski (1992), Development and Performance Characteristics of a New pH Electrode, in *Pittsburgh Conference*, pp. 1–4.

DelValls, T. A., and A. G. Dickson (1998), The pH of buffers based on 2-amino-2-hydroxymethyl-1,3-propanediol (“tris”) in synthetic sea water, *Deep Sea Res. Part I Oceanogr. Res. Pap.*, *45*(9), 1541–1554.

Dickson, A. G. (1990), Standard potential of the reaction : AgCl (s) + 1/2H2(g) = Ag (s) + HCl (aq), and the standard acidity constant of the ion HSO4- in synthetic sea water from 273 . 15 to 318 . 15 K, *J. Chem. Thermodyn.*, *22*(3), 113–127.

Dickson, A. G. (1993), pH buffers for sea water media based on the total hydrogen ion concentration scale, *Deep Sea Res. Part I Oceanogr. Res. Pap.*, *40*(1), 107–118, doi:10.1016/0967-0637(93)90055-8.

Dickson, A. G. (2010), The carbon dioxide system in seawater: equilibrium chemistry and measurements, in *Guide to Best Practices for Ocean Acidificaton Research and Data Reporting*, edited by U. Riebesell, V. J. Fabry, L. Hansson, and J.-P. Gattuso, pp. 17–40, EUR 24328 EN, European Commission, Brussels, Belgium.

Easley, R. A., and R. H. Byrne (2012), Spectrophotometric Calibration of pH Electrodes in Seawater Using Purified m-Cresol Purple., *Environ. Sci. Technol.*, *46*(9), 5018–24, doi:10.1021/es300491s.

Ellis, D. A. (1961), A New Universal Buffer System, *Nature*, *191*(479), 1099–1100.

Emerson, S. R., and C. Stump (2010), Net biological oxygen production in the ocean—II: Remote in situ measurements of O2 and N2 in subarctic pacific surface waters, *Deep Sea Res. Part I Oceanogr. Res. Pap.*, *57*(10), 1255–1265, doi:10.1016/j.dsr.2010.06.001.

Emerson, S. R., C. Stump, and D. Nicholson (2008), Net biological oxygen production in the ocean: Remote in situ measurements of O 2 and N 2 in surface waters, *Global Biogeochem. Cycles*, *22*(3), 1–13, doi:10.1029/2007GB003095.

EURACHEM/CITAC (2000), *Quantifying Uncertainty in Analytical Measurement*, edited by S. L. R. Ellison, M. Rosslein, and A. Williams.

Feely, R. A. et al. (2002), In situ calcium carbonate dissolution in the Pacific Ocean, *Global Biogeochem. Cycles*, *16*(4), 91–1–91–12, doi:10.1029/2002GB001866.

Frieder, C. A., S. Nam, T. R. Martz, and L. A. Levin (2012), High temporal and spatial variability of dissolved oxygen and pH in a nearshore California kelp forest, *Biogeosciences*, *9*(10), 3917–3930, doi:10.5194/bg-9-3917-2012.

Harned, H. S., and N. J. Brumbaugh (1922), The activity coefficient of hydrochloric acid in aqueous salt solutions, *J. Am. Chem. Soc.*, *44*, 2729–2748.

Harned, H. S., and G. E. Mannweiler (1935), The Thermodynamics of Ionized Water in Sodium Chloride Solutions, *J. Am. Chem. Soc.*, *57*(10), 1873–1876.

Harris, K. E., M. D. DeGrandpre, and B. Hales (2013), Aragonite saturation state dynamics in a coastal upwelling zone, *Geophys. Res. Lett.*, *40*(11), 2720–2725, doi:10.1002/grl.50460.

Hofmann, G. E. et al. (2011), High-Frequency Dynamics of Ocean pH: A Multi-Ecosystem Comparison, edited by W.-C. Chin, *PLoS One*, *6*(12), e28983, doi:10.1371/journal.pone.0028983.

Hofmann, G. E. et al. (2014), Exploring local adaptation and the ocean acidification seascape – studies in the California Current Large Marine Ecosystem, *Biogeosciences*, *11*(4), 1053–1064, doi:10.5194/bg-11-1053-2014.

Holmes, H. F., O. Ridge, and R. H. Wood (1987), The enthalpy of dilution of HCl(aq) to 648 K and 40 MPa Thermodynamic properties, *J. Chem. Thermodyn.*, *19*, 863–890.

Johnson, K. S., K. H. Coale, and H. W. Jannasch (1992), Analytical Chemistry in Oceanography, *Anal. Chem.*, *64*(22), 1065–1075.

Johnson, K. S., J. A. Needoba, S. C. Riser, and W. J. Showers (2007), Chemical sensor networks for the aquatic environment., *Chem. Rev.*, *107*(2), 623–40, doi:10.1021/cr050354e.

Kapsenberg, L., and G. E. Hofmann (2014), Signals of resilience to ocean change: high thermal tolerance of early stage Antarctic sea urchins (Sterechinus neumayeri) reared under present-day and future pCO2 and temperature, *Polar Biol.*, doi:10.1007/s00300-014-1494-x.

Kroeker, K. J., F. Micheli, M. C. Gambi, and T. R. Martz (2011), Divergent ecosystem responses within a benthic marine community to ocean acidification., *Proc. Natl. Acad. Sci. U. S. A.*, *108*(35), 14515–20, doi:10.1073/pnas.1107789108.

Lee, K. (2001), Global net community production estimated from the annual cycle of surface water total dissolved inorganic carbon, *Limnol. Oceanogr.*, *46*(6), 1287–1297, doi:10.4319/lo.2001.46.6.1287.

Liu, X., M. C. Patsavas, and R. H. Byrne (2011), Purification and characterization of meta-cresol purple for spectrophotometric seawater pH measurements., *Environ. Sci. Technol.*, *45*(11), 4862–8, doi:10.1021/es200665d.

Martz, T., U. Send, M. D. Ohman, Y. Takeshita, P. Bresnahan, H.-J. Kim, and S. Nam (2014), Dynamic Variability of Biogeochemical Ratios in the Southern California Current System, *Geophys. Res. Lett.*, *41*(7), 2496–2501, doi:10.1002/2014GL059332.

Martz, T. R., J. G. Connery, and K. S. Johnson (2010), Testing the Honeywell Durafet for seawater pH applications, *Limnol. Oceanogr. Methods*, *8*, 172–184, doi:10.4319/lom.2010.8.172.

Matson, P. G., T. R. Martz, and G. E. Hofmann (2011), High-frequency observations of pH under Antarctic sea ice in the southern Ross Sea, *Antarct. Sci.*, *7*, 1–7, doi:10.1017/S0954102011000551.

Millero, F. J., J.-Z. Zhang, S. Fiol, S. Sotolongo, R. N. Roy, K. Lee, and S. Mane (1993), The use of buffers to measure the pH of seawater, *Mar. Chem.*, *44*(2-4), 143–152.

Moore, T. S., K. M. Mullaugh, R. R. Holyoke, A. S. Madison, M. Yücel, and G. W. I. Luther (2009), Marine Chemical Technology and Sensors for Marine Waters: Potentials and Limits, *Ann. Rev. Mar. Sci.*, *1*(1), 91–115, doi:10.1146/annurev.marine.010908.163817.

Pitzer, K. S. (1973), Thermodynamics of Electrolytes. I. Theoretical Basis and General Equations, *J. Phys. Chem.*, *77*(2), 268–277.

Pitzer, K. S., and J. J. Kim (1974), Thermodynamics of electrolytes. IV. Activity and osmotic coefficients for mixed electrolytes, *J. Am. Chem. Soc.*, *96*(18), 5701–5707, doi:10.1021/ja00825a004.

Pitzer, K. S., C. J. Peiper, and H. R. Busey (1984), Thermodynamic Properties of Aqueous Sodium Chloride Solutions, *J. Phys. Chem. Ref. Data*, *13*(1), 1–102, doi:10.1063/1.555709.

Price, N. N., T. R. Martz, R. E. Brainard, and J. E. Smith (2012), Diel Variability in Seawater pH Relates to Calcification and Benthic Community Structure on Coral Reefs., *PLoS One*, *7*(8), e43843, doi:10.1371/journal.pone.0043843.

Prien, R. D. (2007), The future of chemical in situ sensors, *Mar. Chem.*, *107*(3), 422–432, doi:10.1016/j.marchem.2007.01.014.

Roemmich, D., G. C. Johnson, S. C. Riser, R. E. Davis, J. Gilson, W. B. Owens, S. L. Garzoli, C. Schmid, and M. Ignaszewski (2009), The Argo Program: Observing the Global Ocean with Profiling Floats, *Oceanography*, *22*, 34–43, doi:10.5670/oceanog.2009.65.COPYRIGHT.

Sandifer, J. R., and J. J. Voycheck (1999), A Review of Biosensor and Industrial Applications of pH-ISFETs and an Evaluation of Honeywell's "DuraFET," *Microchim. Acta*, *131*(1-2), 91–98, doi:10.1007/s006040050013.

Shitashima, K., M. Kyo, Y. Koike, and H. Henmi (2002), Development of in situ pH sensor using ISFET, in *International Symposium on Underwater Technology*, pp. 106–108, IEEE, Tokyo.

Shitashima, K., Y. Maeda, Y. Koike, and T. Ohsumi (2008), Natural analogue of the rise and dissolution of liquid CO2 in the ocean, *Int. J. Greenh. Gas Control*, *2*(1), 95–104, doi:10.1016/S1750-5836(07)00092-8.

Smith, S. V., and G. S. Key (1975), Carbon Dioxide and Metabolism in Marine Environments, *Limnol. Oceanogr.*, *20*(3), 493–495.

Takahashi, T. et al. (2009), Climatological mean and decadal change in surface ocean pCO2, and net sea–air CO2 flux over the global oceans, *Deep Sea Res. Part II Top. Stud. Oceanogr.*, *56*(8-10), 554–577, doi:10.1016/j.dsr2.2008.12.009.

Taylor, J. K., and E. R. Smith (1939), Reproducibility of silver-silver halide electrodes, *Natl. Bur. Stand.*, *22*(1938), 307–314.

Vaslow, F. V., and G. E. Boyd (1952), Thermodynamics of Coprecipitation : Dilute Solid Solutions of AgBr in AgCll, *J. Am. Chem. Soc.*, *74*(18), 4691–4695.

CHAPTER 4: THE EFFECTS OF PRESSURE ON TRIS BUFFER IN SYNTHETIC SEAWATER

Abstract

Equimolar Tris (2-amino-2-hydroxymethyl-propane-1,3-diol) buffer prepared in artificial seawater media is a widely accepted pH standard for oceanographic pH measurements, though its change in pH over pressure is largely unknown. The change in volume (ΔV) of dissociation reactions can be used to estimate the effects of pressure on the dissociation constant of weak acid and bases. The ΔV of Tris in seawater media of salinity 35 ($\Delta V_{\mathrm{Tris}}^{\mathrm{SW}}$) was determined between 5 and 40 °C using potentiometry. The potentiometric cell consisted of a modified high pressure tolerant Ion Sensitive Field Effect Transistor pH sensor and a Chloride-Ion Selective Electrode directly exposed to solution. The effects of pressure on the potentiometric cell were quantified in aqueous HCl solution prior to measurements in Tris buffer. The experimentally determined $\Delta V_{\mathrm{Tris}}^{\mathrm{SW}}$ were fitted to the equation $-0.0073T_C^2 + 0.55T_C + 4.7$, where T_C is temperature in Celsius; the resultant fit agreed to experimental data within uncertainty of the measurements, which was estimated to be 1.4 cm^{-3} mol^{-1}. Using the results presented here, pH of Tris buffer can be constrained to better than 0.005 at 200 bar.

Glossary of Terms

Cl-ISE	Chloride-Ion Selective Electrode
E	Measured electromotive force (EMF) of the cell ISFET|Cl-ISE
$E_{\mathrm{ref}}(T,P)$	Reference potential for the cell ISFET|Cl-ISE at T and P on the free hydrogen ion concentration scale
$E^*_{\mathrm{ref}}(T,P)$	Reference potential for the cell ISFET|Cl-ISE at T and P on the total hydrogen ion concentration scale
F	Faraday Constant (96485 C mol^{-1})
$f(T,P)$	Change in E due to pressure induced strain on the ISFET
ISFET	Ion Sensitive Field Effect Transistor
K_i^P	Acidity constant for species i at P
m_{i}	Molality of species i
m^*_{H}	Molality of hydrogen ion on the total scale; $m^*_H = m_H\left(1+\frac{SO4_T}{K_{HSO4}}\right)$
R_{G}	Gas constant (83.145 cm^3 bar mol^{-1} K^{-1})
R	Universal gas constant (8.3145 J K^{-1} mol^{-1})
P	Gauge Pressure (Bar)
pH	pH on the free hydrogen ion concentration scale; $pH = -\log(m_H)$
pH_T	pH on the total hydrogen ion concentration scale; $pH_T = -\log(m^*_H)$
k	Nernst Slope; $k = RT_K \cdot \ln(10)/F$
$SO4_T$	Total sulfate concentration; $SO4_T = m_{HSO_4^-} + m_{SO_4^{2-}}$
T_{K}	Temperature in Kelvin
T_{C}	Temperature in Celsius
ΔV_{i}	Difference in partial molal volume of the acid dissociation reaction for species i [cm^3 mol^{-1}]
ΔV_i^{SW}	Difference in partial molal volume of the acid dissociation reaction for species i in seawater media (salinity = 35) [cm^3 mol^{-1}]
$\bar{V}°_{\mathrm{i}}$	Partial molal volume of species i at infinite dilution [cm^3 mol^{-1}]
$\bar{V}_{\mathrm{i}}$	Partial molal volume of species i in the ionic medium [cm^3 mol^{-1}]
$\bar{V}_{\mathrm{i}}^{\mathrm{SW}}$	Partial molal volume of species i in seawater media (salinity = 35) [cm^3 mol^{-1}]
γ_i	Activity coefficient for species i
$\gamma_{\pm\mathrm{HCl}}$	Mean activity coefficient of HCl, where $\gamma_{\pm HCl} = (\gamma_H\gamma_{Cl})^{1/2}$
$\Delta\kappa_{\mathrm{i}}$	Difference in partial molal compressibility of the acid dissociation reaction for species i [cm^3 mol^{-1} Bar^{-1}]

$\Delta\kappa_i^{SW}$	Difference in partial molal compressibility of the acid dissociation reaction for species i in seawater media (salinity = 35) [cm^3 mol^{-1} Bar^{-1}]
$\bar{\kappa}^{\circ}_i$	Partial molal compressibility of species i at infinite dilution [cm^3 mol^{-1} bar^{-1}]
$\bar{\kappa}_i$	Partial molal compressibility of species i in the ionic medium [cm^3 mol^{-1} bar^{-1}]
$\bar{\kappa}_i^{SW}$	Partial molal compressibility of species i in seawater media (salinity = 35) [cm^3 mol^{-1} bar^{-1}]

Introduction

Open ocean pH is declining at rates between -0.001 to -0.002 pH yr^{-1} as atmospheric CO_2 increases and the surface ocean equilibrates with larger partial pressures of CO_2 [*Dore et al.*, 2009; *Byrne et al.*, 2010; *Bates et al.*, 2014]. Decreases in pH may have large impacts on ocean ecosystems, particularly on organisms that make calcium carbonate skeletons and shells [*Barton et al.*, 2012; *Bednaršek et al.*, 2012]. It is expected that rates of pH change will not be uniform [*Feely et al.*, 2008; *Wootton et al.*, 2008], and different regions will experience varying degrees of impact. The rate of decrease has been observed directly at a few long-term time series stations [*Bates et al.*, 2014] using highly reproducible spectrophotometric pH measurements [*Clayton and Byrne*, 1993; *Liu et al.*, 2011]. The expense and expertise required to sustain such observations prevent them from being scaled to large areas of the ocean. Alternatively, a monitoring system that utilizes autonomous chemical sensors may alleviate such problems and greatly improve our understanding of the spatial and temporal variability of the rate of pH decline in the ocean. However, in order to establish such a chemical sensor network, the development and implementation of stringent calibration protocols are necessary.

The assignment of proper pH values to a suitable buffer solution is essential in obtaining accurate pH measurements [*Bates*, 1973]. Equimolar Tris (2-amino-2-hydroxymethyl-propane-1,3-diol) buffer prepared in artificial seawater (referred to as just Tris buffer hereafter) has been widely accepted as the primary pH standard for oceanographic pH measurements [*Dickson*, 1993; *DelValls and Dickson*, 1998], and

has been used to calibrate potentiometric pH measurements [*Millero et al.*, 1993; *Martz et al.*, 2010], and to characterize indicator dyes used in spectrophotometric pH measurements [*Clayton and Byrne*, 1993; *Liu et al.*, 2011]. Although the temperature and salinity dependence of the dissociation constant of Tris has been quantified at 0 gauge pressure (K^0_{Tris}) [*DelValls and Dickson*, 1998], its pressure dependence has yet to be determined in seawater media. As the number of in situ pH measurements at high pressures is expected to increase rapidly in the next decade due to improvements in robust pH sensor technology, characterizing Tris buffer in seawater under high pressures will meet a crucial need in sensor calibration and traceability.

The relationship between the dissociation constant at in situ gauge pressure ($K_{\mathrm{i}}^{\mathrm{P}}$) and at 0 gauge pressure (K_{i}^{0}) is given by

$$\log\left(\frac{K_{\mathrm{i}}^{\mathrm{P}}}{K_{\mathrm{i}}^{0}}\right) = \frac{-\Delta V_{\mathrm{i}} P + 0.5\Delta\kappa_{\mathrm{i}} P^2}{\ln(10) R_{\mathrm{G}} T_{\mathrm{K}}} \qquad (4.1)$$

where ΔV_{i} [cm^3 mol^{-1}] and $\Delta\kappa_{\mathrm{i}}$ [cm^3 mol^{-1} bar^{-1}] are the differences in partial molal volume and compressibility of the acid dissociation reaction, respectively, R_{G} is the gas constant (83.145 cm^3 bar mol^{-1} K^{-1}), T_{K} is temperature in Kelvin, and P is gauge pressure in bar [*Byrne and Laurie*, 1999; *Millero*, 2001]. The ΔV_{Tris} at infinite dilution and in low ionic strength solutions ($\leq$ 0.1 mol dm^{-3} NaCl) has been reported using dilatometry [*Katz and Miller*, 1971; *Kitamura and Itoh*, 1987] and spectrophotometry [*Neuman et al.*, 1973]. However, since ΔV is dependent on ionic strength and solution composition [*Byrne and Laurie*, 1999], ΔV_{tris} must be quantified in seawater media for high accuracy in situ pH sensor calibration.

Here, we report $\Delta V_{\mathrm{Tris}}^{\mathrm{SW}}$ between 5 – 40 °C, where the superscript SW refers to seawater media of salinity 35. A potentiometric cell consisting of an Ion Senstive Field Effect Transistor (ISFET) pH sensor and a Chloride-Ion Selective Electrode (Cl-ISE) was utilized to quantify the effects of pressure on K_{Tris} up to 200 bar. Sources of uncertainty for the reported values are explored.

Background and Theory

The pressure dependence of K_{Tris} can be calculated by monitoring the solution pH over a range of pressures. The left hand side of equation (1) is equivalent to the difference in solution pH at 0 and experimental P (pH^0 – pH^{P}), given that the concentration of H^+ and OH^- is negligible compared to the buffer concentration:

$$(\mathrm{pH}^0 - \mathrm{pH}^{\mathrm{P}}) = \frac{-\Delta V_{\mathrm{i}} P + 0.5 \Delta \kappa_{\mathrm{i}} P^2}{\ln(10) R_{\mathrm{G}} T_{\mathrm{K}}} \qquad (4.2)$$

Therefore $\Delta V_{\mathrm{Tris}}^{\mathrm{SW}}$ and $\Delta \kappa_{\mathrm{Tris}}^{\mathrm{SW}}$ can be quantified from a second order polynomial regression between $R_{\mathrm{G}} \cdot T_{\mathrm{K}} \cdot \ln(\mathrm{pH}^0 - \mathrm{pH}^{\mathrm{P}})$ versus pressure.

The pH of the solution was quantified using the cell ISFET|Cl-ISE. The operating principle of ISFET pH sensors is based on potentiometry, though significantly differs from conventional potentiometric electrodes such as the glass electrode. The ISFET is an active electronic circuit, in which the potential between the reference electrode and the source of the transistor follows the Nernst equation, given that the gate insulator material has sufficient buffer capacity [*Bergveld*, 2003]. The ISFET utilized in the Honeywell Durafet line of pH sensors (referred to as ISFET hereafter) with a Cl-ISE directly exposed to solution as the reference electrode have

been shown to produce extremely stable measurements in seawater for months to years at 1 atm [*Martz et al.*, 2010]. The Cl-ISE is especially well suited for high pressure applications, as it seems to exhibit minimal pressure hysteresis [*Shitashima et al.*, 2002]. These traits make ISFET|Cl-ISE a good candidate for characterizing Tris buffer over periods of weeks to months.

The electromotive force (EMF) of the cell ISFET|Cl-ISE can be explained by the Nernst relation:

$$E_{\mathrm{ISFET|Cl-ISE}} = E_{\mathrm{ref}}(T,P) - k\log(\gamma_{\pm\mathrm{HCl}}{}^{2} m_{\mathrm{H}} m_{\mathrm{Cl}}) \tag{4.3}$$

where $E_{\mathrm{ref}}(T,P)$ is the reference potential at experimental T and P, k is the Nernst slope, m is the molality of the respective ions, and $\gamma_{\pm\mathrm{HCl}}$ is the mean activity coefficient of HCl ($\gamma_{\pm\mathrm{HCl}} = (\gamma_{\mathrm{H}}\gamma_{\mathrm{Cl}})^{1/2}$); the Nernst slope is defined as $k = RT_{\mathrm{K}}\ln(10)/F$, where R is the universal gas constant (8.3145 J K^{-1} mol^{-1}), and F is the Faraday constant (96485 C mol^{-1}). Although the E_{ref} is analogous to the "standard potential", it is referred to as the reference potential because of the large variability between ISFET sensors [*Martz et al.*, 2010]. Rearranging equation (4.3) for pH, defined as the $-\log(m_{\mathrm{H}})$, gives

$$\begin{aligned} -\log(m_{\mathrm{H}}) &= \mathrm{pH} \\ &= \frac{(E_{\mathrm{ISFET|Cl-ISE}} - E_{\mathrm{ref}}(T,P)) + k\log(\gamma_{\pm\mathrm{HCl}}{}^{2} m_{\mathrm{Cl}})}{k} \end{aligned} \tag{4.4}$$

In order to calculate pH at experimental conditions, the *T*-*P* induced changes on $E_{\mathrm{ref}}(T,P)$ and $\gamma_{\pm\mathrm{HCl}}$ must be quantified (m_{Cl}, however, is independent of *T* and *P*).

The relationship between the activity coefficient of species i at experimental pressure, γ_{i}^{P}, and its activity coefficient at 0 bar, γ_{i}^{0}, is given by

$$\ln\left(\frac{\gamma_{\mathrm{i}}^{\mathrm{P}}}{\gamma_{\mathrm{i}}^{0}}\right)=\left(\frac{-(\bar{V}_{\mathrm{i}}-\bar{V}^{\circ}{}_{\mathrm{i}})}{R_{\mathrm{G}}T_{\mathrm{K}}}\right)P+\left(\frac{0.5(\bar{\kappa}_{\mathrm{i}}-\bar{\kappa}^{\circ}{}_{\mathrm{i}})}{R_{\mathrm{G}}T_{\mathrm{K}}}\right)P^{2} \qquad (4.5)$$

where $\bar{V}_{\mathrm{i}}$ and $\bar{\kappa}_{\mathrm{i}}$ are the partial molal volume and compressibility in the ionic medium, respectively, and the ° symbol refers to the reference state at infinite dilution [*Byrne and Laurie*, 1999]. By convention, the partial molal quantities of H^{+} are 0 under all conditions [*Millero*, 2001], thus for this study, we assume $\gamma_{\pm\mathrm{HCl}}^{P}/\gamma_{\pm\mathrm{HCl}}^{0}=\gamma_{\mathrm{Cl}}^{P}/\gamma_{\mathrm{Cl}}^{0}$.

Characterizing E_{ref}(T,P)

The $E_{\mathrm{ref}}(T,0)$ can be quantified using a linear relationship [*Connery et al.*, 1992; *Martz et al.*, 2010], however, the pressure response deviates from a simple linear response, and must be determined for every sensor individually. Furthermore, the pressure response of E_{ref}, induced by strain on the ISFET and mounting mechanism, is slightly temperature dependent and must be characterized over the temperature range of interest. The pressure response of E_{ref} at a given temperature can be expressed as

$$E_{\mathrm{ref}}(T,P)=E_{\mathrm{ref}}(T,0)+f(T,P)+\frac{-\Delta V_{\mathrm{AgCl}}P\ +\ 0.5\Delta\kappa_{\mathrm{AgCl}}P^{2}}{10F} \qquad (4.6)$$

where $f(T,P)$ is the pressure response of the ISFET, and the 10 in the denominator converts units for the gas constant. The second term on the right describes the pressure induced change in solubility of the Cl-ISE, and ΔV_{AgCl} and $\Delta\kappa_{\mathrm{AgCl}}$ refer to the

difference in partial molal volume and compressibility of the redox reaction of the Cl-ISE:

$$AgCl_{(s)} + e^- \leftrightarrow Ag_{(s)} + Cl_{(aq)}^- \quad (4.7)$$

Since partial molal quantities of solids are 0, ΔV_{AgCl} and $\Delta \kappa_{AgCl}$ are equivalent to $\bar{V}_{Cl}$ and $\bar{\kappa}_{Cl}$, respectively; note that these partial molal quantities are solution dependent. The $\bar{V}_{Cl}^{SW}$ and $\bar{\kappa}_{Cl}^{SW}$ is known [*Millero*, 1982], thus, pH of Tris buffer can be quantified at experimental *P*, if *f*(*T*,*P*) is characterized.

The *f*(T,P) can be quantified by measuring $E_{ISFET|Cl\text{-}ISE}$ in a solution where the activity of HCl, $\bar{V}_{Cl}$, and $\bar{\kappa}_{Cl}$ are known over the desired range of *T* and *P*. Combining equations (4.3) and (4.6) gives

$$f(T,P) = E_{ISFET|Cl-ISE} + k\log(\gamma_{\pm HCl}{}^2 m_H m_{Cl}) - E_{ref}(T,0) - \frac{-\bar{V}_{Cl}P + 0.5\bar{\kappa}_{Cl}P^2}{10F} \quad (4.8)$$

Aqueous HCl is an ideal solution for this approach since HCl is fully dissociated, thus m_H and m_{Cl} are independent of *T* and *P*, $\gamma_{\pm HCl}$ is well characterized over a wide range of temperature [*Harned and Ehlers*, 1932; *Harned and Owen*, 1963], and the partial molal quantities of Cl^- in HCl media are known [*Millero*, 1982]. Furthermore, the effect of pressure on $\gamma_{\pm HCl}$ in 0.01 m HCl solution is negligible (<10 µV at 200 bar) [*Harned and Owen*, 1963]. Once *f*(*T*,*P*) is quantified for a given ISFET|Cl-ISE cell, then it can be used to measure pH of Tris buffer at experimental *T* and *P* (equation (4.4) and (4.6)) to quantify ΔV_{Tris}^{SW} (equation (4.2)).

Determining ΔV_{Tris}^{SW}.

The pH of Tris buffer is reported on the total hydrogen ion concentration scale [*DelValls and Dickson*, 1998], and is defined as $pH_T = -\log(m_H^*)$;

$$m_H^* = m_H\left(1 + \frac{SO4_T}{K_{HSO4^-}}\right) \tag{4.9}$$

where $SO4_T$ is the total sulfate concentration ($m_{HSO_4^-} + m_{SO_4^{2-}}$), and $K_{HSO_4^-}$ is the acidity constant for bisulfate. Therefore the pH on the total scale at experimental pressure (pH_T^P) must be determined to quantify ΔV_{Tris}^{SW} and $\Delta\kappa_{Tris}^{SW}$ using equation (4.2). pH_T can be calculated by:

$$\begin{aligned} pH_T &= -\log(m_H^*) \\ &= \frac{E_{ISFET|Cl-ISE} - E_{ref}^*(T,P) + k\log(\gamma_{\pm HCl}{}^2 m_{Cl})}{k} \end{aligned} \tag{4.10}$$

where $E_{ref}^*(T,P)$ is the reference potential on the total hydrogen ion concentration scale, and is defined as

$$E_{ref}^*(T,P) = E_{ref}(T,P) + k\log\left(1 + \frac{SO4_T}{K_{HSO4}^P}\right) \tag{4.11}$$

The $SO4_T$ was quantified assuming salinity = 35 [*Dickson et al.*, 2007], and K_{HSO4}^P was calculated from equation (4.1), using K_{HSO4}^0 from *Dickson*, 1990, and $\Delta V_{HSO4}^{SW}$and $\Delta\kappa_{HSO4}^{SW}$ from *Millero*, 1982. E_{ref}(T,P) was calculated using $\bar{V}_{Cl}^{SW}$ and $\bar{\kappa}_{Cl}^{SW}$, [*Millero*, 1982]) and the *f*(*T*,*P*) quantified in aqueous HCl (equation (4.6)). Finally, the pressure

effect on $\gamma_{\pm\mathrm{HCl}}$ is not negligible in Tris (~ 200 µV at 200 bar), thus equation (4.5) was used to calculate $\gamma^{P}_{\pm\mathrm{HCl}}$.

Materials and Methods

Experimental Apparatus

Temperature and pressure cycles were carried out in a custom system capable of reproducing a *T-P* range of 0 - 40 °C, and 0 – 200 bar. The ISFET|Cl-ISE cells were placed into a vessel consisting of a titanium housing with an inert PEEK insert as the wetted material. The *T* and *P* of the housing is controlled by a temperature bath (Thermo Scientific, RTE-7) and an ISCO 260D Syringe pump, respectively. The pressure chamber was placed in an air bath (controlled by the same water bath) in order to improve temperature stability. Temperature was measured using a YSI 4600 thermometer with an Omega thermistor (P/N ON-410-PP), and pressure was measured using an Omega analog pressure sensor (P/N: PX409-5.0KG5V-XL). The thermistor was calibrated between 0 – 40 °C using a Hart 5611T thermistor (estimated accuracy of 0.01 °C). The factory calibration was used for the pressure sensor (accuracy of 0.03%).

Modified, high-pressure tolerant ISFETs were used for this study, since commercially available Durafets are only capable of withstanding pressures up to 6.9 bar (100 psi). Cl-ISE pellets were purchased from Van London, and packaged in-house. Two ISFET|Cl-ISE cells (DF52 and DF53) were simultaneously operated in either a 0.0100 ± 0.0001 m HCl or Tris buffer solution; HCl was prepared gravimetrically using a 1 mol dm^{-3} HCl standard solution (Fisher, SA48-1), and a

certified Tris buffer distributed by the Dickson lab (batch 8) was used. A 24-bit Analog to Digital Converter (NI-9219) was used to measure $E_{ISFET|Cl\text{-}ISE}$ every 45 seconds. All electronics except for the water bath were powered through an isolation transformer to eliminate potential ground loop issues.

Experimental Procedure

The *T* and *P* were controlled through a LabView interface, and pressure was cycled between 0 – 200 bar at a rate of 0.016 ml min^{-1}, taking approximately 8 hours for a full compression/decompression cycle. This resulted in > 600 discrete measurements per pressure cycle. Pressure cycles were performed at 9 different temperatures at 5 °C intervals between 0 and 40 °C (n = 6 for HCl, n = 9 for Tris buffer at each temperature). This was repeated twice, to serve as replicate estimates for $f(T,P)$ and $\Delta V_{\mathrm{Tris}}^{\mathrm{SW}}$. The first pressure cycle at a new temperature was discarded due to incomplete thermal equilibration of the housing. Furthermore, only the data collected during increasing pressure were used in the analysis, since $E_{ISFET|Cl\text{-}ISE}$ showed better agreement between different pressure cycles than using data from the entire pressure cycle (agreement was better than 60 µV; 1 σ).

The $f(T,P)$ at each temperature was quantified as the average of 5 pressure cycles, and its repeatability and stability were assessed by comparing results from replicates. We assumed that $f(T,P)$ remained constant between HCl and seawater media, though this assumption was not tested. The $\Delta V_{\mathrm{Tris}}^{\mathrm{SW}}$ was quantified as the average of 8 pressure cycles.

Results and Discussion

Characterization of f(T,P)

DF52 and DF53 had distinct, yet repeatable $f(T,P)$ at each temperature (Figure 4.1). The mean $f(T,P)$ at each temperature were binned into 5 dbar intervals to produce a look up table to prevent the small yet significant biases resulting from a high order polynomial fit. The stability of $f(T,P)$ was assessed by comparing replicate estimations of $f(T,P)$ at each temperature; depending on the temperature, these replicate measurements could have taken place weeks to months apart. Both cells showed adequate stability and repeatability. Agreement of $f(T,P)$ between replicates between 0 – 200 bar and 0 – 40 °C was 50 µV for DF53, and 200µV for DF52, demonstrating the long term stability of the sensor performance.

A general trend of greater $|f(T,P)|$ at lower temperatures for pressures < 170 bar, and the reverse at pressures > 170 bar, was observed for both cells. The effects of temperature are not completely independent of pressure, and vice versa. Failure to account for this small, yet detectable, cross-sensitivity could lead to errors up to ~370 µV (e.g. when comparing $f(0°C,P)$ and $f(40°C,P)$. These results imply errors of up to 0.005 pH, if, for example, $f(T,P)$, quantified at a single temperature is extended over the entire pressure and temperature range; this would lead to an uncertainty in $\Delta V_{\mathrm{Tris}}^{\mathrm{SW}}$ of 1.5 ml mol^{-1}. As stated above, the calibration process employed in this work leads to pH stability of 200 µV or ~0.003 pH, which translate into an uncertainty in $\Delta V_{\mathrm{Tris}}^{\mathrm{SW}}$ of 0.9 ml mol^{-1}.

Determination of ΔV_{Tris}^{SW}

The $\Delta V_{\mathrm{Tris}}^{\mathrm{SW}}$ was calculated as the slope of a regression for $-R_G T_K \ln(pH^0 - pH^P)$ versus P (equation (4.2)) between 30 and 200 bar (Figure 4.2) over the range 5-40 °C. The magnitude and sign of the change in pH_T of Tris buffer between 0 and 200 bar is highly dependent on temperature. For example pH_T of Tris buffer increases by ~0.03 at 25°C, whereas it decreases by ~0.007 at 5 °C. Sensor noise often increased with a full depressurization of the sensors, theorized to be due to nucleation of an air bubble in the open gate of the FET. Therefore, regression was limited to data above 30 bar. The $\Delta \kappa_{\mathrm{Tris}}^{\mathrm{SW}}$ was not calculated because the fit of the data did not improve the quality of the fit from a linear to quadratic regression. This is most likely because the effects of partial molal compressibility are usually not significant at pressures below 1000 bar [*Byrne and Laurie*, 1999].

Unfortunately, following several weeks of good operation, both DF52 and DF53 malfunctioned before $\Delta V_{\mathrm{Tris}}^{\mathrm{SW}}$ could be quantified at temperatures below 5 °C. Both DF52 and DF53 failed or began to exhibit erratic behavior partway through the second set of replicate pressure cycles. In summary, $\Delta V_{\mathrm{Tris}}^{\mathrm{SW}}$ was quantified a total of 15 times at 8 temperatures between 5 – 40 °C, with replicates at temperatures ≥ 25°C (Table 4.1). The mean $\Delta V_{\mathrm{Tris}}^{\mathrm{SW}}$ was fitted to the equation

$$AT_C^2 + BT_C + C \tag{4.12}$$

where T_C is temperature in Celsius, A = -0.0073, B = 0.55, and C = 4.70. This quadratic equation agrees to experimental data within the uncertainty of the measurements (see below).

The uncertainty in the determined $\Delta V_{\mathrm{Tris}}^{\mathrm{SW}}$ is directly associated to our ability to quantify the relative change in pH between atmospheric and experimental pressure (equation (4.2)). The sources of error and their contribution to the uncertainty at 200 bar based on standard propagation of uncertainty calculations [*EURACHEM/CITAC*, 2000], are listed in Table 4.2. These results indicate that the change in pH of Tris due to change in pressure of 200 Bar can be constrained to 0.0048, which translates to an uncertainty in $\Delta V_{\mathrm{Tris}}^{\mathrm{SW}}$ of 1.4 cm^3 mol^{-1}; the effect of temperature on this value is small, and changes by < 0.1 cm^3 mol^{-1} between 5 – 40 °C. It is apparent that the two dominant sources of error in our study, i.e., uncertainties in $f(T,P)$ and sensor stability, account for 86% of the overall uncertainty.

The ΔV_{Tris} reported in the literature cannot be directly compared to the results here, because previous studies have either determined volumetric properties at infinite dilution [*Neuman et al.*, 1973; *Kitamura and Itoh*, 1987; *Ford et al.*, 2000] or at ionic strengths significantly lower than seawater (0.1mol dm^{-3} NaCl) [*Katz and Miller*, 1971]. The ΔV_{Tris} reported at infinite dilution and 25°C (1-4.3 cm^3 mol^{-1}) were lower than those found in this study, 4.6-5.9 cm^3 mol^{-1}. This is consistent with expectations, since partial molal volumes of cations increase with ionic strength (i.e. protonated form of Tris) [*Millero*, 2001]. Furthermore, Ford et al., 2000 observed a positive correlation between temperature and ΔV_{Tris} as well, though their trend was significantly smaller than this study. Overall, the $\Delta V_{\mathrm{Tris}}^{\mathrm{SW}}$ at 25°C seems to be consistent with reported values, however, the small effects of temperature reported in this study

are near the detection limit of the methodology and should be confirmed using other approaches.

Conclusion

The $\Delta V_{\mathrm{Tris}}^{\mathrm{SW}}$ was quantified between 5 and 40 °C at 5 °C intervals, using a modified high pressure tolerant ISFET pH sensor and a Cl-ISE as a reference electrode. A custom system was utilized to control temperature and pressure between 5 – 40 °C, and 0 – 200 bar. The pressure response of the cell ISFET|Cl-ISE ($f(T,P)$) was quantified in aqueous HCl solution prior to measurements in a certified Tris buffer solution. The $\Delta V_{\mathrm{Tris}}^{\mathrm{SW}}$ were fit to a second order polynomial regression as a function of temperature; the formulation agrees to experimental data within the experimental uncertainty, which was estimated to be 1.4 cm^3 mol^{-1}. Potential uses of this information include benchtop and in situ calibration of pH sensors at elevated pressures in a widely accepted seawater pH standard (Tris in artificial seawater). The pH of Tris buffer at pressures up to 200 bar can be calculated with a combined uncertainty of 0.005 using the results presented in this study.

Acknowledgements

This work was supported by the National Oceanographic Partnership Program award N00014-10-1-0206.

Chapter 3, in full is currently being prepared for submission for publication of the material. Takeshita, Y., Martz, T.R., Johnson, K.S. and Jannasch, H.W. The dissertation author was the primary investigator and author of this paper.

Table 4.1: $\Delta V_{\mathrm{Tris}}^{\mathrm{SW}}$ [cm^3 mol^{-1}] between 5 – 40 °C

Temperature	Trial	DF52_1[a]	DF52_2[a]	DF53
5	1	—	—	-1.4
10	1	—	—	-0.4
15	1	—	—	1.1
20	1	—	—	2.9
25	1	5.9	4.9	4.6
30	1	5.8	5.5	7.0
35	1	4.9	5.3	7.0
40	1	4.7	—	5.5

[a] Number after the underscore indicates repetition number.

Table 4.2: Summary of Propagation of Uncertainty for Calculated pH at Experimental Conditions

Source of Error	Error	Uncertainty in pH [a]
Sensor Stability	200 µV	0.0034
f(T,P)	200 µV	0.0034
$\Delta \mathbf{V}^{\mathbf{SW}}_{\mathbf{HSO4}}$	0.1[b] cm^3 mol^{-1}	0.0001
$\Delta \boldsymbol{\kappa}^{\mathbf{SW}}_{\mathbf{HSO4}}$	0.001[d] cm^3 mol^{-1} bar^{-1}	0.0001
$\overline{V}_{Cl}$	0.1[b] cm^3 mol^{-1}	0.0005
$-\overline{V^{\circ}}_{Cl}$	0.3[c] cm^3 mol^{-1}	0.0007
$\overline{\kappa}_{Cl}$	3×10^{-4}[d] cm^3 mol^{-1} bar^{-1}	0.0000
$\overline{\kappa^{\circ}}_{Cl}$	2×10^{-5}[d] cm^3 mol^{-1} bar^{-1}	0.0001
Total		0.0048

[a] pH calculated at 200 bar and 25 °C
[b] Error from [*Poisson and Chanu*, 1976]
[c] Error from [*Millero*, 1982]
[d] Error was estimated using 50% relative uncertainty

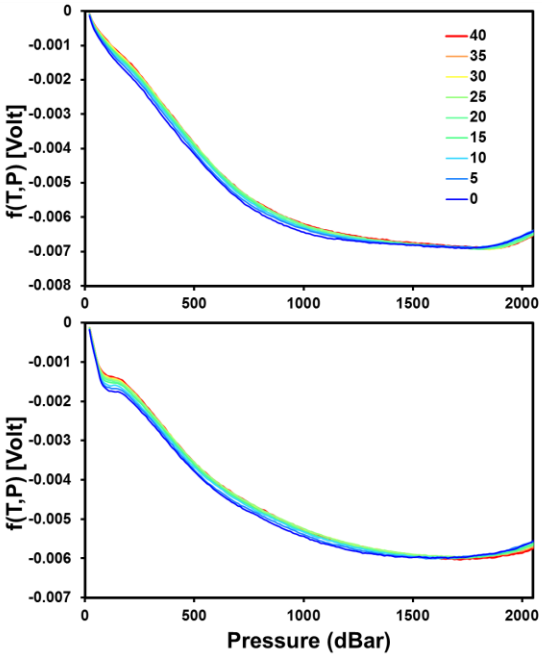

Figure 4.1: *f*(*T*,*P*) characterized between 0 – 40 °C using DF52 (top) and DF53 (bottom).

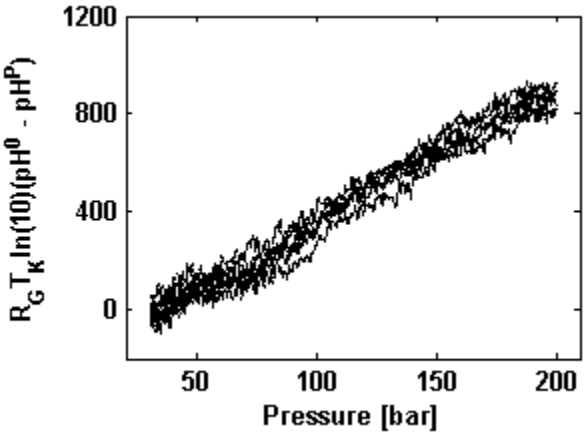

Figure 4.2: Typical results of a set of pressure at a constant temperature used to determine on the ΔV_{Tris}^{SW} (data were collected using DF52 at 30 °C).

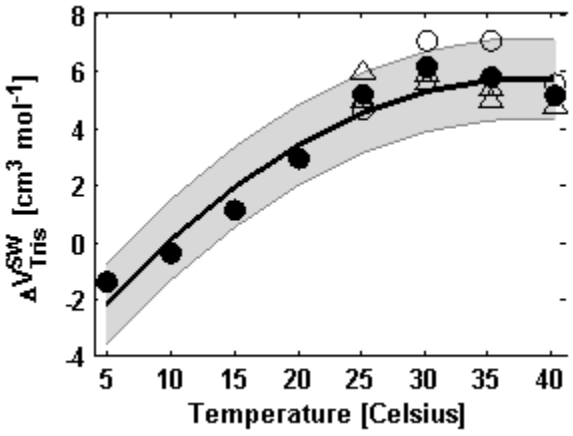

Figure 4.3: ΔV_{Tris}^{SW} versus temperature. The mean (closed circles), and values determined by DF52 (open triangles) and DF53 (open circles) are shown. The result of a 2nd order polynomial regression is represented by the black solid line, and the shaded area represent experimental uncertainty (1.4 cm^3 mol^{-1}).

References

Barton, A., B. Hales, G. G. Waldbusser, C. Langdon, and R. a. Feely (2012), The Pacific oyster, Crassostrea gigas, shows negative correlation to naturally elevated carbon dioxide levels: Implications for near-term ocean acidification effects, *Limnol. Oceanogr.*, *57*(3), 698–710, doi:10.4319/lo.2012.57.3.0698.

Bates, N. R., Y. M. Astor, M. J. Church, K. Currie, J. E. Dore, M. Gonzalez-Davila, L. Lorenzoni, F. Muller-karger, J. Olafsson, and J. M. Santana-Casiano (2014), A Time-Series View of Changing Surface Ocean Chemistry Due to Ocean Uptake of Anthropogenic CO2 and Ocean Acidification, *Oceanography*, *1*, 126–141.

Bates, R. G. (1973), *Determination of pH Theory and Practice*, 2nd ed., John Wiley & Sons, Inc., New York.

Bednaršek, N. et al. (2012), Extensive dissolution of live pteropods in the Southern Ocean, *Nat. Geosci.*, *5*(12), 881–885, doi:10.1038/ngeo1635.

Bergveld, P. (2003), ISFET , Theory and Practice, in *IEEE Sensor Conference*, pp. 1–26, Toronto.

Byrne, R. H., and S. H. Laurie (1999), Influence of Pressure on Chemical Equilbria in Aqueous Systems - With Particular Reference to Seawater, *Pure Appl. Chem.*, *71*(5), 871–890.

Byrne, R. H., S. Mecking, R. A. Feely, and X. Liu (2010), Direct observations of basin-wide acidification of the North Pacific Ocean, *Geophys. Res. Lett.*, *37*(2), 1–5, doi:10.1029/2009GL040999.

Clayton, T. D., and R. H. Byrne (1993), Spectrophotometric seawater pH measurements : total hydrogen results, *Deep Sea Res. Part I Oceanogr. Res. Pap.*, *40*(10), 2115–2129.

Connery, J. G., R. D. Baxter, and C. W. Gulczynski (1992), Development and Performance Characteristics of a New pH Electrode, in *Pittsburgh Conference*, pp. 1–4.

DelValls, T. A., and A. G. Dickson (1998), The pH of buffers based on 2-amino-2-hydroxymethyl-1,3-propanediol (“tris”) in synthetic sea water, *Deep Sea Res. Part I Oceanogr. Res. Pap.*, *45*(9), 1541–1554.

Dickson, A. G. (1990), Standard potential of the reaction : AgCl (s) + 1/2H2(g) = Ag (s) + HCl (aq), and the standard acidity constant of the ion HSO4- in

synthetic sea water from 273 . 15 to 318 . 15 K, *J. Chem. Thermodyn.*, *22*(3), 113–127.

Dickson, A. G. (1993), pH buffers for sea water media based on the total hydrogen ion concentration scale, *Deep Sea Res. Part I Oceanogr. Res. Pap.*, *40*(1), 107–118, doi:10.1016/0967-0637(93)90055-8.

Dickson, A. G., C. L. Sabine, and J. R. Christian (Eds.) (2007), *Guide to best practices for ocean CO2 measurements*, PICES Special Publication 3.

Dore, J. E., R. Lukas, D. W. Sadler, M. J. Church, and D. M. Karl (2009), Physical and biogeochemical modulation of ocean acidification in the central North Pacific., *Proc. Natl. Acad. Sci. U. S. A.*, *106*(30), 12235–40, doi:10.1073/pnas.0906044106.

EURACHEM/CITAC (2000), *Quantifying Uncertainty in Analytical Measurement*, edited by S. L. R. Ellison, M. Rosslein, and A. Williams.

Feely, R. A., C. L. Sabine, J. M. Hernandez-Ayon, D. Ianson, and B. Hales (2008), Evidence for upwelling of corrosive "acidified" water onto the continental shelf., *Science*, *320*(5882), 1490–2, doi:10.1126/science.1155676.

Ford, T. D., T. G. Call, M. L. Origlia, M. a. Stark, and E. M. Woolley (2000), Apparent molar volumes and apparent molar heat capacities of aqueous 2-amino-2- hydroxymethyl-propan-1,3-diol (Tris or THAM) and THAM plus equimolal HCl, *J. Chem. Thermodyn.*, *32*(4), 499–516, doi:10.1006/jcht.1999.0617.

Harned, H. S., and R. W. Ehlers (1932), The Dissociation Constant of Acetic Acid from 0 To 35 Centigrade, *J. Am. Chem. Soc.*, *54*, 1350–1357.

Harned, H. S., and B. B. Owen (1963), *The Physical Chemistry of Electrolytic Solutions*, 3rd ed., Reinhold Pub. Corp., New York.

Katz, S., and J. E. Miller (1971), Medium Effects of Some Denaturing Agents on Volume Changes, *J. Phys. Chem.*, *75*(8), 1120–1125.

Kitamura, Y., and T. Itoh (1987), Reaction Volume of Protonic Ionization for Buffering Agents . Prediction of Pressure Dependence of pH and pOH, *J. Solution Chem.*, *16*(9), 715–725.

Liu, X., M. C. Patsavas, and R. H. Byrne (2011), Purification and characterization of meta-cresol purple for spectrophotometric seawater pH measurements., *Environ. Sci. Technol.*, *45*(11), 4862–8, doi:10.1021/es200665d.

Martz, T. R., J. G. Connery, and K. S. Johnson (2010), Testing the Honeywell Durafet for seawater pH applications, *Limnol. Oceanogr. Methods*, *8*, 172–184, doi:10.4319/lom.2010.8.172.

Millero, F. J. (1982), The effect of pressure on the solubility of minerals in water and seawater, *Geochim. Cosmochim. Acta*, *46*, 11–22.

Millero, F. J. (2001), *Physical Chemistry of Natural Waters*, 1st ed., John Wiley & Sons, Inc., New York.

Millero, F. J., J.-Z. Zhang, S. Fiol, S. Sotolongo, R. N. Roy, K. Lee, and S. Mane (1993), The use of buffers to measure the pH of seawater, *Mar. Chem.*, *44*(2-4), 143–152.

Neuman, R. C. J., W. Kauzmann, and A. Zipp (1973), Pressure Dependence of Weak Acid Ionization in Aqueous Buffers, *J. Phys. Chem.*, *77*(22), 2687–2691.

Poisson, A., and J. Chanu (1976), Partial molal volumes of some major ions in seawater, *Limnol. Oceanogr.*, *21*(6), 853–861.

Shitashima, K., M. Kyo, Y. Koike, and H. Henmi (2002), Development of in situ pH sensor using ISFET, in *International Symposium on Underwater Technology*, pp. 106–108, IEEE, Tokyo.

Wootton, J. T., C. a Pfister, and J. D. Forester (2008), Dynamic patterns and ecological impacts of declining ocean pH in a high-resolution multi-year dataset., *Proc. Natl. Acad. Sci. U. S. A.*, *105*(48), 18848–53, doi:10.1073/pnas.0810079105.

CHAPTER 5: UNIQUE HABITAT-SPECIFIC OCEAN ACIDIFICATION PROJECTIONS FROM HIGH-FREQUENCY PH OBSERVATIONS

Abstract

Assessing the impacts of anthropogenic ocean acidification requires knowledge of present-day and future environmental conditions. Here, we present a simple model for upwelling margins that projects anthropogenic acidification trajectories by combining high-temporal resolution sensor data, hydrographic surveys for source water characterization, empirical relationships of the CO_2 system, and the atmospheric CO_2 record. This model characterizes CO_2 variability on timescales ranging from hours (e.g. tidal) to months (e.g. seasonal), bridging a critical knowledge gap in ocean acidification research. A density-watermass age relationship was derived for the study region, and was combined with the 2013 Intergovernmental Panel on Climate Change CO_2 emission scenarios to add density-dependent anthropogenic carbon to the sensor time series. The model was applied to four autonomous pH sensor time series' from the surf zone, kelp forest, submarine canyon edge, and rocky bottom in the upper 100m of the Southern California Bight. All habitats were within 5 km of one another, and exhibited unique, habitat-specific CO_2 variability signatures and acidification trajectories, demonstrating the importance of making projections in the context of habitat-specific CO_2 signatures. In general, both the mean and range of pCO_2 increase in the future, with the greatest increases in both magnitude and range occurring in the deeper habitats due to reduced buffering capacity. On the other hand, Ω_{Ar}, the saturation state of Aragonite decreased in both magnitude and range. This

model can be applied to the entire California Current System, and upwelling margins in general, where sensor data are available.

Introduction

It has become increasingly apparent that the California Current System (CCS) is particularly vulnerable to anthropogenic ocean acidification due to its unique physical and chemical traits [*Feely et al.*, 2008; *Gruber et al.*, 2012; *Hauri et al.*, 2013a, 2013b]. First, since upwelled waters are naturally elevated in CO_2, anthropogenic carbon may have an increased potential to push carbonate conditions past critical biological thresholds. The equilibrium saturation level with respect to aragonite or calcite ($\Omega_{Ar\ or\ Ca} = 1$) is an example of a commonly used threshold for calcifying organisms. The saturation horizon has shoaled by approximately 50 m since pre-industrial times, and undersaturated waters ($\Omega < 1$) have been observed at the surface during strong upwelling events [*Feely et al.*, 2008]. Second, the rate of acidification (i.e. Δ pH yr^{-1}) is expected to be significantly higher along upwelling margins than that observed in the surface open ocean [*Gruber et al.*, 2012; *Bates et al.*, 2014], due to the reduced buffering capacity of seawater at higher levels of CO_2 [*Frankignoulle*, 1994]. This effect has caused parts of the CCS to venture beyond the envelope (mean ± 1 s.d.) of pre-industrial Ω_{Ar} conditions [*Hauri et al.*, 2013a]. This is significant because organisms must now survive outside of environmental conditions they are adapted to. The evolutionary potential for key ecological species to adapt to such rapid and unprecedented changes is poorly understood.

The CCS is an eastern boundary upwelling system, and supports a rich ecosystem that is of great ecological and economic value. In particular, there is great habitat and species diversity, which includes a large number of commercially important invertebrates and fishes. Habitats in the region include bays and estuaries, rocky and sandy intertidal, eel grass beds and kelp forests, sub-tidal reefs, canyons and extensive sandy sea floor. There are many endangered and harvested benthic organisms that inhabit only one or a subset of these habitats. For instance, the urchins *Strongylocentrotus purpuratus* and *S. francsicanus* are associated with rocky habitat in the intertidal and subtidal, while embryos of the market squid *Doryeteuthis opalescens* are laid along sandy bottom and canyon-edge features.

The high productivity of the CCS is fueled by the upwelling of cold, nutrient-rich waters to the surface. These upwelled waters have spent several decades in the ocean interior, isolated from the atmosphere [*Feely et al.*, 2008], during which they accumulate CO_2 and nutrients from remineralization of sinking organic particles. Generally, upwelling is strongest during the spring and summer seasons (upwelling season), but episodic upwelling/relaxation events occur throughout the year [*Send and Nam*, 2012] and near-bottom thermocline shoaling occur even at higher (e.g., diurnal and semidiurnal) frequencies during the upwelling season [*Pineda*, 1995; *Woodson et al.*, 2007; *Noble et al.*, 2009; *Nam and Send*, 2011], particularly in the southern region of the CCS.

A critical component in making accurate impact assessments of ocean acidification is the development of robust, habitat-specific projections of future CO_2

conditions [*McNeil and Matear*, 2008; *Feely et al.*, 2009, 2010; *Cai et al.*, 2011; *Sunda and Cai*, 2012; *Andersson et al.*, 2013]. Development of surface open acidification projections for the surface open ocean has been relatively straightforward, as they rely on well-defined chemical principals of CO_2 equilibrium at the air-sea interface [*Byrne et al.*, 2010]. The projections become more convoluted when outstanding biological and physical processes contribute significantly to the natural variability of the system. For example, biologically mediated "enhanced acidification" was identified in the northern Gulf of Mexico, causing significantly faster rates of acidification than the open ocean [*Cai et al.*, 2011]. In upwelling margins, both biological and physical processes contribute to the observed natural variability of carbonate conditions [*Fassbender et al.*, 2011], and must be properly parameterized.

One approach to develop region-specific ocean acidification projections is to apply an eddy-resolving regional ocean model system (ROMS) coupled with a biogeochemical component – as has been developed for the CCS [*Gruber et al.*, 2012]. Such models have highlighted the importance of capturing physical and biological processes in highly dynamic upwelling systems. The model simulations show complex spatiotemporal variability in the CCS [*Hauri et al.*, 2013a], and predict that the frequency of corrosive upwelling events will intensify in both magnitude and duration [*Hauri et al.*, 2013b]. Furthermore, the pH envelope of the upper 100 m for most regions of the CCS is already significantly lower than preindustrial levels, and is expected to depart from present-day conditions within the next several decades [*Hauri et al.*, 2013a]. However, the eddy-resolving ROMS project pCO2 and Ω on a 5-km

grid-scale, whereas many marine organisms experience the environment on the scale of centimeters to meters. This discrepancy in space incorporates processes that can confound the straightforward interpolation from global and regional ocean models to the microclimate of organisms. To improve the validity of stepping from the global and regional to the microclimate requires a quantitative assessment of the features that couple these two scales in a given environment.

To transition from region-specific to habitat-specific ocean acidification projections, high temporal resolution data from autonomous chemical sensors can be used to directly quantify the full range of present-day carbonate conditions [*Hofmann et al.*, 2011, 2014; *Harris et al.*, 2013; *Martz et al.*, 2014; *Sutton et al.*, 2014]. Sensor data provide key observations for the mechanistic understanding of the controls on environmental conditions, and are particularly needed for coastal marine environments where complex physical and biological processes influence the observed variability. For example, sensor data from a near-shore kelp forest in the southern CCS revealed that local biologic feedbacks and episodic upwelling events were the dominant drivers of CO_2 variability, with pCO_2 fluctuating by 600 µatm at 17 m water depth [*Frieder et al.*, 2012]. This scale of variability associated with near-shore environments is not captured by regional model systems, but is most relevant for organisms living in the kelp forest.

Here, we present an anthropogenic ocean acidification model to project CO_2 chemistry into the future by combining autonomous chemical sensor data, regional empirical relationships for the CO_2 system [*Alin et al.*, 2012], hydrographic data, and

the atmospheric CO_2 record [*Keeling et al.*, 2005]. This model was applied to 4 habitats in the Southern California Bight within 100-m water depth, and within a 5 km × 5 km grid. Each site showed distinct CO_2 variability signatures and acidification trajectories, highlighting the importance of interpreting ocean acidification projections in the context of present and future habitat-specific CO_2 signatures. Implications for future ocean acidification research are discussed.

Methods

Study Sites

Moored autonomous sensor packages (SeapHOx or SeaFET; see section 0) were deployed at four depths (4, 17, 30, and 88 m) at several distinct habitats on the San Diego continental shelf for 1 year starting June 2012 (Figure 5.1). All sensors were deployed near the seafloor; the three shallowest sensors were deployed within 3 m of the bottom, and the deepest sensor was moored 12 m above the seafloor (Table 5.1).

A SeaFET was deployed at the Scripps pier 2 m above the benthos as a part of the Scripps Water Acidity Monitoring Program. The sensor was located approximately 400 m from the shore in the surf zone. Weekly discrete samples for total alkalinity (TA) and dissolved inorganic carbon (DIC) were taken alongside the sensors for calibration and quality control. The sensor was serviced every couple of months to combat biofouling.

The La Jolla kelp forest is part of the South La Jolla state marine reserve and is characterized by a dense population of *Macrocystis pyrifera*. The chemical variability

in this ecosystem is strongly influenced by regional physical processes (*e.g.*, upwelling and stratification) and local biological feedbacks (*e.g.*, production and respiration). A SeapHOx was deployed at 17 m in the kelp, 3 meters above the bottom. The reader is referred to *Frieder et al.,* 2012 for further details on site and deployment description.

The La Jolla canyon is a submarine canyon plunging from approximately 20 m to a depth of 1000 m within several km from shore. A SeapHOx was deployed at the southern canyon edge at 30 m depth. Regional physical processes (e.g. upwelling, internal waves/tides, and bores) are expected to be the dominant source of the observed variability at this site [*Navarro et al.*, 2013].

The Del Mar Buoy was first deployed in 2006 at 100 m off of Del Mar in northern San Diego over a rocky bottom (http://mooring.ucsd.edu), and has provided continuous time series data (e.g. temperature, salinity, oxygen, and current) at discrete depths [*Frieder et al.*, 2012; *Send and Nam*, 2012]. The mooring was typically serviced annually. A SeaFET sensor was on the mooring at 88 m in 2011, and has provided a near-continuous time series of pH since. Co-located sensors include temperature, salinity (SBE 37), and O_2 (Aanderaa Optode).

Cruise data

Hydrographic data were collected during the student-led San Diego Coastal Expedition cruises in July and December of 2012 (Figure 5.1). These cruises correspond with the upwelling and non-upwelling seasons, respectively. Discrete samples were analyzed for dissolved oxygen (O_2), pH, and DIC. Samples collected at the same depth by independent Niskin bottles were treated as duplicate samples to

assess precision of measurements, duplicates were collected during every cast. Hydrographic data are available at BCO-DMO project SeapHOx.

Discrete samples for O_2 were collected and analyzed following standard procedures [*Dickson*, 1996] The endpoint was determined photometrically [*Bryan et al.*, 1976] using a custom titration cell [*Martz et al.*, 2012]. The titrant concentration was quantified prior to and after each cruise using KIO_3 standard solutions prepared in house (Fisher, lot 105595); no detectable drift was observed for either cruise. Precision based on duplicates was ± 0.6 µmol/kg (n = 62), and the accuracy was estimated to be ± 0.5% because KIO_3 standards were not recrystallized [*Emerson*, 1999].

Samples for DIC and pH were collected in 150 or 250 ml pyrex serum bottles (13 mm neck) following standard procedures [*Dickson et al.*, 2007]. However, rather than leaving headspace, the bottle was filled completely, and a gray butyl stopper was inserted to prevent gas exchange. Samples were typically analyzed within 4 hours of collection.

DIC samples were analyzed using an infrared analyzer (LI-COR 7000) based on systems described in *O'Sullivan and Millero*, 1998 and *Friederich et al.*, 2002. The DIC measurements were calibrated using Certified Reference Materials provided by the Dickson Lab at SIO, by applying a gain correction (slope), and assuming an offset of zero (intercept). The reference material were stored in CO_2 impermeable bags (3L Scholle DuraShield®), and were measured frequently throughout the cruise. The stability of the reference material in the bag was verified by daily measurements of a

new bottle; no drift was observed. Precision and accuracy of the measurements were ± 2.5 µmol/kg (n = 67, 1σ). Samples for pH were analyzed spectrophotometrically [*Clayton and Byrne*, 1993] using an automated system [*Carter et al.*, 2013] and are reported on the total hydrogen ion concentration scale (at in situ temperature and pressure). The indicator dye (m-cresol purple, ACROS Lot A0264321) was used as received from the manufacturer without further purification. An offset was applied based on measurements in certified Tris buffer provided by the Dickson Lab. The precision and accuracy of the measurements were estimated to be ± 0.0015 (n = 86) and ± 0.02 [*Liu et al.*, 2011], respectively. TA and pCO_2 were calculated using CO2SYS [*van Heuven et al.*, 2011] using pH and DIC as inputs, and carbonic acid dissociation constants from *Mehrbach et al.*, 1973 refit by *Lueker*, 2000.

Phosphate concentrations were estimated (PO_4^{est}) for the hydrographic data by establishing a regional empirical relationship from historical data using the approach described in *Juranek et al.*, 2009 and *Alin et al.*, 2012. The data from the North American Carbon Program 2007 West Coast Cruise data at all depths were used to calculate the coefficients for the equation:

$$PO_4^{est} = \alpha_0 + \alpha_1\left(O_2 - O_{2,r}\right) + \alpha_2(T - T_r) + \alpha_3\left(O_2 - O_{2,r}\right) \times (T - T_r) \quad (5.1)$$

where the subscript r refers to a mean reference value ($O_{2,r}$ = 156.7 µmol kg^{-1} and T_r = 9.045 °C). The PO_4^{est} were in excellent agreement with measured values (Figure 5.2), with a root mean squared error (RMSE) of 0.15 µmol/kg. This error in PO_4^{est} propagates to a ~4µmol kg^{-1} uncertainty in preformed TA (see section 0). The

coefficients of the regression were $\alpha_0 = 1.758$, $\alpha_1 = -6.52 \times 10^{-3}$, $\alpha_2 = -0.102$, and $\alpha_3 = -1.88 \times 10^{-4}$.

Sensor Data

The SeapHOx and SeaFET sensor packages utilize a modified Honeywell Durafet III pH combination electrode for high frequency pH measurements [*Martz et al.*, 2010]. These sensor packages have been successfully deployed in ecosystems worldwide [*Hofmann et al.*, 2011; *Kroeker et al.*, 2011; *Frieder et al.*, 2012; *Price et al.*, 2012; *Martz et al.*, 2014], and have been shown to have excellent stability in seawater for months to years [*Bresnahan et al.*, 2014]. The SeapHOx is an integrated sensor package that also consists of an Aanderaa 3835 oxygen optode, and a Seabird SBE 37 Conductivity-Temperature sensor, all plumbed into a pumped flow stream; the SeaFET only measures pH using a passively flushed cell. Sampling frequencies were 1 hr^{-1} or greater at all depths.

All pH measurements were calibrated based on discrete TA and DIC samples taken alongside the sensor ($n > 4$ for every depth) [*Bresnahan et al.*, 2014]. The resolution of the pH measurements is better than 0.0005 pH, stability is estimated to be better than 0.005, and accuracy is estimated to be ± 0.02. Sensors were removed periodically for maintenance, but all were deployed for > 50 days during both the upwelling and relaxation season.

At the surf zone, a constant TA value of 2240 µmol/kg was assumed, since discrete TA samples showed low variability (2240 ± 7 (1 s.d.) µmol/kg, $n = 57$). For the three subsurface sensors, TA was estimated (TA^{est}) using a regional empirical

relationship [*Alin et al.*, 2012]. An offset of +8 µmol/kg was applied to TA^{est} based on discrete samples to account for a regional surface TA influence that is not incorporated in the empirical relationship developed for the whole CCS (RMSE = 6 µmol/kg, n = 25). pH sensor data were converted to DIC and pCO_2 using CO2SYS [*van Heuven et al.*, 2011].

Modelling Future Carbonate Chemistry

The carbonate conditions were modeled between 2012 – 2100 by increasing DIC while using TA conditions from 2012. It was assumed that the increase in DIC is due to anthropogenic CO_2 invasion through the air-sea interface, and the biological and physical processes that alter DIC and TA in the ocean interior remain constant over the modeled period. We also assumed that both the path of a particular water mass between the subduction and upwelling site and the rate of remineralization processes remain unchanged. Sensitivity to these assumptions is explored in the Discussion.

The DIC of the modeled year t (DIC_t) is calculated by

$$DIC_t = DIC_{2012} + \Delta DIC_{ant} \quad (5.2)$$

where DIC_{2012} is the DIC observed in 2012 derived from sensor data, and ΔDIC_{ant} is the additional anthropogenic CO_2 that the water mass would have absorbed since 2012. Different formulations for ΔDIC_{ant} were used for surface waters (i.e., above the seasonal mixed layer depth, defined here as $\sigma_\theta \leq 25.2$ kg m^{-3}) and subsurface waters ($\sigma_\theta > 25.2$ kg m^{-3}), and are outlined below.

For surface waters, ΔDIC_{ant} is the difference in surface DIC between year t and 2012, where surface DIC is calculated by assuming atmospheric equilibrium under 2012 TA conditions, and using $pCO_{2,atm}$ projection under the 2013 IPCC RCP6 scenario [*Hijioka et al.*, 2008]. Although large deviations from equilibrium conditions are often observed in the coastal ocean due to upwelling and biological production [*Hales et al.*, 2005], the mean pCO_2 at the surf zone was 394 µatm, suggesting that the surface water at the study site was near atmospheric equilibrium over an annual cycle.

For subsurface waters, ΔDIC_{ant} is quantified as the increase in DIC due to anthropogenic CO_2 when the waters were last in contact with the atmosphere. The mass balance of DIC for subsurface waters is:

$$DIC = DIC_{eq} + \Delta DIC_{diseq} + \Delta DIC_{bio} \quad (5.3)$$

where DIC_{eq} is the DIC if it were in equilibrium with the atmosphere when it was last at the surface, ΔDIC_{diseq} is the offset from the equilibrium value caused by slow gas exchange kinetics and biological production, and ΔDIC_{bio} is the DIC added by remineralization processes in the ocean interior. The preformed DIC (DIC°), or the DIC of the water when it subducted, is the sum of the first two terms in equation (5.3):

$$DIC° = DIC_{eq} + \Delta DIC_{diseq} \quad (5.4)$$

Since anthropogenic CO_2 only enters the ocean at the surface, the increase in DIC_{eq} represents the anthropogenic ocean acidification signal. Therefore, ΔDIC_{ant} for subsurface waters can be expressed as the difference in DIC_{eq} between the modeled year t and 2012:

$$\Delta \mathrm{DIC}_{\mathrm{ant}} = \mathrm{DIC}_{\mathrm{eq}}^{\mathrm{t-age}} - \mathrm{DIC}_{\mathrm{eq}}^{2012-\mathrm{age}} \quad (5.5)$$

where the superscripts represent the year the water was last in contact with the atmosphere; age is the number of years since the water parcel was at the surface. This approach assumes that ΔDIC_{diseq} remains constant during the modeled period. $DIC_{eq}^{2012-age}$ is calculated from cruise data by removing ΔDIC_{bio} (equation (5.6)), and DIC_{eq}^{t-age} is calculated from TA° and atmospheric pCO_2 projections during the year the water mass was last in contact with the atmosphere (t - age). As an alternative to using independent tracers such as ^{14}C or CFCs to quantify water mass age, we developed a simplified tracer by matching the preformed pCO_2 from the hydrographic data to the mean annual atmospheric CO_2 record [*Keeling et al.,* 2005]. A σ_θ - modeled age relationship was established, and used for the projections between 2012 and 2100. This relationship was used to establish a density dependent ΔDIC_{ant} that was applied to sensor data. The following steps were used to calculate ΔDIC_{ant} for subsurface waters.

Step 1. Calculate $DIC_{eq}^{2012-age}$, TA°, and $fCO_{2,eq}^{2012-age}$ from cruise data.

The $DIC_{eq}^{2012-age}$ was calculated from hydrographic bottle data using equation (5.3). ΔDIC_{bio} was quantified following formulations in [*Sabine et al.,* 2002]:

$$\Delta DIC_{bio} = r_{O:C}(AOU) - 0.5(TA_{obs} - TA^{\circ} + r_{O:N}(AOU)) \quad (5.6)$$

where AOU = Apparent Oxygen Utilization = ($O_{2,sat} - O_{2,obs}$), TA° is the preformed alkalinity, and the r's are the elemental remineralization ratios [*Anderson and Sarmiento,* 1994]. The oxygen saturation concentration ($O_{2,sat}$) was calculated using

the equations in *Garcia and Gordon*, 1992, and TA° was estimated based on historical near-surface TA data in the Pacific (equation 3 in [*Sabine et al.*, 2002]); TA° for surface waters was set to 2240 µmol kg^{-1}. The ΔDIC_{diseq} was estimated as -6 µmol kg^{-1} based on θ and salinity [*Sabine et al.*, 2002]. The $fCO_{2,eq}^{2012-age}$, or the fugacity of CO_2 of the sample when it was in equilibrium with the atmosphere at the time of subduction, was calculated using $DIC_{eq}^{2012-age}$ and TA° (Figure 5.3).

Step 2: Determine age of water as a function of σ_θ.

The atmospheric CO_2 concentration when the sample was last at the surface was determined from $fCO_{2,eq}^{2012-age}$, assuming 100% relative humidity and barometric pressure of 1 atm [Dickson, 2007]. The year that the water parcel subducted was determined by matching the calculated $CO_{2,atm}$ to the mean annual $CO_{2,atm}$ record [Keeling]; the age is the difference between 2012 and this calculated year (Figure 5.3). A relationship between σ_θ and the age was established by fitting a second order polynomial to the subsurface data (n = 186, R^2 = 0.92), and assuming the age of the surface water (σ_θ < 25.2) is 0 (Figure 5.3). The age of the water ranged between 0 - 50 years between σ_θ 25.2-26.5 kg m^{-3}.

Step 3. Determine DIC_{eq}^{t-age} and calculate ΔDIC_{ant}.

The DIC_{eq}^{t-age} was calculated from TA° and the projected $CO_{2,atm}$ from the IPCC RCP6 scenario [*Hijioka et al.*, 2008] when the water mass was last at the surface. For example, atmospheric CO_2 projections for the year 2020 would be used to calculate DIC_{eq}^{t-age} for a 30-year-old water mass when t = 2050. ΔDIC_{anth} was

calculated using equation (5.5). $CO_{2,atm}$ was converted to fCO_2 for surface seawater using the same assumptions as above. The ΔDIC_{ant} for subsurface waters was modeled for each projection year as a linear function of σ_θ. The surface and subsurface ΔDIC_{ant} were connected assuming a two end member linear mixing between σ_θ 25.2 – 25.5 kg m^{-3} to prevent step changes (Figure 5.4). Preindustrial pCO_2 and Ω_{Ar} were calculated using the same model, and assuming that subsurface waters equilibrated with $pCO_{2,atm}$ of 280 µatm when it was last at the surface.

Results

Carbonate Chemistry Variability Observed in 2012

The results are presented using pCO_2 [µatm] or Ω_{Ar}, since pCO_2 and Ω_{Ar} are commonly used stress indicators for respiration [*Brewer and Peltzer*, 2009] and calcification [*Langdon et al.*, 2010]. Generally, pCO_2 increased with depth; the mean pCO_2 in the surf zone was near atmospheric equilibrium (394 µatm), while the mean pCO_2 at 88 m was 839 µatm, and reaching a maximum of 1100 µatm (Table 5.2). The range of pCO_2 also increased with depth (indicated by the s.d. of the time series), which was only 43 µatm in the surf zone, but was 120 µatm at 88 m depth. The mean Ω_{Ar} decreased with depth; the mean Ω_{Ar} in the surf zone was 2.4, where it was 1.09 at 88m. Undersaturated conditions ($\Omega_{Ar} < 1$) were observed roughly 20% of the time at 88 m. However, unlike pCO_2, the range of Ω_{Ar} decreased with depth; the s.d. of the time series in the surf zone and rocky bottom was 0.25 and 0.16, respectively (Table 5.2).

Distinct, habitat-specific CO_2 signatures were observed at the four deployment sites (Figure 5.5). A clear seasonal pattern was apparent at the canyon edge (30 m) and the rocky bottom (88 m), where higher pCO_2 was observed during the spring and summer months (upwelling season) and lower pCO_2 was observed during the fall and winter (relaxation season). The pCO_2 differs by roughly 300 – 400 µatm between the upwelling and relaxation seasons at 88 m, compared to 200 – 300 µatm at 30 m. In addition to seasonal changes, variability on higher frequencies such as tidal or event (days to weeks) time scales were observed (lower panels in Figure 5.5). Upwelling on event time scales have been documented in this study region [*Frieder et al.*, 2012; *Send and Nam*, 2012], and was observed at all three subsurface habitats (kelp forest, canyon edge, and rocky bottom). During event-scale upwelling, greater changes in pCO_2 were observed at the kelp forest and canyon edge compared to the rocky bottom (lower panels in Figure 5.5), which is opposite than what was observed on seasonal time scales. Finally, the canyon edge experienced significantly greater variability on higher frequencies (e.g. tidal) than the other sites, where fluctuations of pCO_2 of greater than 300 µatm were observed over the course of a day.

Similar trends were observed for Ω_{Ar} between the habitats, with the exception of the magnitude of the seasonal changes in Ω_{Ar} (Figure 5.6). Greater seasonal changes for Ω_{Ar} occurred at 30 m (~ 1) compared to 88 m (~0.5), which was opposite of what was observed for pCO_2. Event scale upwelling affected Ω_{Ar} at the subsurface sites, and large variability at high frequencies were observed at the canyon edge. It is important to note that all sites were within 5 km of one another, demonstrating the wide variety

of habitat-specific CO_2 signatures that exist over a small spatial scale, especially in near shore environments.

Modeled Carbonate Chemistry Variability

Changes in the modelled carbonate parameters were consistent with increasing levels of anthropogenic DIC, i.e. higher pCO_2 and lower Ω (Table 5.2). However, each habitat showed distinct trends in both modelled mean and range of pCO_2 and Ω_{Ar}. For example, the mean pCO_2 at 88 m and 30 m increased by factors of two to three greater than that observed at the surf zone, respectively. The increase in range was also larger at 88 m compared to the surface, although the largest increase occurred at the canyon edge at 30 m. The largest decrease in the mean Ω_{Ar} occurred at the surface relative to the deeper sites, whereas the decrease in range was equivalent across all depths.

The time series for pCO_2 and Ω_{Ar} at 88 m for the year 2012 and 2100 is shown in Figure Figure 5.7and Figure 5.8, respectively. The variability of pCO_2 increases by approximately two fold; the seasonal change increases to 600 – 700 µatm, and variability on higher frequencies (e.g. tidal) can be as great as 300 – 400 µatm. This greater variability is in addition to an increase in mean pCO_2 of > 700 µatm. On the other hand, the variability of Ω_{Ar} on both seasonal and shorter time scales decreases. However, the habitat experiences undersaturated conditions almost exclusively.

Pre-industrial pCO_2 and Ω_{Ar} were calculated using the same model, and assuming that subsurface waters equilibrated with $pCO_{2,atm}$ of 280 µatm when it was last at the surface. The mean and standard deviation of carbonate parameters for the pre-industrial period are reported in Table 5.2. At most sites, the observed pCO_2 and

Ω_{Ar} in 2012 were already outside of its pre-industrial variability envelopes (defined as mean ± 1 s.d.), which is consistent with results from a previous ROMS simulation in the CCS [*Hauri et al.*, 2013a]. These results suggest that all habitats studied here have left, or are about to leave the carbonate conditions that were experienced during pre-industrial times. This is significant as organisms at these sites are now surviving in conditions that are significantly different than what they are adapted to. The pCO_2 variability envelope will leave 2012 conditions between 2055 and 2080, whereas Ω_{Ar} follows about 5 to 10 years later (Table 5.3).

The modeled habitat-specific pCO_2 and Ω_{Ar} conditions for pre-industrial, 2012, 2060, and 2100 are shown in Figure 5.9. The histograms represent the full range of carbonate conditions at each habitat that was captured by the sensors, which includes both the seasonal and high-frequency variability. The kelp forest and canyon edge will start to experience undersaturated conditions ($\Omega < 1$) about 10 % of the time by 2060. A negative trend between increased range and proportional time at a given carbonate condition is apparent. The shape of the distribution skews towards more "corrosive" conditions (i.e. higher pCO_2 and lower Ω_{Ar}) at all sites, as the model steps forward into the future. This means that not only will each habitat experience elevated levels of CO_2 in the coming decades, but they will spend disproportionately higher amounts of time in unfavorable carbonate conditions.

Discussion

Model Assessment

The sensitivity of the projected carbonate conditions to the assumptions made in the model is explored. Sea surface temperature has increased over the past century due to climate change [*Smith et al.*, 2008], and is expected to continue. This will affect the CO_2 equilibrium concentration (DIC_{eq}), but the effects are small and will only reduce DIC_{eq} by several μmol kg^{-1}, thus can be safely ignored. Both pCO_2 and Ω_{Ar} are dependent on in situ temperature; the effects on Ω_{Ar} are negligible ($\Delta\Omega/\Delta T < 0.01$ $°C^{-1}$), whereas $\Delta pCO_2/\Delta T$ increases at higher pCO_2 levels, and can be as large as 30 μatm $°C^{-1}$ at the end of the century. However, it is important to note that this effect will affect the mean conditions, but the magnitude of the variability will be relatively unaffected.

TA conditions from 2012 were used to calculate pCO_2 and Ω_{Ar} for all years. Changes in TA affect the buffering capacity of seawater, thus, alterations in TA distribution will either speed up, or slow down the progression of ocean acidification. However, trends in TA along the CCS on decadal time scales are unknown due to lack of observations. Reduced ventilation in high latitude seas, altered precipitation patterns, and changes in surface calcification and water-column dissolution rates would all lead to changes in TA conditions. Quantifying these processes is very difficult and out of the scope of this study. Nevertheless, to demonstrate the magnitude of the uncertainty due to using TA conditions from 2012, pCO_2 was projected for the year 2100 by applying a +20 μmol kg^{-1} bias to TA. The effects were strongly dependent on DIC: mean pCO_2 was reduced by approximately 240, 130, and 70 μatm at 88 m, 30 m, and the surface, respectively.

Finally, the model presented here projects future carbonate conditions by assuming the dynamics that control the variability at each habitat (e.g. seasonal and episodic upwelling events, internal waves and tides, biological production/respiration) remain the same as 2012 conditions, leading to uncertainties in our projections. Severe O_2 and pH changes associated with interannual climate events on the Southern California Bight has been observed [*Nam et al.*, 2011]. Since 2012 did not correspond with a strong El Niño or La Niña phase, we believe that it was not strongly biased by such events. However, at this time, we lack observations with sufficient longevity to predict how climate variability on interannual to decadal time scales might modify the acidification trajectory over the course of the next century. For example, recent evidence suggests that the proportion of Pacific Equatorial Waters in the California Under Current has been increasing over the past several decades, thus modifying the source water properties for upwelled waters onto the continental shelf [*Bograd et al.*, 2014]. Since waters of equatorial origin are elevated in DIC [*Nam et al.*, *In Prep*.], the Southern California Bight will experience higher levels of acidification than predicted from this study if this trend continues. Sustained, high-frequency time series of inorganic carbon parameters are required to elucidate such effects.

Observed and Modelled Carbonate Chemistry Variability

The respective changes in these carbonate parameters with depth, i.e. increase in pCO_2 and decrease in Ω_{Ar}, are due to the greater influence of upwelled waters at deeper sites. At 88 m, the water is isolated from the atmosphere, thus the variability in carbonate chemistry is driven dominantly by subsurface processes such as seasonal

and episodic upwelling events [*Nam et al.*, 2011; *Frieder et al.*, 2012; *Send and Nam*, 2012] and higher-frequency processes such as internal waves and bores [*Pineda*, 1995]. The shallower depth sites (kelp forest and canyon edge) intermittently experience waters that are near-atmospheric equilibrium conditions (Figure 5.5), thus their variability is controlled by both subsurface processes and periodic exposure to near-surface conditions. Furthermore, the kelp forest has significant biological feedback that affects carbonate chemistry variability [*Frieder et al.*, 2012], highlighting the importance of local processes to the observed variability in carbonate chemistry.

The trajectories are sensitive to the choice of the emission scenario (Figure 5.10); the trends are similar at all depths, thus only the mean pCO_2 and Ω_{Ar} projections at 88 m are shown. The highest emission scenario (RCP8) diverges the earliest around 2030, followed by the lowest emission scenario RCP2.5 around 2050. The two intermediate scenarios (RCP4 and RCP6) do not diverge significantly until 2070. The delayed response to different atmospheric CO_2 trajectories occurs because upwelled waters have spent several decades since they were last in contact with the atmosphere. Therefore the anthropogenic ocean acidification trajectory for the Southern California Bight is already determined for the next several decades, and any mitigation due to changing CO_2 emissions will be delayed.

Changes in the Buffering Capacity

The patterns observed in the modeled pCO_2 and Ω_{Ar} are driven solely by the increase in anthropogenic DIC, since TA conditions from 2012 were used. The ability

for seawater to buffer changes in pCO_2 diminishes under higher concentrations of DIC (i.e. higher Revelle factor), thus the same biological and physical forcings cause a larger change in pCO_2. The buffer factor Π_{pCO2} and Π_{CO3} are defined as

$$\Pi_{pCO2} = \frac{dpCO_2}{dDIC}, \qquad \Pi_{CO3} = \frac{dCO_3^{2-}}{dDIC} \tag{5.7}$$

and they represent the change in its respective carbonate parameter per change in DIC [*Frankignoulle*, 1994] . (Figure 5.11). The effect of temperature on Π is small (< 10%) between 0 – 15 °C for the DIC and TA values analyzed here, thus subsequent values were calculated assuming a temperature of 10 °C.

On average, Π_{pCO2} increased from 1.6 to 3.3 at the surface between 2012 and 2100 under the RCP6 scenario. However, since deeper waters are naturally elevated in DIC, this effect is more pronounced: Π_{pCO2} increases from 6.2 to 12.3 during the same time interval at 88 m. The water at 88 m is isolated from the atmosphere, thus the greater increase in both magnitude and range relative to the surface is driven mainly by the decreased buffering capacity (Figure 5.9). However, the greater increase in range was observed at shallower depths (17 and 30 m) than at 88 m. This is because these sites are influenced from both surface waters and upwelled waters, thus experiencing near-atmospheric equilibrium conditions to elevated CO_2 due to remineralization in the ocean interior (Figure 5.5).

Changes in Π_{CO3} can explain the patterns for Ω_{Ar}, since $[Ca^{2+}]$ and K_{SP} remain unchanged. Unlike $\Pi_{pCO2,}$ $|\Pi_{CO3}|$ decreases at higher concentrations of DIC (Figure 5.11); $|\Pi_{CO3}|$ decreases from -0.62 to -0.57 at the surface, and -0.49 to -0.3 at 88 m

between 2012 and 2100. This change in Π_{CO3} explains both the decrease in rate and range of Ω_{Ar} as anthropogenic CO_2 continues to infiltrate the ocean.

Conclusions

Here we have presented habitat-specific carbonate chemistry projections for four habitats within the upper 100 m of the Southern California Bight. The projections were generated by combining high frequency sensor measurements, a regional empirical relationship for TA, hydrographic survey data to quantify the source-water properties of upwelled waters, and the atmospheric CO_2 record . Even though the four habitats were within 5 km of one another, distinct habitat-specific variability signatures and acidification trajectories were observed. These results reveal the existence of highly variable CO_2 signatures within a small geographic area, and the potential for discoveries of habitats that could act as refuges from ocean acidification. In addition, when assessing impacts of ocean acidification, it is imperative to quantify the history of the organisms under study, and interpret their physiological responses in context of current and future environmental conditions. The development of habitat-specific ocean acidification models is critical in establishing realistic experimental conditions to accurately assess the biological impacts of ocean acidification.

At all habitats, increases in both mean and range of pCO_2, and decreases in mean and range of Ω_{Ar} were observed. Changes in buffering capacity largely explained these patterns, however, local biological feedbacks could also produce a large acidification signal. In all habitats studied here, carbonate conditions have left, or are leaving pre-industrial variability envelopes; under the RCP6 scenario, all habitats

are expected to move outside of 2012 conditions between 2060 and 2080. This suggests that the anthropogenic ocean acidification will continue to progress in the CCS and other upwelling margins over the next several decades regardless of any changes in CO_2 emissions; any impacts from reduced emissions will only be observed mid-century and beyond. This demonstrates the urgency of the situation, and this delayed response must be taken into account when assessing the impacts of ocean acidification, and developing mitigation and monitoring strategies.

The model presented in this study can be applied to the whole CCS, and upwelling margins in general. The Southern California Bight experiences steady but weaker degree of upwelling compared to the northern regions in the CCS, where upwelling events are more severe [*Feely et al.*, 2008]. These regions could experience more extreme conditions regularly, as well as significantly higher variability of carbonate conditions. However, high-frequency observations of carbonate parameters are relatively scarce, and such dynamics are poorly understood. Furthermore, source water properties will necessarily be different, thus must be characterized for each study region. Alternatively, for regions where such data for source waters are not available, sensor data can be combined with either Global Circulation Model or ROMS outputs. This approach will alleviate the cost associated with characterizing source waters, and to a large degree, will incorporate processes (e.g. interannual variability, decadal changes in source water properties, and reduced ventilation) that are hard to quantify in the projections. It is critical that inorganic carbon sensors (e.g.

pH or pCO_2) are co-located with basic physical oceanographic measurements (e.g. T and S) to determine source water properties, especially for subsurface deployments.

Acknowledgements

We would like to thank the UC Ship Funds for providing ship time for the San Diego Coastal Expedition cruises, and all of the volunteers that aided in sample collection and analysis. We would also like to thank the Ellen Browning Scripps Foundation and California State Water Board for supporting the Scripps Water Acidity Monitoring Program.

Chapter 5, in full, is currently being prepared for submission for publication of the material. Takeshita, Y., Frieder, C.A., Martz, T.R., Ballard, J.R., Feely, R.A., Nam, S., and Navarro, M. The dissertation author was the primary investigator and author of this paper.

Table 5.1: Summary of sensor deployments

Habitat Type	Deployment site	DD[a]	BD[b]	Sensor	Days[c]
Surf Zone	Scripps Pier	4	6	SeaFET	122
Kelp Forest	La Jolla Kelp Forest	17	20	SeapHOx	128
Canyon Edge	La Jolla Canyon	30	30	SeapHOx[d]	302
Rocky Bottom	Del Mar Buoy	88	100	SeaFET	335

[a] Sensor deployment depth in meters
[b] Bottom Depth in meters
[c] Total deployment days between June 2012 and June 2013.
[d] A linear drift correction for salinity was applied for 2 of the 4 deployments.

Table 5.2. Mean ± s.d. of modelled carbonate parameters at in situ conditions for preindustrial, 2012, 2060, and 2100 using the RCP6 projection at each habitat.

	Year	pCO_2 (µatm)	Ω_{Ar}	pH
Surf Zone (4 m)	Pre-ind.	267 ± 26	3.09 ± 0.21	8.19 ± 0.034
	2012	394 ± 43	2.38 ± 0.25	8.05 ± 0.038
	2060	473 ± 56	2.09 ± 0.19	7.98 ± 0.041
	2100	619 ± 80	1.71 ± 0.18	7.88 ± 0.045
Kelp Forest (17 m)	Pre-ind.	389 ± 64	2.16 ± 0.33	8.05 ± 0.064
	2012	555 ± 93	1.66 ± 0.28	7.92 ± 0.067
	2060	739 ± 136	1.32 ± 0.25	7.81 ± 0.076
	2100	1020 ± 202	1.01 ± 0.22	7.68 ± 0.084
Canyon Edge (30 m)	Pre-ind.	365 ± 68	2.29 ± 0.37	8.08 ± 0.068
	2012	529 ± 105	1.75 ± 0.31	7.94 ± 0.075
	2060	702 ± 155	1.40 ± 0.29	7.83 ± 0.085
	2100	964 ± 231	1.09 ± 0.25	7.70 ± 0.095
Rocky Bottom (88 m)	Pre-ind.	602 ± 106	1.44 ± 0.24	7.88 ± 0.070
	2012	839 ± 120	1.09 ± 0.16	7.75 ± 0.060
	2060	1143 ± 163	0.84 ± 0.13	7.62 ± 0.060
	2100	1577 ± 204	0.62 ± 0.09	7.49 ± 0.056

Table 5.3: Estimated year when projected carbonate parameters leave 2012 envelopes under the RCP6 scenario.

	pCO_2	Ω_{Ar}
Surf Zone	2056	2058
Kelp Forest	2070	2081
Canyon Edge	2078	2085
Rocky Bottom	2058	2067

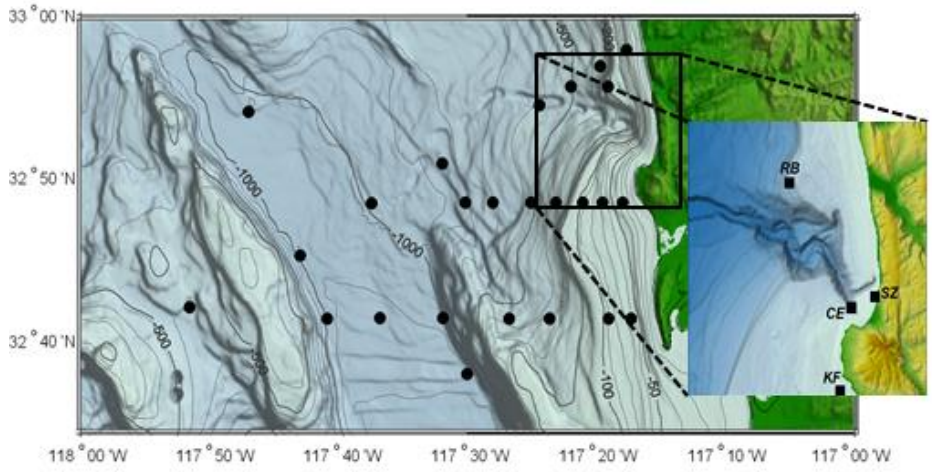

Figure 5.1: Map of study region. Hydrographic stations (black dots) and sensor deployment sites (black squares) are shown. Initials are: CE = canyon edge, RB = rocky bottom, SZ = surf zone, and KF = kelp forest.

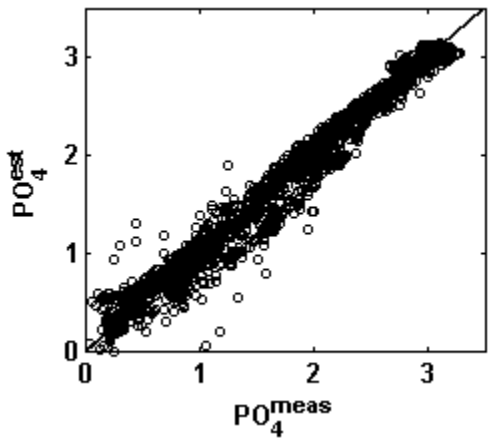

Figure 5.2: Measured phosphate (PO_4^{meas}) versus estimated phosphate (PO_4^{est}) (R^2 = 0.98). Solid line represents a 1:1 relationship

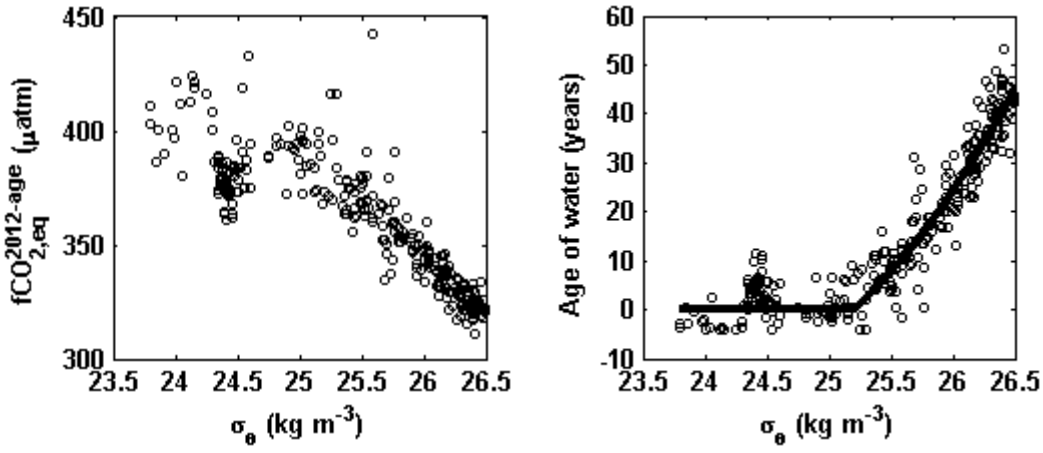

Figure 5.3: $fCO_{2,eq}^{2012-age}$ calculated from hydrographic data (left) and the calculated age – σ_θ relationship (right) is shown. Good agreement (R^2 = 0.87) between the data (black open circles) and the fit (black line) is observed (right). Age of surface waters (σ_θ < 25.2 kg m^{-3}) was assumed to be 0.

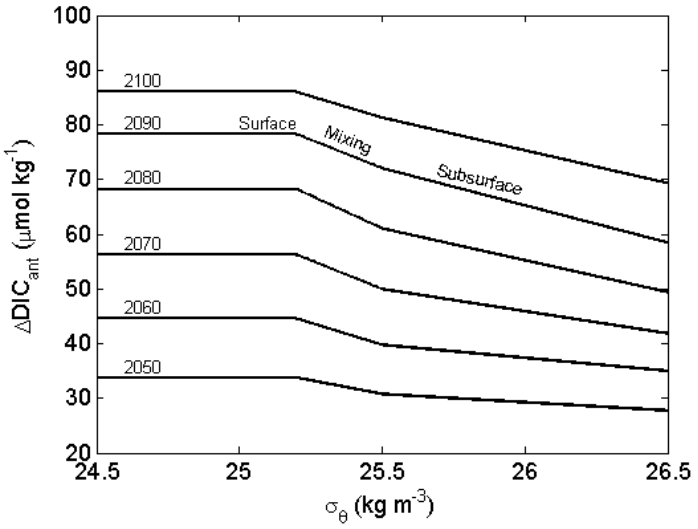

Figure 5.4: ΔDIC_{anth} as a function of σ_θ for certain modeled years (indicated above line). The three regimes used in this model, surface, mixing, and subsurface are labeled.

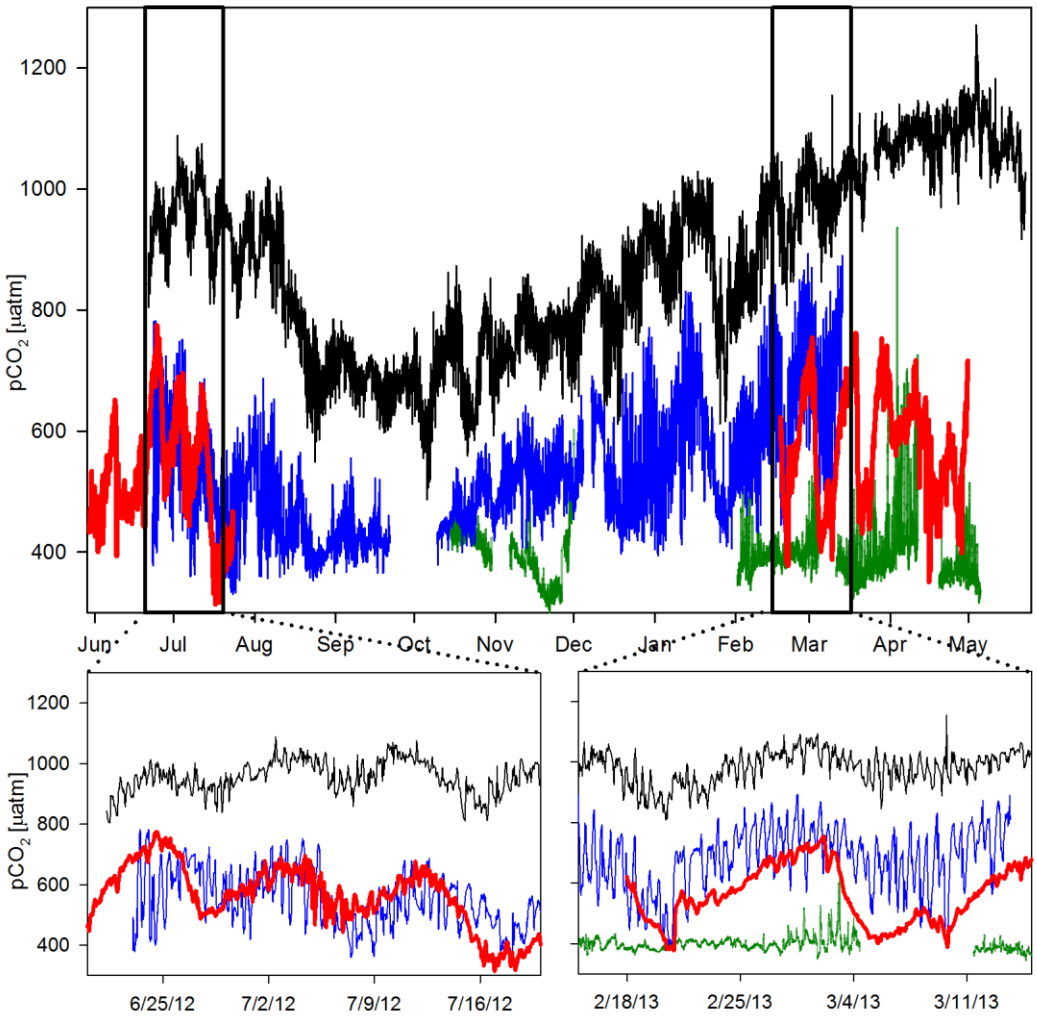

Figure 5.5: Time series sensor pCO_2 data between June 2012 to June 2013 (top) from the Scripps Pier (green), La Jolla Kelp Forest (red), La Jolla canyon edge (blue), and the Del Mar Buoy (black). The bottom figures present two 30-day snippets of the year-long time series. pCO_2 is reported at in situ conditions.

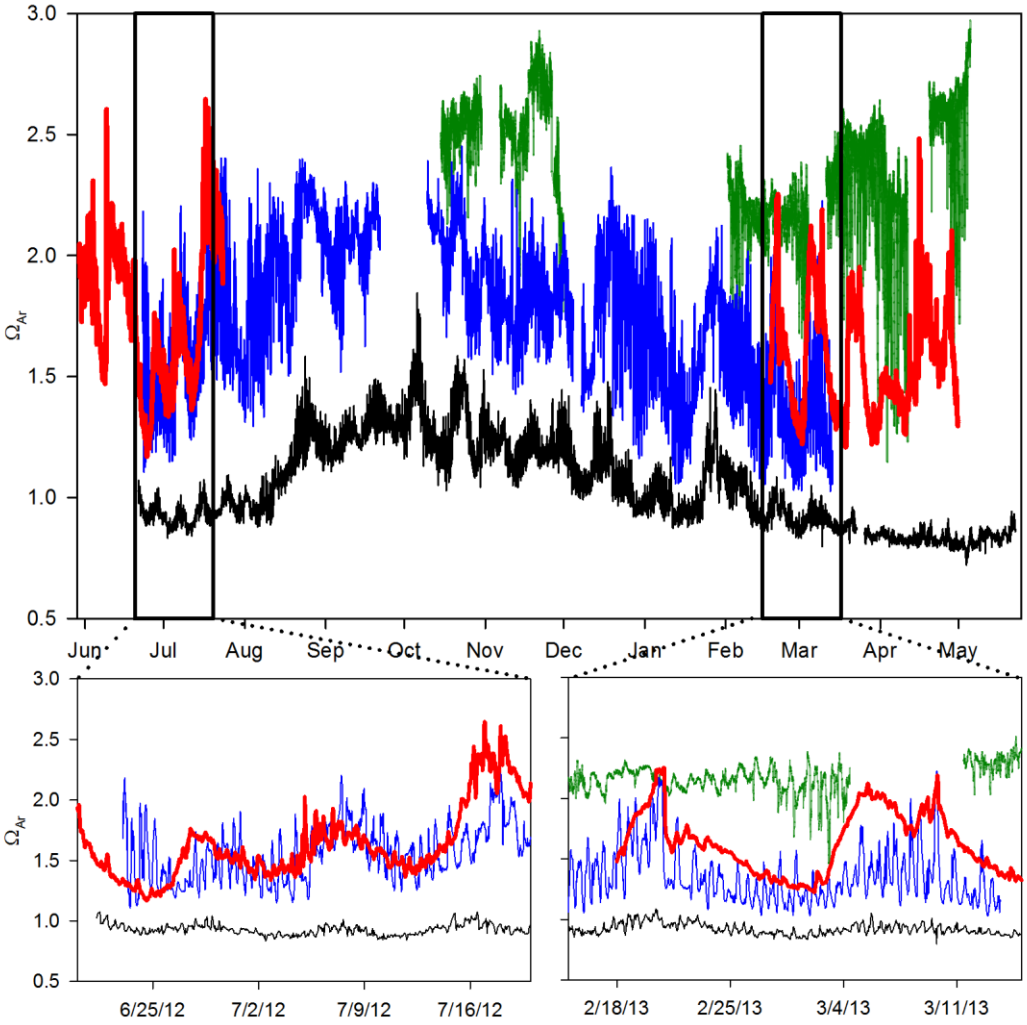

Figure 5.6: Same as Figure 5.5 but for Ω_{Ar}.

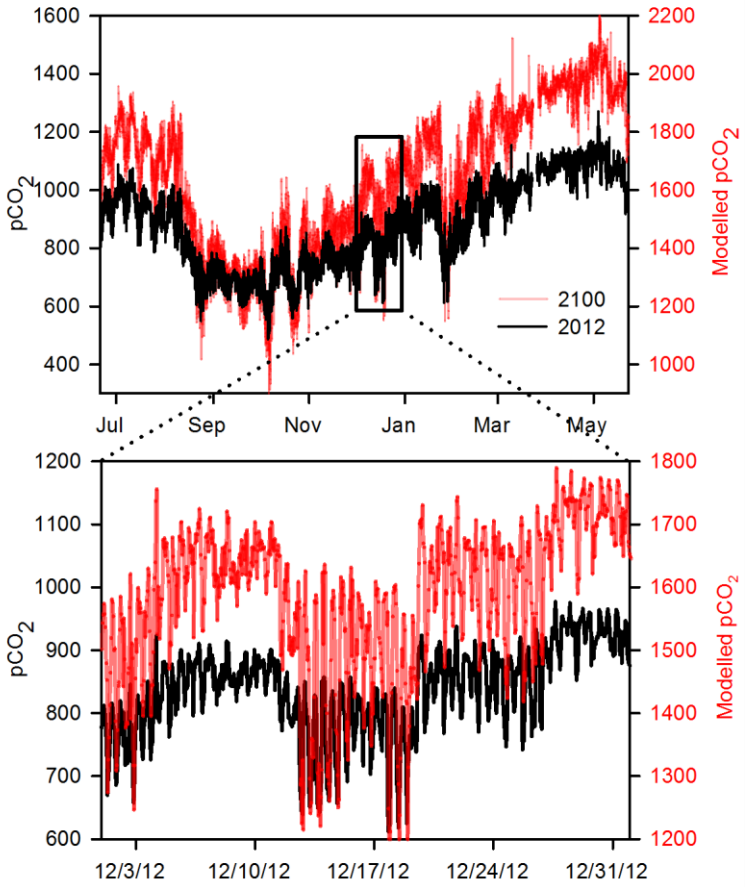

Figure 5.7: Observed pCO_2 in 2012 (black) and modelled pCO_2 using the ICPP RCP 6 scenario for the year 2100 (red) at the Del Mar Buoy (88 m) over an annual cycle (top). A close up for the month of December is shown on the bottom. Note that the range of the vertical axes for each figure is the same.

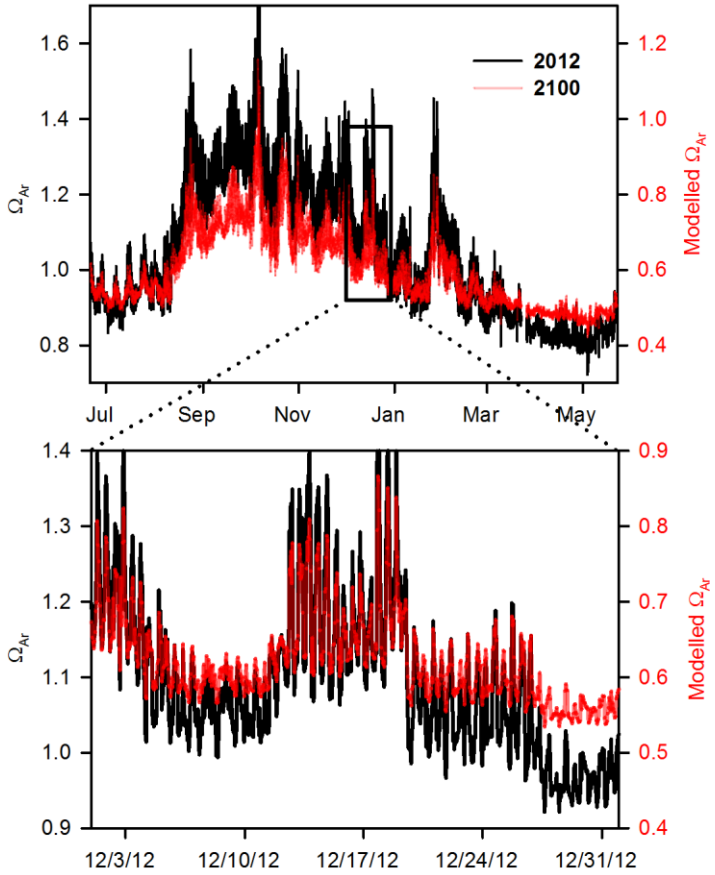

Figure 5.8: Same as Figure 5.7 but for Ω_{Ar}.

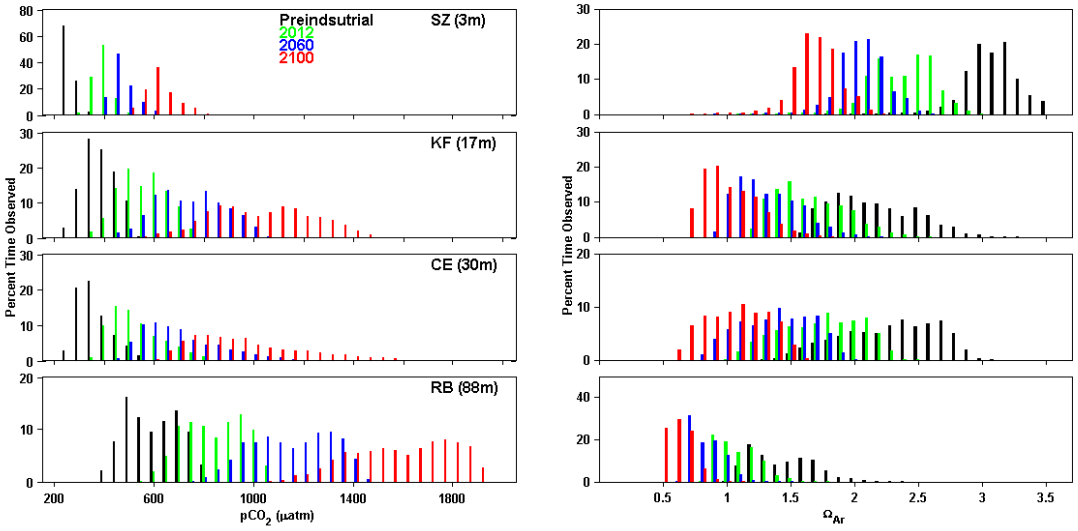

Figure 5.9: Histogram of modeled pCO_2 (left) and Ω_{Ar} (right) distribution at the four depths for preindustrial (black), 2012 (green), 2060 (blue), and 2100 (red). Atmospheric pCO_2 for the years 2060 and 2100 roughly correspond to 510 and 670 µatm based on the IPCC RCP6 scenario. Initials are: CE = canyon edge, RB = rocky bottom, SZ = surf zone, and KF = kelp forest.

+

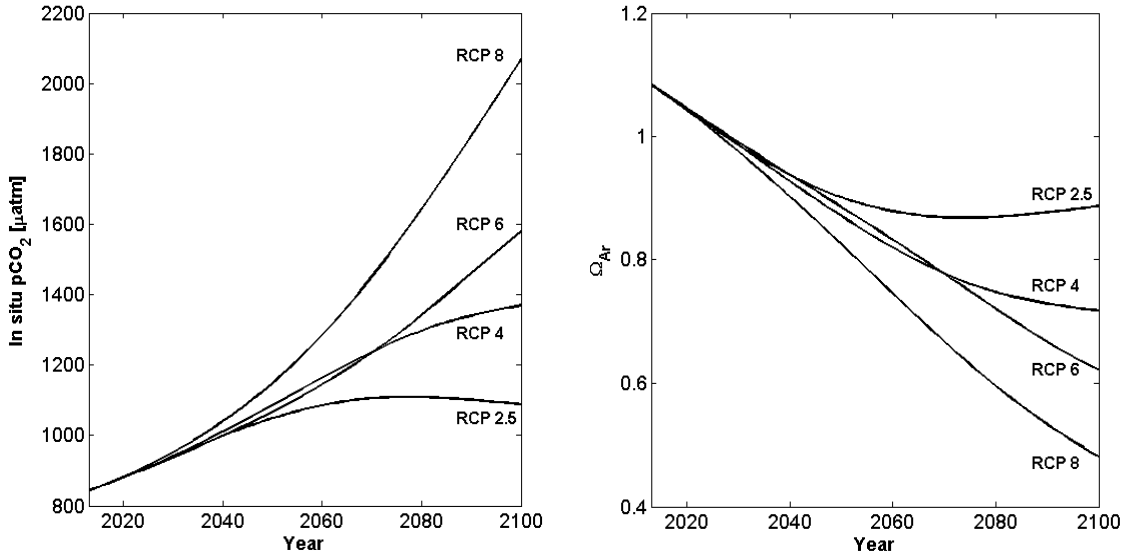

Figure 5.10: Projections of mean pCO_2 (left) and Ω_{Ar} (right) at the RB site (88m) based on four IPCC projections.

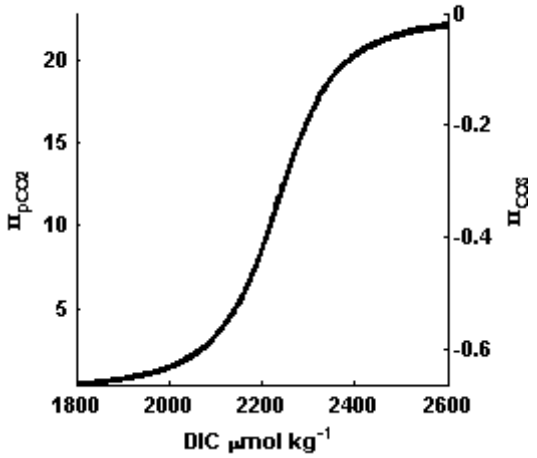

Figure 5.11: Π_{pCO2} and Π_{CO3} versus DIC. Π's were calculated assuming TA = 2240 µmol kg^{-1}, temperature = 10 °C, and salinity = 33.5.

References

Alin, S. R., R. a. Feely, A. G. Dickson, J. M. Hernández-Ayón, L. W. Juranek, M. D. Ohman, and R. Goericke (2012), Robust empirical relationships for estimating the carbonate system in the southern California Current System and application to CalCOFI hydrographic cruise data (2005–2011), *J. Geophys. Res.*, *117*(C5), doi:10.1029/2011JC007511.

Anderson, L. A., and J. L. Sarmiento (1994), Redfield Ratios of Remineralization Determined by Nutrient Data Analysis, *Global Biogeochem. Cycles*, *8*(1), 65–80.

Andersson, A. J., K. L. Yeakel, N. R. Bates, and S. J. de Putron (2013), Partial offsets in ocean acidification from changing coral reef biogeochemistry, *Nat. Clim. Chang.*, *3*(11), 1–6, doi:10.1038/nclimate2050.

Bates, N. R., Y. M. Astor, M. J. Church, K. Currie, J. E. Dore, M. Gonzalez-Davila, L. Lorenzoni, F. Muller-karger, J. Olafsson, and J. M. Santana-Casiano (2014), A Time-Series View of Changing Surface Ocean Chemistry Due to Ocean Uptake of Anthropogenic CO2 and Ocean Acidification, *Oceanography*, *1*, 126–141.

Bograd, S. J., M. P. Buil, E. Di Lorenzo, C. G. Castro, I. D. Schroeder, R. Goericke, C. R. Anderson, C. Benitez-Nelson, and F. a. Whitney (2014), Changes in source waters to the Southern California Bight, *Deep Sea Res. Part II Top. Stud. Oceanogr.*, 1–11, doi:10.1016/j.dsr2.2014.04.009.

Bresnahan, P. J., T. R. Martz, Y. Takeshita, K. S. Johnson, and M. LaShomb (2014), Best practices for autonomous measurement of seawater pH with the Honeywell Durafet, *Methods Oceanogr.*, *Accepted*.

Brewer, P. G., and E. T. Peltzer (2009), Limits to Marine Life, *Science (80-.).*, *324*, 347–348.

Bryan, J. R., J. P. Riley, and P. J. L. Williams (1976), A Winkler Procedure for Making Precise Measurements of Oxygen Concentration for Productivity and Related Studies, *J. Exp. Mar. Bio. Ecol.*, *21*, 191–197.

Byrne, R. H., S. Mecking, R. A. Feely, and X. Liu (2010), Direct observations of basin-wide acidification of the North Pacific Ocean, *Geophys. Res. Lett.*, *37*(2), 1–5, doi:10.1029/2009GL040999.

Cai, W.-J. et al. (2011), Acidification of subsurface coastal waters enhanced by eutrophication, *Nat. Geosci.*, *4*(11), 766–770, doi:10.1038/ngeo1297.

Carter, B. R., J. a. Radich, H. L. Doyle, and a. G. Dickson (2013), An automated system for spectrophotometric seawater pH measurements, *Limnol. Oceanogr. Methods*, *11*, 16–27, doi:10.4319/lom.2013.11.16.

Clayton, T. D., and R. H. Byrne (1993), Spectrophotometric seawater pH measurements : total hydrogen results, *Deep Sea Res. Part I Oceanogr. Res. Pap.*, *40*(10), 2115–2129.

Dickson, A. G. (1996), Determination of dissolved oxygen in sea water by Winkler titration, *Stand. Oper. Proced.*, 1–13.

Dickson, A. G., C. L. Sabine, and J. R. Christian (Eds.) (2007), *Guide to best practices for ocean CO2 measurements*, PICES Special Publication 3.

Emerson, S. (1999), Accurate measurement of O2, N2, and Ar gases in water and the solubility of N2, *Mar. Chem.*, *64*(4), 337–347, doi:10.1016/S0304-4203(98)00090-5.

Fassbender, A. J., C. L. Sabine, R. a. Feely, C. Langdon, and C. W. Mordy (2011), Inorganic carbon dynamics during northern California coastal upwelling, *Cont. Shelf Res.*, *31*(11), 1180–1192, doi:10.1016/j.csr.2011.04.006.

Feely, R. A., C. L. Sabine, J. M. Hernandez-Ayon, D. Ianson, and B. Hales (2008), Evidence for upwelling of corrosive "acidified" water onto the continental shelf., *Science*, *320*(5882), 1490–2, doi:10.1126/science.1155676.

Feely, R. A., S. C. Doney, and S. R. Cooley (2009), Ocean Acidification Present Conditions and Future Changes in a High-CO2 World, *Oceanography*, *22*(4), 36–47.

Feely, R. a., S. R. Alin, J. Newton, C. L. Sabine, M. Warner, A. Devol, C. Krembs, and C. Maloy (2010), The combined effects of ocean acidification, mixing, and respiration on pH and carbonate saturation in an urbanized estuary, *Estuar. Coast. Shelf Sci.*, *88*(4), 442–449, doi:10.1016/j.ecss.2010.05.004.

Frankignoulle, M. (1994), A complete set of buffer factors for acid / base CO2 system in seawater, *J. Mar. Syst.*, *5*(2), 111–118.

Frieder, C. A., S. Nam, T. R. Martz, and L. A. Levin (2012), High temporal and spatial variability of dissolved oxygen and pH in a nearshore California kelp forest, *Biogeosciences*, *9*(10), 3917–3930, doi:10.5194/bg-9-3917-2012.

Friederich, G. E., P. M. Walz, M. G. Burczynski, and F. P. Chavez (2002), Inorganic carbon in the central California upwelling system during the 1997 – 1999 El Niño–La Niña event, *Prog. Oceanogr.*, *54*(1-4), 185–203.

Garcia, H. E., and L. I. Gordon (1992), Oxygen Solubility in Seawater : Better Fitting Equations, *Limnol. Oceanogr.*, *37*(6), 1307–1312.

Gruber, N., C. Hauri, Z. Lachkar, D. Loher, T. L. Frölicher, and G.-K. Plattner (2012), Rapid progression of ocean acidification in the California Current System., *Science (80-.).*, *337*(6091), 220–3, doi:10.1126/science.1216773.

Hales, B., T. Takahashi, and L. Bandstra (2005), Atmospheric CO 2 uptake by a coastal upwelling system, *Global Biogeochem. Cycles*, *19*(1), n/a–n/a, doi:10.1029/2004GB002295.

Harris, K. E., M. D. DeGrandpre, and B. Hales (2013), Aragonite saturation state dynamics in a coastal upwelling zone, *Geophys. Res. Lett.*, *40*(11), 2720–2725, doi:10.1002/grl.50460.

Hauri, C., N. Gruber, M. Vogt, S. C. Doney, R. A. Feely, Z. Lachkar, A. Leinweber, A. M. P. McDonnel, M. Munnich, and G.-K. Plattner (2013a), Spatiotemporal variability and long-term trends of ocean acidification in the California Current System, *Biogeosciences*, *10*, 193–216.

Hauri, C., N. Gruber, a. M. P. McDonnell, and M. Vogt (2013b), The intensity, duration, and severity of low aragonite saturation state events on the California continental shelf, *Geophys. Res. Lett.*, *40*(13), 3424–3428, doi:10.1002/grl.50618.

Van Heuven, S., D. Pierrot, J. W. B. Rae, E. Lewis, and D. W. . Wallace (2011), MATLAB Program Developed for CO2 System Calculations. ORNL/CDIAC-105b., , doi:10.3334/CDIAC/otg.CO2SYS_MATLAB_v1.1.

Hijioka, Y., Y. Matsuoka, H. Nishimoto, M. Masui, and M. Kainuma (2008), Global GHG emissions scenarios under GHG concentration stabilization targets, *J. Glob. Environ. Eng.*, *13*, 97–108.

Hofmann, G. E. et al. (2011), High-Frequency Dynamics of Ocean pH: A Multi-Ecosystem Comparison, edited by W.-C. Chin, *PLoS One*, *6*(12), e28983, doi:10.1371/journal.pone.0028983.

Hofmann, G. E. et al. (2014), Exploring local adaptation and the ocean acidification seascape – studies in the California Current Large Marine Ecosystem, *Biogeosciences*, *11*(4), 1053–1064, doi:10.5194/bg-11-1053-2014.

Juranek, L. W., R. a. Feely, W. T. Peterson, S. R. Alin, B. Hales, K. Lee, C. L. Sabine, and J. Peterson (2009), A novel method for determination of aragonite saturation state on the continental shelf of central Oregon using multi-parameter relationships with hydrographic data, *Geophys. Res. Lett.*, *36*(24), L24601, doi:10.1029/2009GL040778.

Keeling, C. D., S. C. Piper, R. B. Bacastow, M. Wahlen, T. P. Whorf, M. Heimann, and H. A. Meijer (2005), Atmospheric CO2 and 13CO2 exchange with the terrestrial biosphere and oceans from 1978 to 2000: observations and carbon cycle implications, in *A History of Atmospheric CO2 and its effects on Plants, Animals, and Ecosystems*, edited by J. R. Ehleringer, T. E. Cerling, and M. D. Dearing, pp. 83–113, Springer Verlag, New York.

Kroeker, K. J., F. Micheli, M. C. Gambi, and T. R. Martz (2011), Divergent ecosystem responses within a benthic marine community to ocean acidification., *Proc. Natl. Acad. Sci. U. S. A.*, *108*(35), 14515–20, doi:10.1073/pnas.1107789108.

Langdon, C., J. Gattuso, and A. Andersson (2010), Measurements of Calcification and Dissolution of Benthic Organisms and Communities, in *Guide to Best Practices for Ocean Acidificaton Research and Data Reporting*, pp. 213–232, Publications Office of the European Union, Luxembourg.

Liu, X., M. C. Patsavas, and R. H. Byrne (2011), Purification and characterization of meta-cresol purple for spectrophotometric seawater pH measurements., *Environ. Sci. Technol.*, *45*(11), 4862–8, doi:10.1021/es200665d.

Lueker, T. J., A. G. Dickson, and C. D. Keeling (2000), Ocean pCO2 calculated from dissolved inorganic carbon, alkalinity, and equations for K1 and K2: validation based on laboratory measurements of CO2 in gas and seawater at equilibrium, *Mar. Chem.*, *70*, 105–119, doi:10.1016/S0304-4203(00)00022-0.

Martz, T., Y. Takeshita, R. Rolph, and P. Bresnahan (2012), Tracer monitored titrations: measurement of dissolved oxygen., *Anal. Chem.*, *84*(1), 290–296, doi:10.1021/ac202537f.

Martz, T., U. Send, M. D. Ohman, Y. Takeshita, P. Bresnahan, H.-J. Kim, and S. Nam (2014), Dynamic Variability of Biogeochemical Ratios in the Southern California Current System, *Geophys. Res. Lett.*, *41*(7), 2496–2501, doi:10.1002/2014GL059332.

Martz, T. R., J. G. Connery, and K. S. Johnson (2010), Testing the Honeywell Durafet for seawater pH applications, *Limnol. Oceanogr. Methods*, *8*, 172–184, doi:10.4319/lom.2010.8.172.

McNeil, B. I., and R. J. Matear (2008), Southern Ocean acidification: a tipping point at 450-ppm atmospheric CO2., *Proc. Natl. Acad. Sci. U. S. A.*, *105*(48), 18860–4, doi:10.1073/pnas.0806318105.

Mehrbach, C., C. H. Culberson, J. E. Hawley, and R. M. Pytkowicz (1973), Measurement of the apparent dissociation constants of carbonic acid in seawater at atmospheric pressure, *Limnol. Oceanogr.*, *18*(6), 897–907, doi:10.4319/lo.1973.18.6.0897.

Nam, S., and U. Send (2011), Direct evidence of deep water intrusions onto the continental shelf via surging internal tides, *J. Geophys. Res.*, *116*(C5), C05004, doi:10.1029/2010JC006692.

Nam, S., H.-J. Kim, and U. Send (2011), Amplification of hypoxic and acidic events by La Niña conditions on the continental shelf off California, *Geophys. Res. Lett.*, *38*(22), 1–5, doi:10.1029/2011GL049549.

Nam, S., C. A. Frieder, Y. Takeshita, J. R. Ballard, and T. R. Martz (2014), Dissolved oxygen and inorganic carbon altered by upwelling and advection of Pacific Equatorial Water near the southern California coast, *Prep*.

Navarro, M. O., P. E. Parnell, and L. A. Levin (2013), Year-round spawning of te Market Squid, Doryteuthis opalescens and associated critical habitat along an upwelling margin, in *Coastal and Estuarine Research Federation National Conference*, San Diego.

Noble, M., B. Jones, P. Hamilton, J. Xu, G. Robertson, L. Rosenfeld, and J. Largier (2009), Cross-shelf transport into nearshore waters due to shoaling internal tides in San Pedro Bay, CA, *Cont. Shelf Res.*, *29*(15), 1768–1785, doi:10.1016/j.csr.2009.04.008.

O'Sullivan, D. W., and F. J. Millero (1998), Continual measurement of the total inorganic carbon in surface seawater, *Mar. Chem.*, *60*(1-2), 75–83, doi:10.1016/S0304-4203(97)00079-0.

Pineda, J. (1995), An internal tidal bore regime at nearsbore stations along western U.S.A.: Predictable upwelling within the lunar cycle, *Cont. Shelf Res.*, *15*(8), 1023–1041.

Price, N. N., T. R. Martz, R. E. Brainard, and J. E. Smith (2012), Diel Variability in Seawater pH Relates to Calcification and Benthic Community Structure on Coral Reefs., *PLoS One*, *7*(8), e43843, doi:10.1371/journal.pone.0043843.

Sabine, C. L., R. a. Feely, R. M. Key, J. L. Bullister, F. J. Millero, K. Lee, T.-H. Peng, B. Tilbrook, T. Ono, and C. S. Wong (2002), Distribution of anthropogenic CO2 in the Pacific Ocean, *Global Biogeochem. Cycles*, *16*(4), 30–1–30–17, doi:10.1029/2001GB001639.

Send, U., and S. Nam (2012), Relaxation from upwelling: The effect on dissolved oxygen on the continental shelf, *J. Geophys. Res.*, *117*(C4), 1–9, doi:10.1029/2011JC007517.

Smith, T. M., R. W. Reynolds, T. C. Peterson, and J. Lawrimore (2008), Improvements to NOAA's Historical Merged Land–Ocean Surface Temperature Analysis (1880–2006), *J. Clim.*, *21*(10), 2283–2296, doi:10.1175/2007JCLI2100.1.

Sunda, W. G., and W.-J. Cai (2012), Eutrophication induced CO2-acidification of subsurface coastal waters: interactive effects of temperature, salinity, and atmospheric PCO2., *Environ. Sci. Technol.*, *46*(19), 10651–9, doi:10.1021/es300626f.

Sutton, A. J., R. A. Feely, C. L. Sabine, M. J. McPhaden, T. Takahashi, F. P. Chavez, G. E. Friederich, and J. T. Mathis (2014), Natural variability and anthropogenic change in equatorial Pacific surface ocean pCO2 and pH, *Global Biogeochem. Cycles*, *28*, 1–15, doi:10.1002/2013GB004679.

Woodson, C. B. et al. (2007), Local diurnal upwelling driven by sea breezes in northern Monterey Bay, *Cont. Shelf Res.*, *27*(18), 2289–2302, doi:10.1016/j.csr.2007.05.014.

CHAPTER 6: CONCLUSION

Observing biogeochemical dynamics at the spatial and temporal resolution of the ARGO profiling float array would truly revolutionize our understanding of the ocean. Currently there are only a handful of chemical sensors that are routinely deployed on profiling floats, e.g. dissolved oxygen [*Körtzinger et al.*, 2005; *Tengberg et al.*, 2006], nitrate [*Johnson and Coletti*, 2002; *Sakamoto et al.*, 2009; *Johnson et al.*, 2013], and bio-optical sensors [*Boss et al.*, 2008]. However, even the most commonly utilized sensor (O_2) only accounts for less than 7% of the current float array. Although a significant obstacle to increasing the number of chemical sensors on profiling floats is cost related, the lack of calibration protocols is also inhibiting the progress of the integration of chemical sensors into the float array. Establishment of such protocols would promote the wide-spread use of chemical sensor data from floats, and gain support from the oceanographic community.

After initial reports demonstraTed the long term stability of oxygen sensors on profiling floats [*Körtzinger et al.*, 2005; *Tengberg et al.*, 2006], multiple research groups deployed oxygen profiling floats around the world. However, the importance of properly calibrating sensors was not yet fully appreciated, and the quality of the factory calibration was not verified prior to deployment, leading to large uncertainties in the resultant dataset. Some research groups started "calibrating" profiling float oxygen data by collecting discrete samples alongside the float at the time of deployment; only a handful of floats were corrected using this approach, and the vast majority of oxygen profiling floats remained, essentially, uncalibrated. In chapter 2, I

quality controlled the global profiling float oxygen dataset by comparison to a monthly climatology. The results from this chapter demonstrated that a post-deployment correction is not a viable alternative to proper calibration of the sensors, and highlighted the critical necessity to establish and implement strict calibration protocols prior to deployment.

A large portion of my dissertation was aimed at establishing and improving the calibration for the Deep Sea Durafet: the first pH sensor to be integrated onto profiling floats. First, the behavior of ISFET and Cl-ISE (the two electrodes that constitute the Deep Sea Durafet) over a wide range of pH and salinity was thoroughly characterized (chapter 3). This work revealed that non-ideal behavior of the electrodes lead to negligible errors in calculated pH for the open ocean; an enabling step for the use of the Deep Sea Durafet to monitor pH using profiling floats. Second, a calibration protocol for the Deep Sea Durafet over a wide range of temperature and pressure was presented (chapter 4). The calibrated Deep Sea Durafets were then used to characterize the pressure dependence of Tris buffer, the accepted pH standard for seawater. The results from this chapter allow for the calibration of Deep Sea Durafets in seawater media, which would expedite the calibration process, and potentially lead to a more robust calibration. Establishing calibration protocols for chemical sensors may take years to accomplish, and the calibration process may cost as much, if not, more than the sensor itself; a fact that is often underappreciated and overlooked. However, in almost all cases, the price of not calibrating a sensor is higher than properly calibrating the sensor.

Initial field results from the Deep Sea Durafet are promising. Excellent agreement between sensor and discrete sample pH was observed (Figure 6.1), where the mean ± s.d. of the residual (pH_{sensor} - $pH_{discrete}$) below 100 m over two research cruises was 0.001 ± 0.009 (n = 206). The Deep Sea Durafet was calibrated months prior to the comparison and was not adjusted, demonstrating the robustness, and the long-term stability of the calibration coefficients. In September 2012, the first profiling float equipped with the Deep Sea Durafet was deployed near the Hawaii Ocean Time-series station ALOHA. Again, excellent agreement between float and historical pH was observed. Since then, a total of 10 pH profiling floats have been deployed worldwide, including 7 in the southern ocean (data available at http://www.mbari.org/chemsensor/floatviz.htm). Within several months of deployment, the 7 profiling floats have already made more pH observations in the southern ocean during the austral winter than have been made historically, demonstrating the power of this technology. As the number of chemical sensors on profiling floats continues to increase for the coming years to decades, unprecedented data will become available for studying biogeochemical processes in the ocean.

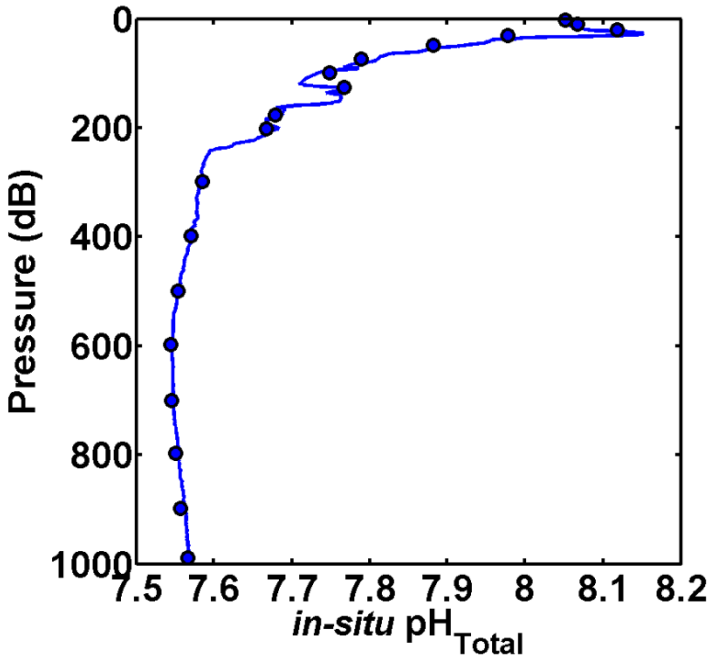

Figure 6.1: Depth profile of in situ pH from a Deep Sea Durafet (solid line) and discrete samples analyzed using spectrophotometry (closed circle). Discrete pH was corrected to *in situ* temperature and pressure.

References

Boss, E. S., D. Swift, L. Taylor, P. Brickley, S. C. Riser, M. J. Perry, and P. G. Strutton (2008), Observations of pigment and particle distributions in the western North Atlantic from an autonomous float and ocean color satellite, *Limnol. Oceanogr.*, *53*(5-2), 2112–2122.

Johnson, K. S., and L. J. Coletti (2002), In situ ultraviolet spectrophotometry for high resolution and long-term monitoring of nitrate, bromide and bisulfide in the ocean, *Deep Sea Res. Part I Oceanogr. Res. Pap.*, *49*(7), 1291–1305, doi:10.1016/S0967-0637(02)00020-1.

Johnson, K. S., L. J. Coletti, H. W. Jannasch, C. M. Sakamoto, D. D. Swift, and S. C. Riser (2013), Long-term Nitrate Measurements in the Ocean Using the In Situ Ultraviolet Spectrophotometer: Sensor Integration into the Apex Profiling Float, *J. Atmos. Ocean. Technol.*, *30*, 1854–1866, doi:10.1175/JTECH-D-12-00221.1.

Körtzinger, A., J. Schimanski, and U. Send (2005), High quality oxygen measurements from profiling floats: A promising new technique, *J. Atmos. Ocean. Technol.*, *22*(3), 302–308.

Sakamoto, C. M., K. S. Johnson, and L. J. Coletti (2009), Improved algorithm for the computation of nitrate concentrations in seawater using an in situ ultraviolet spectrophotometer, *Limnol. Oceanogr. Methods*, *7*, 132–143.

Tengberg, A. et al. (2006), Evaluation of a lifetime-based optode to measure oxygen in aquatic systems, *Limnol. Oceanogr.*, *4*, 7–17.